The University of Nottingham

Power Electronics, Machine and Control Group
Department of Electrical and Electronic Engineering
Faculty of Engineering

Distributed Speed Control for Multi-Three-Phase Motors with Enhanced Power Sharing Capabilities

Alessandro Galassini

Submitted to the University of Nottingham
for the degree of Doctor of Philosophy

January, 2018

For Alessandra
and for my scattered family

Abstract

This thesis describes the last three years work and the results achieved after several stages of design and experimental validation. The main result is the development of a novel sharing current controller for multi-three-phase electrical machines. The proposed regulator, called "*speed-drooped*" or simply "*droop*" controller, allows the current transient triggered by a step change within the rotating reference frame to be controlled. Since multi-three-phase systems appear to be very good candidates for future Integrated Modular Motor Drives and next transportation system challenges, the work has been set up with modularity and redundancy for next future motor drives.

During the preliminary stages, the mathematical models of the *droop* controller have been derived and validated on a multi-drive rig with two three-phase induction motors on the same shaft at the University of Nottingham. After, while developing a new general purpose control platform for power electronics able to control up to three three-phase systems, the Vector Space Decomposition for de-coupling the mutual interactions within multi-three-phase electric motors has been studied. Thanks to it, the inductance matrix of a triple-star two poles synchronous generator at the University of Trieste, Italy, has been diagonalised. Finally, the proposed current controller has been experimentally validated on a nine-phase synchronous generator and compared with the state of the art current sharing techniques. Furthermore, a post-fault compensation strategy has been formulated and validated by means of simulation work.

If compared to the state-of-the-art current sharing techniques, the "*droop*" regulator capability of controlling current sharing transients while keeping constant speed of the shaft has been proven and successfully demonstrated by means of Matlab/Simulink simulations and experiments on both rigs.

Acknowledgements

It all began from a phone call:
- "*Galasso, would you like to start a PhD in Nottingham?*"
- "*Why not!*"
I answered to Giampaolo.

First of all, many thanks to Giampaolo Buticchi and Davide Barater for introducing me to the University of Nottingham and to my main supervisor Professor Chris Gerada. Secondly, I would like to thank my second supervisor Dr. Alessandro Costabeber for all the support and the advice during the last three years. Thirdly, I would like to deeply thank Professors Alberto Tessarolo and Roberto Menis from the University of Trieste for giving me the possibility to collaborate with them and to share their lab spaces with Mauro Bortolozzi, Mario Mezzarobba, and Nicola Barbini.

Many thanks to all the people I have met in Power Electronics, Machines and Control (PEMC) group for all the technical discussions, the exchange of experiences and the great time spent together in the lab, and not only in the lab. My special thanks for developing with me the *uCube* control platform to Dr. Andrea Formentini and Dr. Giovanni Lo Calzo. Among all, many thanks to my companions Savvas, Marija, Manju, Emre and to all the Italian crew with Tarisciotti, Papini, Nuzzo, Tardelli, Claudio, Valerio, Marfoli, and all the others.

The last but not least thanks are for Michele Degano for introducing me to the University of Trieste and for all the rest. Finally, many thanks to the best Trimone ever: Mauro Di Nardo.

List of Terms

Abbreviations

$2L$-$3P$-VSI: 2-Level 3-Phase Voltage Source Inverter

AC: Alternating Current

AD: Actuation Delay

ADC: Analogue to Digital Converters

ARM: Advanced RISC (Reduced Instruction Set Computer) Machine

AXI: Advanced eXtensible Interface protocol

$BEMF$: Back Electro Motive Force

CL: Closed Loop

CPU: Central Processing Unit

CSR: Common Speed Reference

DAC: Digital to Analogue Converters

DC: Direct Current

DDR: Double Data Rate

DSP: Digital Signal Processor

ES: Equal Sharing

$EIA/TIA-XX$: set of communication standard

FC: Fault Condition

FE: Finite Element

FOC: Field Oriented Control

$FPGA$: Field Programmable Gate Array

GNU: recursive acronym for "GNU's Not Unix"

GUI: Graphical User Interface

IMD: Integrated Motor Drive

IMMD: Integrated Modular Motor Drive

IP: Intellectual Property cores or Internetwork Protocol

IRFO: Indirect Rotor Flux Observer

LPF: Low Pass Filter

MCU: Micro Controller Unit

NC: Nominal Condition

NUP, *NU*: Not UPdating

OC: Open Circuit condition

OCM: On Chip Memory

OL: Open Loop

OS: Operating System

PC: Personal Computer

PEBB: Power Electronics Building Block

PEMC: Power Electronics, Machine, and Control

PI_I: Proportional Integral current controller

PI_S: Proportional Integral speed controller

PL: Programmable Logic

PS: Processing System

PWM: Pulse Width Modulation

RAM: Random Access Memory

RMS: Root Mean Square

RNDIS: Remote Network Driver Interface Specification

SC: Short Circuit condition

SDRAM: Synchronous Dynamic Random Access Memory

SIM: SIMulated

SoC: System on Chip

SSM: State Space Model

TCP: Transmission Control Protocol
TF: Torque Follower
THD: Total Harmonic Distortion
UDP: User Datagram Protocol
U, UP: UPdating
US: Unbalanced Sharing
USB: Universal Serial Bus
VSD: Vector Space Decomposition
VSI: Voltage Source Inverter
WS: Wrong Sharing
$ZEDS$: Zonal Electrical Distribution System
pu or $p.u.$: per unit
$uCube$: micro-cube

Nomenclature

In general, bold upper case letters are matrices and lower case letters are vectors. Nomenclature is organised like the following: upper case latin letters, lower case latin letter, and greek letters.

Latin letters

A: state matrix
B: input matrix
C: output matrix
C: controller transfer function
D: feed-through (or feed-forward) matrix
F: friction
G: transfer function matrix

G: transfer function

G_{Dj}: j-th droop controller

G_{EQ}: equivalent droop collective controller

H: homopolar stator leakage inductance

I: identity matrix

I_{SH}: droop controller integral part (K_{iSH}/s)

I_n: nominal current

L: inductance matrix

L_{md}, L_{mq}: dq magnetising inductances

J: inertia

K_D: droop controller coefficient

K_t: machine constant

K_{iSH}: integral droop controller coefficient

K_{pI}: proportional current controller coefficient

K_{iI}: integral current controller coefficient

K_{pS}: proportional speed controller coefficient

K_{iS}: integral speed controller coefficient

M: stator leakage inductance

N: number of modules

O: null matrix

P: de-coupling transformation matrix within rotating orthonormal reference frame

P_i: output active power

P_j: power produced by the j-th module

Q: de-coupling transformation matrix within stationary orthonormal reference frame

R: resistance matrix

T: transformation matrix

T_A: torque produced by working modules

T_j: torque produced by the j-th module

T_L: load torque

T_s: actuation delay

V_n: nominal voltage

W: matrix mapping split-phase scheme into the equivalent n-phase scheme

W_j: j-th sharing coefficient

W_T: global sharing coefficient

X: stator leakage inductance

Y_h: h^{th} time harmonic amplitude

a, b, c: three-phase identifiers

$_{abc}$: per-phase time variant frame identifier

a_n: numerator real part of the plant to be controlled

a_d: denominator real part of the plant to be controlled

b_n: numerator imaginary part of the plant to be controlled

b_d: denominator imaginary part of the plant to be controlled

d_1, q_1: first $d-q$ harmonic inductances

$_{dq0}$, $_{dq}$: rotating orthonormal reference frame identifier

e: phase electromotive force

$_e$: even

f_{SW} switching frequency

h: module identifier ($h = 1..N$) or harmonic order identifier ($h = 1..2\nu \pm 1$)

j: column index or module identifier ($j = 1..N$) or imaginary part

k: phase identifier ($k = 1..n$)

i: phase current or row index or module identifier ($i = 1..N$)

m: number of phases per isolated set of winding

n: number of phases

$_o$: odd

p: pair poles or pole

q: set of harmonic order ($q = 1, 3, 5, 7..2\nu \pm 1$)

r_s: stator resistance

s: Laplacian operator

$_{std}$: n-phase winding scheme identifier

u: input signal

v: phase voltage

$_{vsd}$: orthonormal vector space decomposition frame identifier

x: state space variable

y: output signal

y_k: value of variable in phase k from n-phase winding scheme

z: zero

Greek letters

$\Delta\omega_{MAX}$: Maximum speed drop

Λ: d or q axis identifier

Υ: transfer function relating the i-th input to the j-th output

α: phase shift angle

$\alpha\beta\gamma$: stationary orthonormal reference frame identifier

ε: $\sum_j^N (1/K_{Dj})$

ϑ: rotor angular position

ν: number of time harmonics present in n phase variables from n-phase winding scheme

ξ_j: j-th power sharing scaling factor

τ: time constant

ϕ_d, ϕ_q, ϕ_0: flux along d, q, and 0 axis

ϕ_h: h^{th} time harmonic phase

φ_c: current loop phase margin

φ_{SH}: sharing loop phase margin

φ_s: speed loop phase margin

ω: rotor angular speed or electrical pole or pulsation

ω_0: base reference angular frequency

ω_D: droop controller internal set-point

ω_c: q current loop cut-off bandwidth

ω_{cd}: d current loop cut-off bandwidth

ω_f: current filter cut-off bandwidth

ω_i: output voltage angular frequency

ω_{SH}: sharing loop cut-off bandwidth

ω_s: speed loop cut-off bandwidth

Symbols

*: set-point

$^{*'}$: new set-point

$\hat{}$: measured value

Contents

List of Figures

List of Tables

Chapter 1

Introduction

The electrification of transportation systems started much before the advent of fossil fuel technologies. If the electrification process resisted to oil and petroleum superseding in some fields, in most cases fossil fuel technologies subverted the electrification process started at the end of the nineteenth century. At that time, engineers already studied how to electrify many different technologies for a wide range of applications, like for example locomotives (Fig. 1.1a) [1] and tractor ploughs (Fig. 1.1b) [2]. So far, many technology advancements have been achieved both in terms of electrical machine and controller design. However, thanks to the invention of the transistor [3] and the born of power electronics, controllers have seen a further improvements

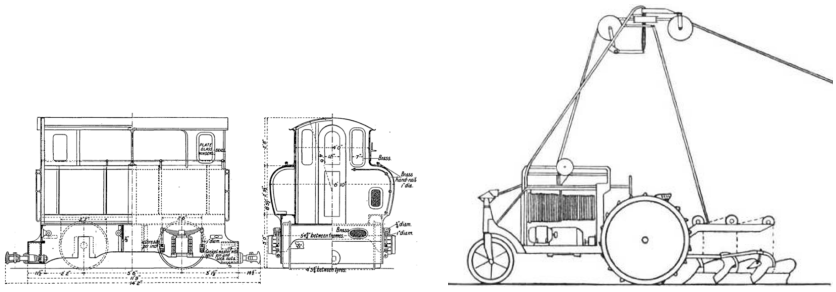

(a) Electric locomotive. (b) Electric tractor plough.

Figure 1.1: Electrified prototype vehicles from the last century [1, 2].

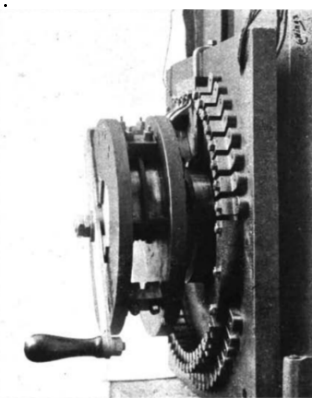

(a) Series-parallel controller.

(b) Variable frequency drive.

Figure 1.2: Controller evolution during the last century.

if compared to electrical machines. For example, in Fig. 1.2, the controller advancement during the last century is shown. In Fig. 1.2a, a series-parallel controller is shown [1] and it is compared versus a modern variable frequency drive in Fig. 1.2b [4]. The electrification of transportation systems had started at the beginning of the last century with railways [5]. After more than one hundred years, power electronics together with renewable energy sources and storage devices advancements have launched a proper propulsion system revolution. In this context, multiple research projects for transportation systems, i.e. aerospace [6, 7], mining machines [8, 9], ships [10, 11], offshore wind turbines [12], ultra high speed elevators [13], and road vehicles [14], have been founded by governments, innovation centres, and companies around the world. Furthermore, the recent availability of low cost off-the-shelf micro-processors had allowed many different integrated motor drives to be investigated and developed [15].

Considering the current Industry 4.0 revolution where the availability of bulk data allows new services never imagined before to be developed, variable frequency drives can be further improved for delivering data to the cloud of a cyber-physical system [16] like the one in Fig. 1.3 proposed by

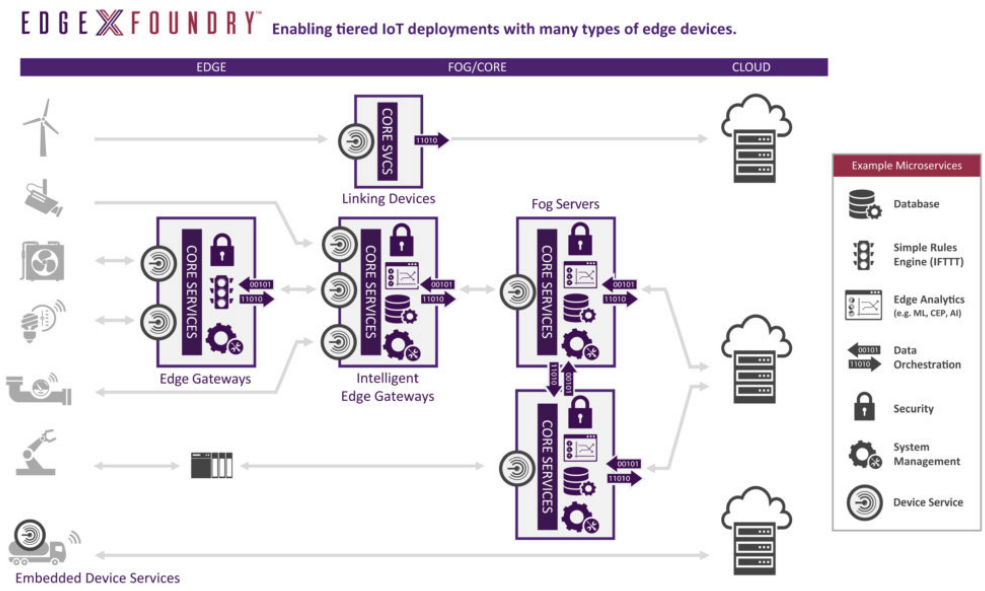

Figure 1.3: Common open platform unifying Internet of Things (IoT) proposed by Edgex.

the EdgeX Foundry, a vendor-neutral open source project hosted by the Linux Foundation building a common open framework for Industrial IoT edge computing.

Summarising, improved reliability, fuel savings, emission reduction, noise reduction and secured inter-connectivity have been recognised as one of the main key features of future electrified systems [17].

1.1 Aims and objectives

Nowadays, most three-phase motors are supplied by a conventional three phase-motor drive made of one 2-Level 3-Phase Voltage Source Inverter (2L-3P-VSI) and one controller [18]. Integrated Motor Drives (IMD) are the result of the innovation process suitable for applications requiring high efficiency and power density [19, 20, 21]. Next generation drives should provide

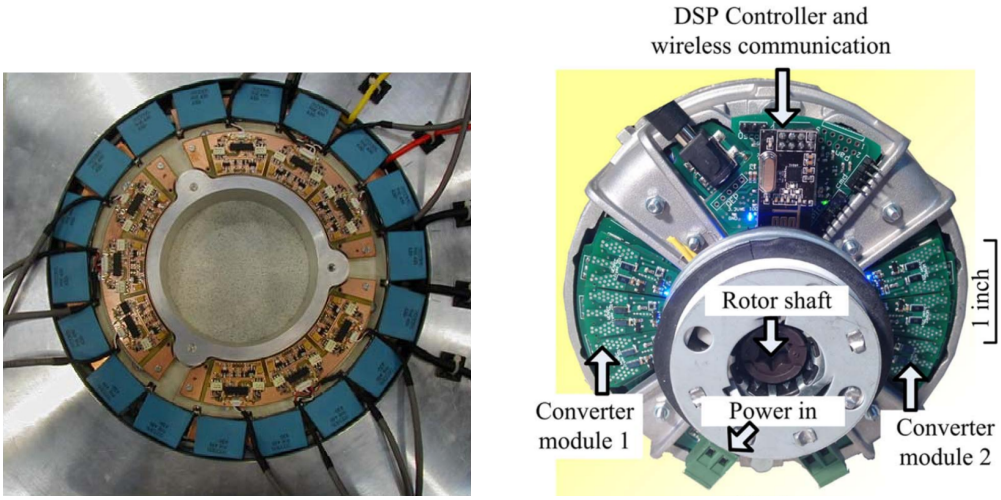

(a) Integrated matrix converter [21]. (b) Centralised DSP [20].

Figure 1.4: Integrated Motor Drives (IMD) examples.

greater reliability, robustness and competitiveness on the global market of propulsion systems. In Fig.s 1.4a-1.4b, some examples of integrated but not modular, not distributed, and not fully redundant drives are shown. The integrated converter in Fig. 1.4a is one single $30kW$ matrix converter connected to one three phase motor, therefore it is not redundant on both machine and converter side and the controller is not even integrated. The system in Fig. 1.4b is not redundant either because the two 2L-3P-VSIs are controlled by one single DSP controller.

Redesigning the drive with the Power-Electronics-Building-Block (PEBB) [22] in mind is not just a simple physical redistribution of the components into the housing to save space and wire length, but it is a chance to investigate new possible features, and therefore, new market opportunities. The need for data for new services, together with the electrification of transportation systems seeking for higher reliability and fault tolerance, leads to the concept of Integrated Modular Motor Drives (IMMD) with distributed control capabilities shown in Fig. 1.5. Modularisation introduces redundancy, increasing up time service and availability. Every module of the distributed IMMD is

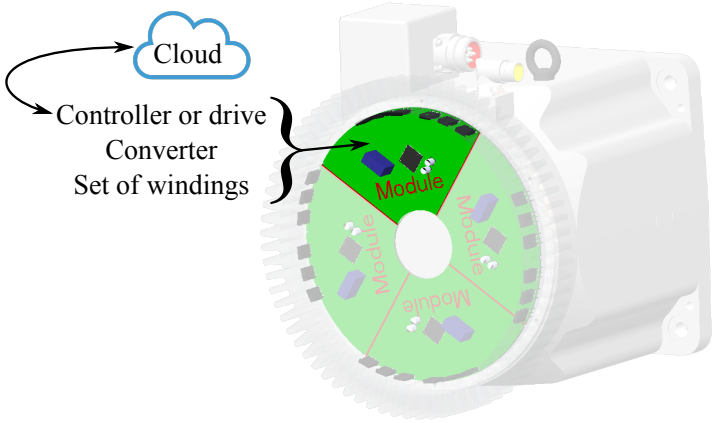

Figure 1.5: Distributed IMMD sketch composed by four modules.

meant to be made of one three-phase set of windings, one three-phase converter and one controller, thus full redundancy on machine, converter and drive side is guaranteed. Furthermore, considering nowadays technologies, every controller could be connected to a cloud like the one in Fig. 1.3. This new kind of approach leads to new functionalities, for example, every controller could detect a fault on its own module and it could notify the other controllers through the cloud or through a communication field-bus. Once notified, all the other modules could re-configure itself in order to cope with the specific fault condition restoring nominal performances.

Currently only a few prototypes of Integrated Motor Drives have been developed [20, 21, 23, 24, 25, 26]. So far, some post-fault compensation strategies for different multi-drive systems and multi-three-phase motors have been investigated [27, 28, 29, 30]. Integration adds other problems, for example, thermal management; consequently more emphasis must be taken in heat extraction [31, 32].

Due to their benefits listed in Table 1.1, IMMDs are one of the best candidates for future electrical propulsion systems [33]. That said, evaluation of the total costs has to also take into account the additional features; for example, the field-bus communication module could be integrated in the

IMMD reducing costs of the utmost system. At the moment, higher cost is the main issue preventing their diffusion. However, the flexibility and functionalities introduced by IMMD systems is expected to reduce the payback time in the near future; indeed, due to their modularity, on a large scale economy the costs of the IMMD is likely to be cut down [18]. Considering all the advantages and disadvantages summarised in Table 1.1, IMMD commercialisation to a comparable price to standard three-phase drives requires significant efforts in many different fields.

Table 1.1: Pros and cons of IMMD

Benefits	**Drawbacks**
Volume, Weight ⇓	Design complexity in general
Wires length, Costs ⇓	Thermal management
Electro Magnetic Interference ⇓	Control strategy
Redundancy and Reliability ⇑	Mechanical integration
Availability and Maintainability ⇑	Vibrations suppression

This thesis has been carried on with particular attention to the control strategy in order to increase the functionalities of the future power drive systems including improved load sharing and fault tolerance. The main objective of this work is to develop a new regulator capable of controlling the power sharing transient among paralleled DC/AC converters and to study benefits and drawbacks of different configurations and arrangements for multi-three-phase machines.

1.2 Conventional converter arrangements

In three-phase electrical motor drives all phases a, b and c are connected to the 2-Level 3-Phase Voltage Source Inverter (2L-3P-VSI), shown in Fig. 1.6, and the total amount of power is managed by its three legs. Reliability and fault tolerance can be difficult to achieve, especially if the neutral point is not reachable. Redundancy and large scale market economy can be both

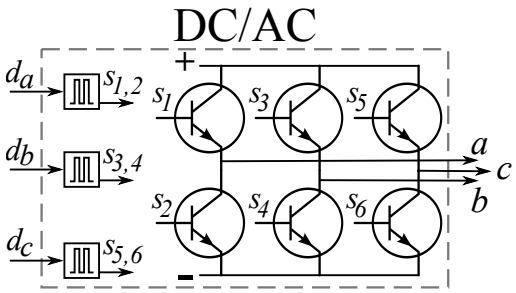

Figure 1.6: DC/AC 2-Level 3-phase Voltage Source Inverter (2L-3P-VSI). d_a,d_b, and d_c are the duty cycles. a, b, and c are the output phases.

improved at the same time modularising the three-phase machine and the relative 2L-3P-VSI. In fact, rewinding the machine in a different way gives designers some possibilities to increase fault tolerance. Among the possible choices, this section considers the specific case of a rewound three phase machine, where two main arrangements are possible: series and parallel, shown in Fig. 1.7a and Fig. 1.7b respectively [19, 20].

In both figures, the DC/AC blocks are meant to be the three phase two level inverter topology (Fig. 1.6). Each inverter is connected to the relative three phase set of windings of a multi-three-phase electrical motor. The arrangement affects the system behaviour and, consequently, the control system. The main limitation of the series configuration (Fig. 1.7a) is the fault tolerance; in fact, if a segment is damaged, the entire system is compromised. On the other hand, in the parallel configuration (Fig. 1.7b), due to the replication of the paralleled inverters and the three-phase sets of windings, both

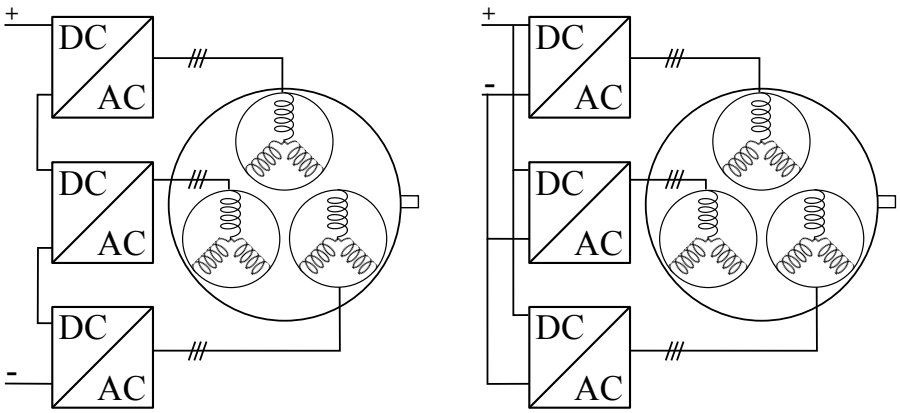

(a) Series configuration. (b) Paralleled configuration.

Figure 1.7: Different drive arrangements for the 2L-3P-VSI inverter.

in case of segment or drive fault, system service is guaranteed. For this reason between the two configurations, the parallel one is the most suitable for IMMD and it has been considered in this thesis. The other relevant design choice is the connection of the neutral points. If the three phase systems are isolated, fault tolerant strategies have been already developed and verified [28, 34]. Contrarily, with one common neutral point, in case of a fault, the system could be reconfigured thanks to additional switches and modified modulation strategies [27, 35, 36]. However, the overall reliability is badly affected by adding extra components, therefore only winding configurations with disconnected neutral points will be considered in this thesis.

1.3 Multi-drive control strategies - State-of-the-art

Nowadays, in multi-drive applications (like for example conveyor systems, large diameter bull gears with multiple drives, printing presses with in-line drive shaft, coal cars, cement kilns, and separator drums) where off-the-shelf three-phase drives are used, power sharing is achieved mainly thanks to three

different control techniques [37, 38]:

- **Common Speed Reference** (Fig. 1.8a);
- **Torque Follower** (Fig. 1.8b);
- **Speed Trim Follower** (Fig. 1.8c).

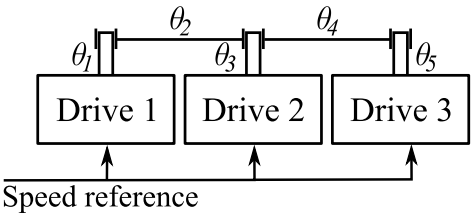

(a) Common Speed Reference (CSR).

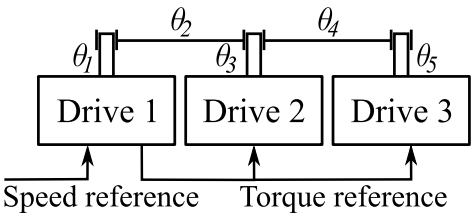

(b) Torque Follower (TF).

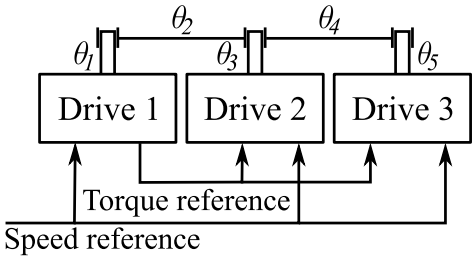

(c) Speed trim follower.

Figure 1.8: Different multi-drive control strategies. θ_1, θ_2, θ_3, θ_4, and θ_5 are not necessarily the same.

In figures 1.8, every drive block is meant to be an industrial controller with a 2L-3P-VSI (Fig. 1.6) connected to an off-the-shelf three phase motor.

The **common speed reference** in Fig. 1.8a is the simplest configuration where all the drives are operated in speed mode and there are no inter-drive connections. Without modifying the firmware of the controller, the power sharing ratio cannot be changed. Thus power is always equally split among the inverters. Since all the drives are independent, the main advantage of such a configuration is its intrinsic fault tolerance.

In the **torque follower** configuration (Fig. 1.8b), interconnections between drives are required [39, 40], and for this reason, it is not modular and not fault tolerant. However, both the load sharing and the speed control are precise [37]. The master drive is operated in speed regulation, whereas the followers are operated in torque regulation mode. This layout is used where coupling among the motors is rigid and speed regulation is critical.

In the **speed trim follower** all the drives are operated with speed regulation (Fig. 1.8c). Whilst the master takes speed reference as it is provided, the followers are added with a trimmed speed. The trim adjusts the speed set-point comparing the local torque set-point with the one from the master. This guarantees equal torque generated by each module. With rigid couplings the torque set-points are the same and no adjustments are encountered. The speed trim follower configuration is adopted when the coupling among motors has a very high potential for oscillation. Since each drive is fed with the torque reference of the master drive, the speed trim follower is not modular. Even if its layout could be reconfigured in case of fault thanks to a supervisory controller, complexity would increase compromising reliability.

Technique	Typical application	Advantages	Disadvantages
Speed reference	Continuous belt conveyor with multiple driven rolls	Simple; No extra wiring for interconnection; High performance drive not required; No runaway condition with load loss;	Poor speed regulation; Limited speed range; Sharing of load not precise;
Torque follower	Coal car, cement kiln, separator drum, large diameter bull gear, printing presses with inline drive shaft	Precise load sharing (act as one); Operation over the entire speed range; Minimum torque mode helps prevent runaway;	Requires a torque regulating drive; Interconnection required; Load loss runaway if torque regulation only;
Speed trim follower	Chain conveyor with different processes, mining or overland conveyor system	Continuous automatic compensation; Operation over the entire speed range; Trim feature built into drive; Speed regulation;	Requires high performance drive for precision; Requires interconnection wiring;

Table 1.2: Current power sharing techniques

In Table 1.2 advantages and disadvantages of the three configurations are summarised. Among the control strategies mentioned above, the only one having independent drives is the the **common speed reference**. For this reason, it is more suitable for IMMD compared to the **torque follower** and the **speed trim follower** configuration.

1.4 Multi-drive control strategies in multi-three-phase motors

The aforementioned configurations can be used to control paralleled converters connected to a single machine with one rotor and multiple three-phase stator windings. Since actuation power is shared among different modules with independent power electronics and isolated windings (Fig. 1.9), if the system is properly re-configured under fault conditions, the overall reliability is improved. Since various faults may occur for different systems, they will not be listed in this thesis. For simplicity, it is assumed that as soon as

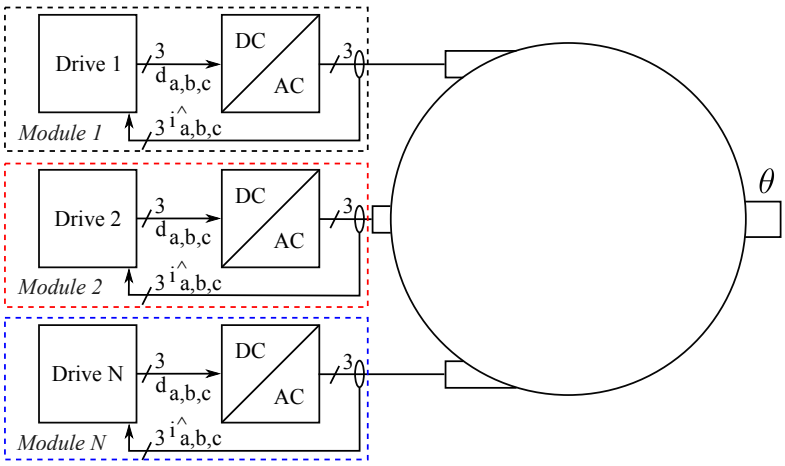

Figure 1.9: Multi-three-phase machine with disconnected neutral points wired to N 2L-3P-VSI (DC/AC blocks). Current feedbacks ($i_a^{\wedge}$,$i_b^{\wedge}$,$i_c^{\wedge}$) are routed to each local drive. d_a,d_b,d_c = duty cycles. θ is the mechanical angle.

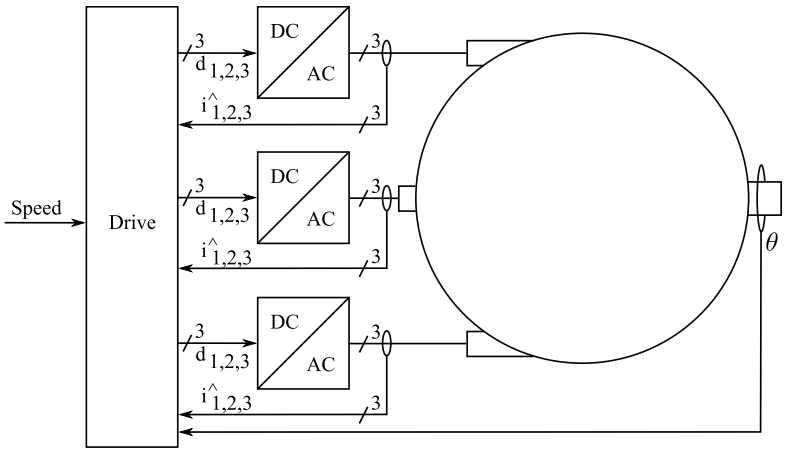

Figure 1.10: Centralised configuration with one single drive processing all the current feedbacks.

the fault is detected thanks to any state-of-of-the-art current fault detection techniques for three-phase AC motor drives [41], the system is able to disconnect the faulty module. In this way, if every module is adequately overrated and properly re-configured to accommodate one or more system failures, the system will be able to maintain operation at nominal power.

In multi-drive industrial plants, the coupling among different motors, either rigid or not, is not ideal. In-fact, even if in small extent, oscillations and skews are always present [42]. Contrarily, in multi-three-phase motors there is just one shaft, therefore there are no mechanical couplings and θ_1, θ_2, θ_3, θ_4, and θ_5 from Fig. 1.8 can be considered all the same and equal to θ in Fig. 1.9. In-fact, in multi-three-phase motors the rotor position information is common to all drives. Since there is just one rotor electromagnetically coupled to multiple sets of windings, the resulting mechanical coupling among the drives can be considered ideal and infinitely rigid. For this reason, as it will be later shown, in multi-three-phase motors there is no difference between the common speed reference and the torque follower configuration.

In configuration shown in Fig. 1.9, only the local currents are fed back to

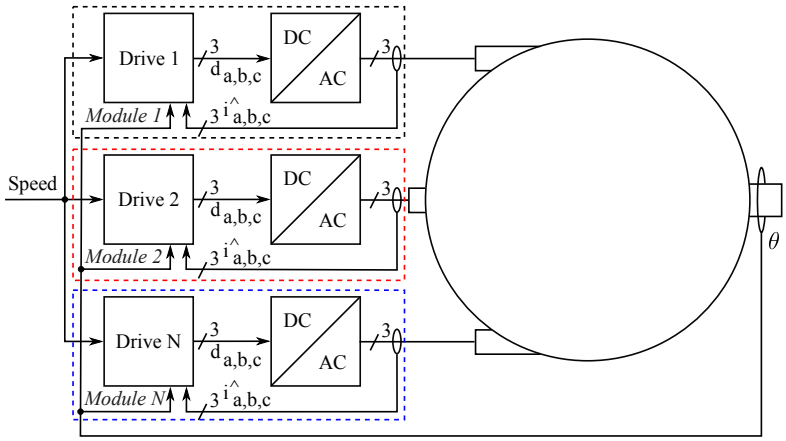

(a) Common Speed Reference configuration (CSR).

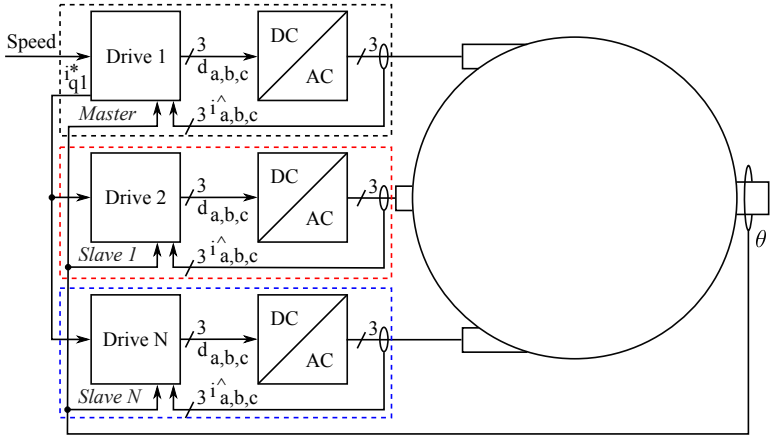

(b) Torque Follower configuration (TF).

Figure 1.11: Multi-drive control strategies comparison.

each drive. Sampling the three local currents, Field Oriented Control (FOC) is implemented like in standard three phase motor control. However, since only local currents are processed, orthonormal sub-spaces cannot be reached. In order to achieve better current dynamics controlling all the orthonormal sub-spaces, multi-three-phase arrangements are based on the so called Vector Space Decomposition (VSD) [43] where all the currents are fed back to one single centralised drive like in Fig. 1.10 [44]. In this configuration, all the currents are fed back to the only drive within the system and the same drive

sets all the duty cycles for all the converters.

Even though the system in Fig. 1.10 allows new control strategies to be studied [45], it is not redundant on the drive side. Contrarily, both configurations in Fig. 1.11 are fully redundant having one drive per converter. Furthermore, *know-how* on three-phase vector-control theory and fault management [41] can be re-used, and eventually combined for developing new control strategies [46] and post-fault counter-measures [27, 28]. Looking at Fig. 1.11, whilst the CSR is distributed, the Torque Follower is centralised. In the latter configuration, the master-drive internal current set-point i_{q1}^{*} within the reference frame is provided as input to the slave-drives. In both configurations every drive processes only its local current feedbacks, but considering the Torque Follower configuration, the system is compromised in case of master drive fault. For this reason, the Torque Follower configuration is not redundant, and therefore it is not suitable for speed controlled Integrated Modular Motor Drives. In Table 1.3 benefits and drawbacks of the aforementioned configurations in terms of redundancy and sub-space controllability are summarised.

Configuration	**Fig.**	**Full redundancy**	**sub-space controllability**
Centralised	1.10	✗	✓
Common Speed Reference	1.11a	✓	✗
Torque Follower	1.11b	✗	✗

Table 1.3: Multi-three-phase configuration comparison

1.5 Possible applications of multi-three-phase motors

In this Section, a circular DC Zonal Electrical Distribution System (ZEDS) proposed in [10] is introduced and further developed for better presenting some of the possibilities enabled by multi-three-phase motors. At the end of this Section, a short list of the most common applications using multi-three-phase machines is given [47].

A standard ZEDS with two three-phase propulsion motors in red, four generators in green, and for sake of clarity with just two electrical zones in yellow is shown in Fig. 1.12 [10]. The switches on the DC ring bus are there

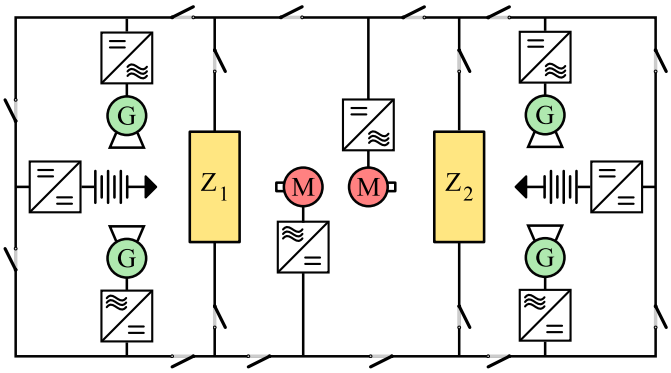

Figure 1.12: State-of-the-art ZEDS with three phase motors.

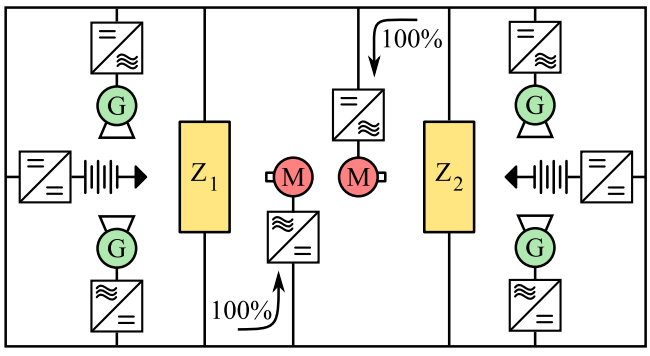

Figure 1.13: State-of-the-art ZEDS during normal operation.

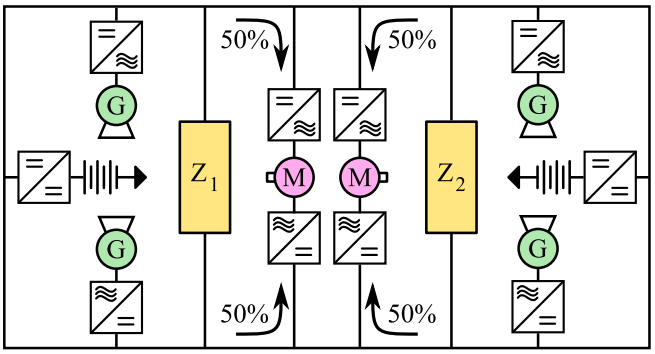

Figure 1.14: Proposed ZEDS with multi-three-phase motors.

to isolate faults that may occur on the buses that distribute power to the zones. During normal operation, the switches are closed like shown in Fig. 1.13. In order to further increase the overall reliability, three-phase motors in the ZEDS from [10] have been replaced by multi-three-phase propulsion motors in magenta as shown in Fig. 1.14 [48]. Obviously, if full redundancy is needed, wires, converters, and motors must be properly over-rated. Doing so, in case of fault, the total delivered power is constant even after a fault occurred. The additional degrees of freedom enabled by the introduction of multi-three-phase motors are listed in the following paragraphs and explained with aid of Figs. 1.15, 1.16,1.17, and 1.18.

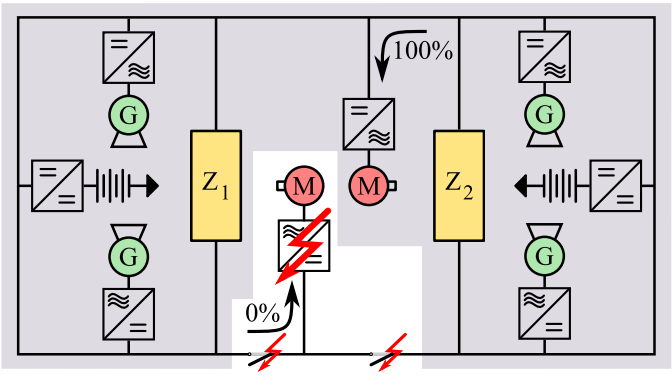

Figure 1.15: State-of-the-art ZEDS in case of fault.

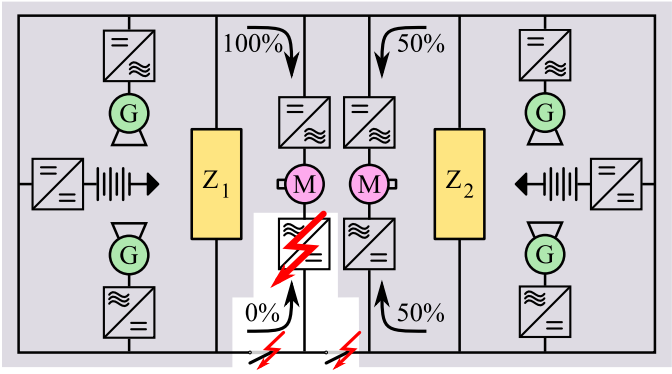

Figure 1.16: Proposed ZEDS in case of fault.

The main advantage introduced by multi-three-phase-motor adoption is higher fault tolerance. For example, in case of fault, whilst the three-phase motor in Fig. 1.15 is compromised, the multi-three-phase motor in Fig. 1.16 in magenta can still operate either in nominal or sub-optimal conditions. Infact, full fault compensation is achieved if and only if motor, wires, generators and converters are properly over-rated.

In Fig. 1.17, the case of two unbalanced isolated DC links is shown. Assuming the system has been properly over-rated, multi-three-phase motors are able to demand different amount of power to (or to share the load between) every DC power source (i.e. 25% and 75%) keeping constant the

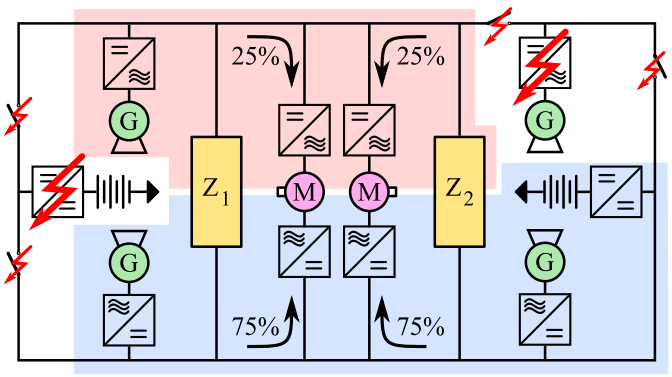

Figure 1.17: Proposed ZEDS - Load sharing among isolated DC-links.

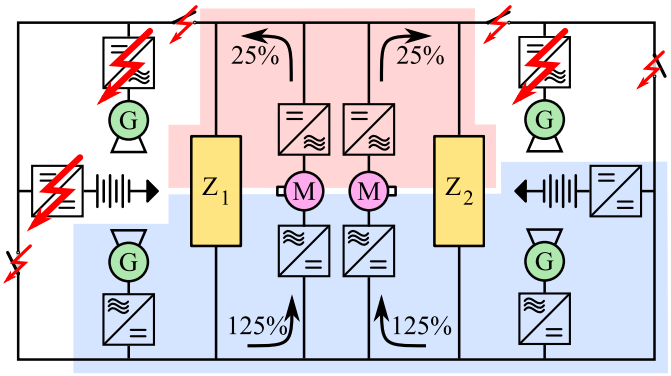

Figure 1.18: Proposed ZEDS - Power flow among isolated DC-Links.

overall power provided to the propulsion units. In this way, multi-three-phase machines adoption does not over-load the top-left generator. Finally, in the unlikely event of faulty generators on the same DC side, thanks to power flow through the multi-three-phase machines, at the same time, power can be delivered to the broken DC-link, while keeping the motors spinning as shown in Fig. 1.18.

1.5.1 List of applications adopting multi-three-phase machines

The following is a list of applications were multi-three-phase machines are adopted the most [47]:

- Road vehicles;
- Aircraft;
- Ships;
- Wind generators;

1.6 Contributions of the thesis

This thesis revises the Vector Space Decomposition method applied to multi-three-phase motors and it verifies the equivalence with the $dq0$ reference frame model under balanced voltage supply condition. The two state-of-the-art control configurations - the common speed reference and the torque follower configuration - are compared. Power sharing achieved with the two state-of-the-art control configurations is improved by a novel Speed-Drooped regulator able to control the power sharing transient while keeping constant the speed of the shaft. Controlling power sharing transients allows current distortions to be minimised improving the Total Harmonic Distortion (THD). Furthermore, controlling power sharing transients minimises vibration extending the life cycle of the overall system.

1.6.1 Organisation of the thesis

The following list summarises the content of every Chapter:

- The next chapter introduces the model of the machine and how the first $d-q$ harmonic inductances are obtained thanks to the Vector Space Decomposition technique.
- In Chapter 3, current control loop design based on the two first harmonic inductances are analytically introduced and simulated by means of Matlab/Simulink simulations.
- In Chapter 4, speed control of multi-three-phase systems is introduced and the two main configurations, the Common Speed Reference in Fig. 1.11a and Torque Follower configuration in Fig. 1.11b, are compared. Their equivalence is further supported by Matlab/Simulink simulations.
- In Chapter 5, power sharing among different modules is introduced. Furthermore, a post-fault compensation strategy assuming constant

current loop bandwidth in case of module fault is analytically described and validated by means of simulations.

- In Chapter 6, the novel Speed-Drooped controller is introduced and formulated. Its capability to control the power sharing transient with different time constants is proved by means of analytical equations and simulations.

- In Chapter 7, experimentally obtained results are presented. All the concepts proposed and validated by numerical simulations in Chapter 6 are experimentally verified on a multi-drive rig with two induction motors on the same shaft.

- In Chapter 8, current and speed control loop designs are validated on a multi-three-phase machine with nine phases. The equivalence between the Common Speed Reference and the Torque Follower configuration is experimentally validated. The speed-drooped controller validation is extended to the multi-three-phase motor where mutual electo-magnetic couplings are present. Furthermore, the proposed speed-droop controller introduced in Chapter 6 is compared against the Common Speed Reference configuration during power sharing transients.

- Finally, Chapter 9 gives the conclusions on the presented work and summarises the contributions of this thesis.

In order to better understand the Vector Space Decomposition, two numerical examples with even and odd number of phases are reported in Appendix A and B, respectively. Some equations for better understanding Chapter 2 are listed in Appendix C.

1.6.2 Publications list

The following publications are results of the research investigations directly related to this thesis:

1. A. Galassini, A. Costabeber, C. Gerada, G. Buticchi and D. Barater, "State space model of a modular speed-drooped system for high reliability integrated modular motor drives," *2015 International Conference on Electrical Systems for Aircraft, Railway, Ship Propulsion and Road Vehicles (ESARS)*, Aachen, 2015, pp. 1-6

2. A. Galassini, A. Costabeber and C. Gerada, "Speed droop control of integrated modular motor drives," *IECON 2015 - 41st Annual Conference of the IEEE Industrial Electronics Society*, Yokohama, 2015, pp. 3271-3276

3. A. Galassini, A. Costabeber, C. Gerada, G. Buticchi, and D. Barater, "A modular speed-drooped system for high reliability integrated modular motor drives," *IEEE Transactions on Industry Applications*, vol. 52, no. 4, pp. 3124–3132, July 2016.

4. A. Galassini, A. Costabeber, M. Degano, C. Gerada, A. Tessarolo, and S. Castellan, "Distributed current control for multi-three-phase synchronous machines in fault conditions," in *2016 XXII International Con- ference on Electrical Machines (ICEM)*, Sept 2016, pp. 1036–1042

5. A. Galassini, G. L. Calzo, A. Formentini, C. Gerada, P. Zancehtta, and A. Costabeber, "uCube: Control platform for power electronics," *2017 IEEE Workshop on Electrical Machines Design, Control and Diagnosis (WEMDCD)*, Nottingham, April 2017

6. A. Galassini, A. Costabeber, and C. Gerada, "Speed Control for Multi-Three-Phase Synchronous Electrical Motors in Fault Condition", *2017*

IEEE International Conference on Smart Technologies (EUROCON), Ohrid, July 2017

7. A. Galassini, A. Costabeber, C. Gerada, and A. Tessarolo, "Distributed Speed-Control for Multi-Three- Phase Electrical Motors with Improved Power Sharing Capability", *2017 IEEE Energy Conversion Congress and Expo (ECCE)*, Cincinnati, Oct 2017

8. A. Galassini, A. Costabeber, C. Gerada, A. Tessarolo, and R. Menis "Speed Control with Load Sharing Capabilities for Multi-Three-Phase Synchronous Motors", *IECON 2017 - 43rd Annual Conference of the IEEE Industrial Electronics Society*, Beijing, Nov 2017

Chapter 2

Machine Modelling

The aim of this Chapter is to revise the Park's transformation and the Vector Space Decomposition for multi-three-phase electrical motors in order to better understand content of Chapter 3. Unfortunately, the Park's transformation does not decouple the mutual interactions between different sets of windings within multi-three-phase machines. De-coupled torque, flux and zero-sequence control within the $dq0$ reference frame is possible only with de-coupled transfer functions linking every output current to its relative input voltage. For this reason, diagonalisation of the inductance matrix must be performed, either numerically or analytically. The values on the diagonal are the j-th order harmonic inductances of the stator system, defined as the inductances the stator exhibits when subjected to a symmetrical supply voltage system.

In order to better understand the distributed current control presented in the next Chapter, the physical and analytical bases behind the multi-three-phase electrical machine modelling discussed in [49] are revised here.

2.1 Multi-three-phase electrical motors

In this section, the multi-three-phase motor definition is given and the specific configuration discussed in this thesis is introduced.

Multi-three-phase electrical motors are a particular group of electrical machines. Defining m the number of phases per isolated set of windings, in multi-three-phase motors $m = 3$ (phases a, b, and c in Fig. 2.1a, 2.1b). Therefore, defining N the number of sets of windings, the total number of phases is equal to $n = Nm$. In Fig. 2.1, two possible winding arrangements for multi-three-phase motors are shown. In Fig. 2.1a, the split-phase

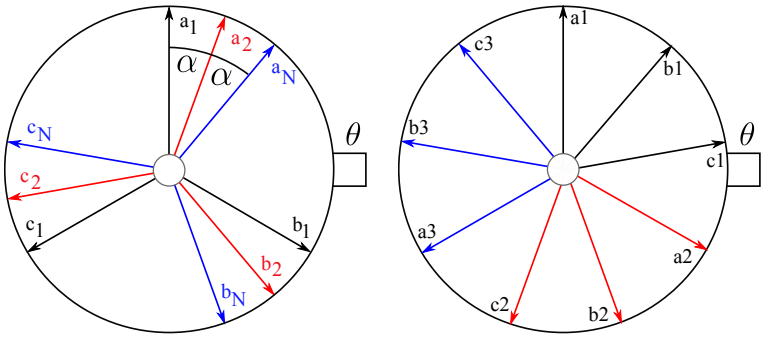

(a) Split-phase (b) Segmented

Figure 2.1: Different multi-three-phase winding arrangements.

winding arrangement is shown, where $\alpha = \pi/n$ is the phase progression between the first phase a of every set of windings. In Fig. 2.1b, the segmented winding arrangement is shown. In both configurations, the neutral points of every three-phase set of windings are disconnected. The segmented winding arrangement is usually adopted in machine with self-levitating rotor capability. On the other hand, it presents higher torque ripple if compared to the split-phase winding arrangement [50, 51, 52].

For simplicity, this thesis will discuss only the split-phase arrangement in Fig. 2.1a. However, the proposed approach and *modus operandi* could be applied also to segmented machines or to any other winding arrangement.

2.2 Modelling assumptions

The work presented in this thesis is based on the assumption that stator inductances are constant. Therefore, it applies to electric machines with negligible saturation effects. In addition it is assumed that:

- all phases are geometrically identical;
- each phase is symmetrical around its magnetic axis;
- the spatial displacement between two whatever phases is an integer multiple of the phase progression α (Fig.2.1a);
- within the air-gap, only the fundamental component of magneto-motive force is considered.

No restrictive assumption is made about whether the winding is distributed or concentrated [53, 54, 55].

2.3 Analytical model in Park's coordinates

Current control of distributed configuration like the one in Fig. 1.9 is achieved within the rotor-attached orthogonal $dq0$ reference frame thanks to the Park's transformation relating machine stator variables (denoted with subscript abc) to the $dq0$ ones (denoted with subscript dq).

In a distributed configuration like the one in Fig.2.2, there is one controller per three phase set of windings and only the three local currents are provided as feedback. Since the machine is made by multiple three phase systems, the global $n \times n$ Park's transformation matrix is given by (2.1), where $\mathbf{0}_3$ is a 3×3 null matrix, and θ is the rotor position:

$$\mathbf{T}_{Park} = \begin{pmatrix} \mathbf{T}_1 & \cdots & \mathbf{0}_3 \\ \vdots & \ddots & \vdots \\ \mathbf{0}_3 & \cdots & \mathbf{T}_N \end{pmatrix}_{n \times n} \tag{2.1}$$

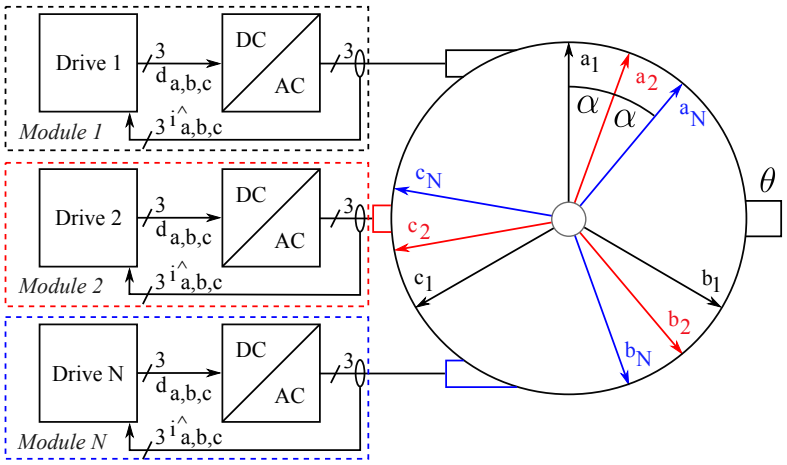

Figure 2.2: Nine phase ($n = 9$) multi-three-phase machine with disconnected neutral points wired to three ($N = 3$) 2L-3P-VSI (DC/AC blocks). Current feedbacks ($i_a^\wedge$,$i_b^\wedge$,$i_c^\wedge$) are routed to the relative local drive. $\alpha = \pi/n = 20°$. For simplicity, θ feedback is omitted.

Sub-matrices on the diagonal of (2.1) are defined as:

$$\mathbf{T}_h(\theta, h, \alpha) = \sqrt{\frac{2}{3}} \begin{pmatrix} \cos[\theta-(h-1)\alpha] & \sin[\theta-(h-1)\alpha] & 0 \\ -\sin[\theta-(h-1)\alpha] & \cos[\theta-(h-1)\alpha] & 0 \\ 0 & 0 & 1 \end{pmatrix} \times \\ \times \begin{pmatrix} 1 & -1/2 & -1/2 \\ 0 & \sqrt{3}/2 & -\sqrt{3}/2 \\ 1/\sqrt{2} & 1/\sqrt{2} & 1/\sqrt{2} \end{pmatrix} \text{ with } h = 1..N \tag{2.2}$$

The whole set of machine variables can be thus transformed into the $dq0$ reference frame. The machine voltage equation in the new coordinate system is:

$$\mathbf{v}_{dq} = \mathbf{R}_{dq}\mathbf{i}_{dq} + \omega\mathbf{J}\mathbf{L}_{dq}\mathbf{i}_{dq} + \mathbf{L}_{dq}\frac{d\mathbf{i}_{dq}}{dt} + \mathbf{e}_{dq} \tag{2.3}$$

with

$$\mathbf{v}_{dq} = \begin{bmatrix} \mathbf{v}_{dq1} \\ \vdots \\ \mathbf{v}_{dqN} \end{bmatrix}; \quad \mathbf{i}_{dq} = \begin{bmatrix} \mathbf{i}_{dq1} \\ \vdots \\ \mathbf{i}_{dqN} \end{bmatrix}; \quad \mathbf{e}_{dq} = \begin{bmatrix} \mathbf{e}_{dq1} \\ \vdots \\ \mathbf{e}_{dqN} \end{bmatrix} \tag{2.4}$$

where

$$\begin{aligned}
\mathbf{v}_{dqh} &= \begin{bmatrix} v_{dh} \\ v_{qh} \\ v_{0h} \end{bmatrix} = \mathbf{T}_h \begin{bmatrix} v_{ah} \\ v_{bh} \\ v_{ch} \end{bmatrix}; \quad \mathbf{i}_{dqh} = \begin{bmatrix} i_{dh} \\ i_{qh} \\ i_{0h} \end{bmatrix} = \mathbf{T}_h \begin{bmatrix} i_{ah} \\ i_{bh} \\ i_{ch} \end{bmatrix} \\
\mathbf{e}_{dqh} &= \begin{bmatrix} e_{dh} \\ e_{qh} \\ e_{0h} \end{bmatrix} = \omega \frac{d}{dt} \begin{bmatrix} \phi_{dh} \\ \phi_{qh} \\ \phi_{0h} \end{bmatrix} = \mathbf{T}_h \begin{bmatrix} e_{ah} \\ e_{bh} \\ e_{ch} \end{bmatrix} \text{ with } h = 1..N
\end{aligned} \tag{2.5}$$

$\mathbf{v}_{dq}$, $\mathbf{i}_{dq}$ and $\mathbf{e}_{dq}$ are respectively voltage, current and back electromotive force vectors $n \times 1$. $\mathbf{R}_{dq}$ and $\mathbf{L}_{dq}$ are respectively resistance and inductance matrices $n \times n$, the angular speed is $\omega = d\theta/dt$, and

$$\mathbf{J} = \begin{pmatrix} \mathbf{J}_1 & \cdots & \mathbf{0}_3 \\ \vdots & \ddots & \vdots \\ \mathbf{0}_3 & \cdots & \mathbf{J}_N \end{pmatrix}; \mathbf{J}_h = \mathbf{T}_h \frac{d\mathbf{T}_h^T}{d\theta} = \begin{pmatrix} 0 & -1 & 0 \\ 1 & 0 & 0 \\ 0 & 0 & 0 \end{pmatrix} \tag{2.6}$$

where ^{T} is the transpose operator. More precisely, $\mathbf{R}_{abc} = \mathbf{R}_{dq} = r_s \mathbf{I}_{(n \times n)}$ where r_s is the stator phase resistance and $\mathbf{I}$ is the identity matrix, whereas

$$\begin{aligned}
\mathbf{L}_{dq} &= \begin{pmatrix} \mathbf{L}_{dq(1,1)} & \cdots & \mathbf{L}_{dq(1,N)} \\ \vdots & \ddots & \vdots \\ \mathbf{L}_{dq(N,1)} & \cdots & \mathbf{L}_{dq(N,N)} \end{pmatrix} = \mathbf{T}_{Park} \mathbf{L}_{abc} \mathbf{T}_{Park}^T \\
&\text{with } \mathbf{L}_{dq(i,j)} = \mathbf{L}_{dq(j,i)}^T = \mathbf{T}_h \mathbf{L}_{abc(i,j)} \mathbf{T}_h^T = \\
&= \frac{3}{2} \begin{pmatrix} L_{md} & 0 & 0 \\ 0 & L_{mq} & 0 \\ 0 & 0 & 0 \end{pmatrix} + \begin{pmatrix} M_{i-j} & -X_{i-j} & 0 \\ X_{i-j} & M_{i-j} & 0 \\ 0 & 0 & H_{i-j} \end{pmatrix}
\end{aligned} \tag{2.7}$$

where L_{md} and L_{mq} are d, q magnetizing inductances. Considering the rotor $dq0$ reference frame, parameters M_k and X_k are the mutual stator leakage inductances, whilst H_k are the homo-polar stator leakage inductances. Their *physical* meaning is schematically shown in Fig. 2.3 (where i and j are the stator set identifiers $1..N$) and they can be calculated with finite element

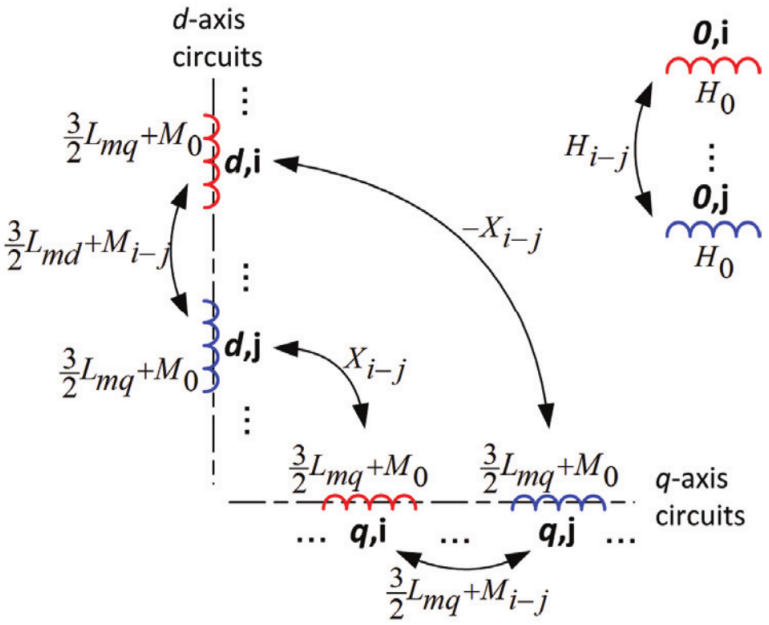

Figure 2.3: Homo-polar (H_{i-j}) and mutual (M_{i-j}, X_{i-j}) leakage inductances corresponding to the i-th and j-th stator three-phase set.

analysis or analytical formulation [56, 57]. In particular, it can be seen that the mutual leakage inductance X_{i-j} couples the d-axis circuit corresponding to the j-th set with the q-axis circuit corresponding to the i-th set of windings. It is worth to notice that d-q cross coupling depends on leakage fluxes alone and may occur only between d and q circuits representing different stator sets (i.e. only if $i \neq j$, hence $X_{0-0} = 0$). M_0 is the self-leakage inductance. $\mathbf{L}_{dq}$ matrices for stators with even and odd number of phases are reported in (A.2) and (B.2), respectively.

Since $\mathbf{L}_{dq}$ in (2.7) is not diagonal, every q output current is function of multiple q input voltages. In other words, within the $dq0$ reference frame, an one-to-one relation between output currents and input voltages is not obtained by simply transforming stator variables with the Park's transformation. For this reason, assuming balanced supply conditions, the RL plants within the $dq0$ reference frame are not known, and it is not possible to set

up any current controller for a plant like the one in Fig. 2.4.

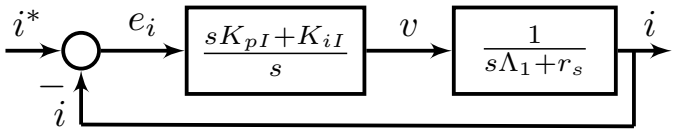

Figure 2.4: Equivalent current plant within the synchronous reference frame with phase resistance r_s and unknown inductance (Λ_1). K_{pI} and K_{iI} are the proportional and the integral current controller gains, respectively.

Assuming balanced supply conditions, the PI controller in Fig. 2.4 can be designed considering the first harmonic inductance (Λ_1) obtained by diagonalising the $\mathbf{L}_{dq}$ matrix either numerically computing the eigenvalues and the eigenvectors, or analytically thanks to the Vector Space Decomposition revised in the next section.

2.4 Vector Space Decomposition

The aim of this section is at recalling the VSD method detailed in [49, 54, 55, 58] which applies to both symmetrical and asymmetrical n-phase winding schemes, for whatever integer n-greater than three.

The Vector Space Decomposition (VSD) is a modelling technique which has been widely applied to multi-phase machines, with both split-phase [43, 59] and symmetrical [60, 61] stator winding configurations. Its theoretical foundation can be traced back to the Fortescue Symmetrical Component (SC) theory for poly-phase systems [62]. In fact, it is well known that, when applied to an ideal round-rotor symmetrical n-phase machine, the Symmetrical Component transformation is capable of decomposing its model into n-1 fully-decoupled component models [63]. From an algebraic viewpoint, this means that the machine phase inductance matrix after transformation assumes a diagonal time-invariant structure, which is suitable for control synthesis purposes.

In [49], it is proposed that the VSD transformation $\mathbf{T}_{vsd}$ should consist of two cascaded steps:

1. The first is a merely geometrical transformation ($\mathbf{W}$) capable of mapping the actual winding structure into a conventional one (Fig. 2.5b); the precise meaning of this mapping operation will be clarified in subsection 2.4.1;

2. The second is a decoupling transformation matrix (represented by $\mathbf{T}_d(\theta)$ where θ is the rotor position) to be applied to the conventional machine model. Such transformation is meant to project machine variables onto a set of mutually orthogonal subspaces and it will be detailed in subsection 2.4.2.

The overall VSD transformation $\mathbf{T}_{vsd}(\theta) = \mathbf{T}_d(\theta)\mathbf{W}$ will then result from combining the two transformations. The advantage of this approach is that the properly called VSD theory can be developed only for the conventional multi-phase model in Fig. 2.5b (thereby making abstraction of the particular phase arrangement of the actual machine), instead of tailoring VSD procedures on any particular multi-phase winding topology that may occur in practice like the one in Fig. 2.5a.

2.4.1 Geometrical transformation matrix

The conventional n-winding arrangement selected for the purpose is shown in Fig. 2.5b and it entails n phases numbered from 1 to n and sequentially arranged over a pole span with a phase progression angle $\alpha = \pi/n$. With such a choice, any n-phase winding (whether symmetrical or asymmetrical, with even or odd phase count) can be mapped into a conventional n-phase arrangement such as that in Fig. 2.5b by means of a geometrical transformation $\mathbf{W}$.

Considering the case of an asymmetrical split-phase scheme composed of N symmetrical three-phase sections shown in Fig.2.5a, either with even or odd number of phases $n = mN$, Eq. (2.8) maps the scheme in Fig.2.5a into the asymmetrical n-phase scheme in Fig.2.5b (denoted by $_{std}$).

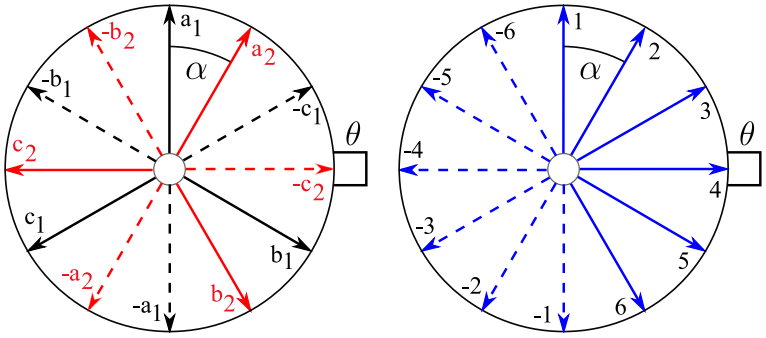

(a) Split-phase scheme (denoted by *abc*).

(b) n-phase equivalent scheme (denoted by $_{std}$).

Figure 2.5: The **W** matrix maps the split-phase winding scheme, either with even or odd number of phases shown in Fig.2.5a, into the n-phase equivalent scheme with the same phase progression α, shown in Fig.2.5b.

The geometrical transformation matrix can be defined as:

$$\mathbf{W}_{(i,j)} = \begin{cases} 1 & \text{if } i - \text{trunc}(\frac{j-1}{m}) - 2N\text{mod}(j-1,m) - 1 = 0 \\ -1 & \text{if } |i - \text{trunc}(\frac{j-1}{m}) - 2N\text{mod}(j-1,m) - 1| = mN \\ 0 & \text{otherwise} \end{cases} \quad (2.8)$$

In (2.8), trunc(x) is the largest integer less then or equal to x, mod(x, y) is the remainder on dividing x by y, and i, j are row and column identifiers [55]. The phase progression in asymmetrical n-phase schemes is the same one of split-phase schemes ($\alpha = \pi/n$). In Fig.2.5, for graphical simplicity $N = 2$ ($m = 3$, $n = 6$, $\alpha = \pi/n$) but the same applies to asymmetrical split-phase scheme composed by $N > 2$ symmetrical three-phase sections. In Appendices A and B numerical examples for the case of $n = 12$ and $n = 9$ are reported, respectively.

2.4.2 Decoupling transformation matrix

Considering an asymmetrical poly-phase machine with n sequentially distributed phases (Fig. 2.5b) at steady-state operation under balanced supply at constant electrical pulsation ω, phase quantities (currents, voltages, flux linkages, etc.) are periodic function of time and can be expressed as Fourier series. Calling y_{std} the generic phase variable vector in the conventional multiphase arrangement in Fig. 2.5b and calling $\mathbf{y}_k(t)$ the value of such variable in phase k at instant t, one can define:

$$\mathbf{y}_{std}(t) = \begin{pmatrix} y_0(t) \\ y_1(t) \\ y_2(t) \\ \vdots \\ y_{n-1}(t) \end{pmatrix} = \begin{pmatrix} \sum\limits_{h=h_1,h_2,h_3,\ldots} Y_h \cos[h\omega t - \phi_h] \\ \sum\limits_{h=h_1,h_2,h_3,\ldots} Y_h \cos[h(\omega t - \alpha) - \phi_h] \\ \sum\limits_{h=h_1,h_2,h_3,\ldots} Y_h \cos[h(\omega t - 2\alpha) - \phi_h] \\ \vdots \\ \sum\limits_{h=h_1,h_2,h_3,\ldots} Y_h \cos\{h[\omega t - (n-1)\alpha] - \phi_h\} \end{pmatrix} \tag{2.9}$$

where Y_h and ϕ_h are the h^{th} time harmonic amplitude and phase and h_1, h_2, h_3, ... are harmonic orders which appear in the phase quantities. Let us suppose to apply a time-invariant variable transformation $\mathbf{Q}$ and call $\mathbf{y}_{\alpha\beta}(t)$ the transformed variable vector:

$$\mathbf{y}_{\alpha\beta}(t) = \begin{pmatrix} y_{\alpha h_1}(t) \\ y_{\beta h_1}(t) \\ \hdashline y_{\alpha h_2}(t) \\ y_{\beta h_2}(t) \\ \hdashline y_{\alpha h_3}(t) \\ y_{\beta h_3}(t) \\ \hdashline \vdots \end{pmatrix} = \mathbf{Q} \begin{pmatrix} y_0(t) \\ y_1(t) \\ y_2(t) \\ \vdots \\ y_{n-1}(t) \end{pmatrix} \tag{2.10}$$

For transformation $\mathbf{Q}$ to perform a VSD, it is required that the couple of variables $y_{\alpha h}$, $y_{\beta h}$ represent the h^{th} harmonic space vector while not depending on any other harmonic component. In other words, $y_{\alpha h}$, $y_{\beta h}$ shall be the

components of a space vector of amplitude proportional to Y_h which rotates at $h\omega$ electrical radians per second in the $\alpha h - \beta h$ plane.

In order to find the appropriate form of $\mathbf{Q}$ which leads to VSD, let us expand 2.9 as follows[1]:

$$\mathbf{y}_{std}(t) = \sum_{h=h_1,h_2,h_3,\ldots} Y_h \begin{pmatrix} \cos[h\omega t - \phi_h] \\ \cos(h\omega t - \phi_h)\cos(h\alpha) + \sin(h\omega t - \phi_h)\sin(h\alpha) \\ \cos(h\omega t - \phi_h)\cos(2h\alpha) + \sin(h\omega t - \phi_h)\sin(2h\alpha) \\ \vdots \\ \cos(h\omega t - \phi_h)\cos[(n-1)h\alpha] + \sin(h\omega t - \phi_h)\sin[(n-1)h\alpha] \end{pmatrix} =$$

$$= \sum_{h=h_1,h_2,h_3,\ldots} Y_h \left\{ \cos(h\omega t - \phi_h) \begin{pmatrix} 1 \\ \cos(h\alpha) \\ \cos(h2\alpha) \\ \vdots \\ \cos[(n-1)h\alpha] \end{pmatrix} + \sin(h\omega t - \phi_h) \begin{pmatrix} 0 \\ \sin(h\alpha) \\ \sin(h2\alpha) \\ \vdots \\ \sin[(n-1)h\alpha] \end{pmatrix} \right\} \tag{2.11}$$

Defining the vectors:

$$\mathbf{c}_h = \begin{pmatrix} 1 \\ \cos(h\alpha) \\ \cos(h2\alpha) \\ \vdots \\ \cos[(n-1)h\alpha] \end{pmatrix}, \qquad \mathbf{s}_h = \begin{pmatrix} 0 \\ \sin(h\alpha) \\ \sin(h2\alpha) \\ \vdots \\ \sin[(n-1)h\alpha] \end{pmatrix} \tag{2.12}$$

equation (2.9) can be re-written as:

$$\mathbf{y}_{std}(t) = \sum_{h=h_1,h_2,h_3,\ldots} Y_h\{\cos(h\omega t - \phi_h)\mathbf{c}_h + \sin(h\omega t - \phi_h)\mathbf{s}_h\} \tag{2.13}$$

Decoupling transformation into a stationary orthonormal reference frame

Let us suppose that ν time harmonics (of orders h_1, h_2, ... h_ν) are present in n phase variables with:

$$\begin{aligned} \nu &= \frac{n}{2} \text{ if } n \text{ is even} \\ \nu &= \frac{n-1}{2} \text{ if } n \text{ is odd} \end{aligned} \tag{2.14}$$

[1] see angle subtraction formula in Appendix C

As a candidate for the VSD transformation through (2.10), let us consider matrices $\mathbf{Q}_e$ for even and $\mathbf{Q}_o$ for odd n, defined as follows in terms of vectors (2.12):

$$\mathbf{Q}_{\mathbf{e}h_1..h_\nu} = \sqrt{\frac{2}{n}} \begin{pmatrix} \mathbf{c}_{h_1}^T \\ \mathbf{s}_{h_1}^T \\ \hdashline \mathbf{c}_{h_2}^T \\ \mathbf{s}_{h_2}^T \\ \hdashline \vdots \\ \hdashline \mathbf{c}_{h_\nu}^T \\ \mathbf{s}_{h_\nu}^T \end{pmatrix}, \qquad \mathbf{Q}_{\mathbf{o}h_1..h_\nu} = \sqrt{\frac{2}{n}} \begin{pmatrix} \mathbf{c}_{h_1}^T \\ \mathbf{s}_{h_1}^T \\ \hdashline \mathbf{c}_{h_2}^T \\ \mathbf{s}_{h_2}^T \\ \hdashline \vdots \\ \hdashline \mathbf{c}_{h_\nu}^T \\ \mathbf{s}_{h_\nu}^T \\ \hdashline \frac{1}{\sqrt{2}}\mathbf{c}_n^T \end{pmatrix} \tag{2.15}$$

An alternative and frequently used form of (2.15) utilizes coefficient $2/n$ in front of the vectors. In such a case, powers per phase of the original and new machine are kept invariant in the transformation, but not the total powers [64].

With aid of (B.4) and (2.12) it can be seen that, in case of odd n, the last row of $\mathbf{Q}_{\mathbf{o}h_1..h_\nu}$ is set as a constant row equal to:

$$\sqrt{\frac{2}{n}}\frac{1}{\sqrt{2}}\mathbf{c}_n^T = \left[\sqrt{\frac{2}{n}}\frac{1}{\sqrt{2}} \; (-\sqrt{\frac{2}{n}}\frac{1}{\sqrt{2}}) \; \sqrt{\frac{2}{n}}\frac{1}{\sqrt{2}} \; (-\sqrt{\frac{2}{n}}\frac{1}{\sqrt{2}}) \; \cdots\right] \tag{2.16}$$

Since the definition of $\mathbf{Q}_{h_1..h_\nu}$ is not univocal, but it depends on the set of ν odd integers $h_1..h_\nu$, the question arises as to whether the choice of these ν integers is free or subject to any restrictions. To answer this question, we need to define the properties which we want matrix transformation $\mathbf{Q}_{h_1..h_\nu}$ to have. For the reasons which will be better explained in Chapter 3, we require that matrix $\mathbf{Q}_{h_1..h_\nu}$ be orthonormal, i.e. invertible and such that its inverse coincides with its transpose. In symbols the following condition must hold:

$$\mathbf{Q}_{h_1..h_\nu}^T \mathbf{Q}_{h_1..h_\nu} = \mathbf{Q}_{h_1..h_\nu} \mathbf{Q}_{h_1..h_\nu}^T = \mathbf{I} \tag{2.17}$$

where $\mathbf{I}$ is the $n \times n$ identity matrix. Proof that matrix $\mathbf{Q}_{h_1..h_\nu}$ defined as per (2.15) is guaranteed to be orthonormal can be found in [49] at page 191. The task is still left to check that $\mathbf{Q}_{h_1..h_\nu}$ accomplishes the VSD. For this purpose, let us suppose that the phase variable $\mathbf{y}_{\alpha\beta}(t)$ contains the set of time harmonics of orders $h_1..h_\nu$ and combine (2.10) with (2.13), obtaining:

$$\begin{aligned}\mathbf{y}_{\alpha\beta}(t) &= \mathbf{Q}_{h_1..h_\nu} \sum_{h=h_1..h_\nu} Y_h\{\cos(h\omega t - \phi_h)\mathbf{c}_h + \sin(h\omega t - \phi_h)\mathbf{s}_h\} = \\ &= \sum_{h=h_1..h_\nu} Y_h\{\cos(h\omega t - \phi_h)\mathbf{Q}_{h_1..h_\nu}\mathbf{c}_h + \sin(h\omega t - \phi_h)\mathbf{Q}_{h_1..h_\nu}\mathbf{s}_h\}\end{aligned} \tag{2.18}$$

It can be proved that:

$$\mathbf{Q}_{h_1..h_\nu}\mathbf{c}_{h_i} = \begin{pmatrix} \begin{matrix} 0 \\ \vdots \\ 0 \end{matrix} \text{ 2(i-1) rows} \\ \hdashline \begin{matrix} 1 \\ 0 \end{matrix} \\ \hdashline \begin{matrix} 0 \\ \vdots \\ 0 \end{matrix} \end{pmatrix}, \quad \mathbf{Q}_{h_1..h_\nu}\mathbf{s}_{h_i} = \begin{pmatrix} \begin{matrix} 0 \\ \vdots \\ 0 \end{matrix} \text{ 2(i-1) rows} \\ \hdashline \begin{matrix} 0 \\ 1 \end{matrix} \\ \hdashline \begin{matrix} 0 \\ \vdots \\ 0 \end{matrix} \end{pmatrix} \tag{2.19}$$

Therefore, (2.18) can be written as:

$$\begin{aligned}\mathbf{y}_{\alpha\beta}(t) = \begin{pmatrix} y_{\alpha h_1}(t) \\ \hdashline y_{\beta h_1}(t) \\ \hdashline y_{\alpha h_2}(t) \\ y_{\beta h_2}(t) \\ \hdashline y_{\alpha h_3}(t) \\ y_{\beta h_3}(t) \\ \hdashline \vdots \end{pmatrix} &= \sqrt{\frac{2}{n}} \sum_{i=h_1..h_\nu} Y_h \begin{pmatrix} \begin{matrix} 0 \\ \vdots \\ 0 \end{matrix} \text{ 2(i-1) rows} \\ \hdashline \cos(h_i\omega t - \phi_{h_i}) \\ \sin(h_i\omega t - \phi_{h_i}) \\ \hdashline 0 \\ \vdots \\ 0 \end{pmatrix} \\ &= \sqrt{\frac{2}{n}} Y_h \begin{pmatrix} \cos(h_1\omega t - \phi_{h_1}) \\ \sin(h_1\omega t - \phi_{h_1}) \\ \hdashline \cos(h_2\omega t - \phi_{h_2}) \\ \sin(h_2\omega t - \phi_{h_2}) \\ \hdashline \cos(h_3\omega t - \phi_{h_3}) \\ \sin(h_3\omega t - \phi_{h_3}) \\ \hdashline \vdots \end{pmatrix}\end{aligned} \tag{2.20}$$

from which we obtain:

$$\begin{pmatrix} y_{\alpha h}(t) \\ y_{\beta h}(t) \end{pmatrix} = \sqrt{\frac{2}{n}} Y_h \begin{pmatrix} \cos(h\omega t - \phi_h) \\ \sin(h\omega t - \phi_h) \end{pmatrix} \tag{2.21}$$

for any $h\epsilon\{h_1..h_\nu\}$. This means that, at steady state, the couple of transformed variables $y_{\alpha h}$ and $y_{\beta h}$ actually describe only the h^{th} time harmonic of phase variables. Such harmonic is in fact represented by a space vector of amplitude $\sqrt{2/n}Y_h$ which revolves at speed $h\omega$ in the $\alpha h - \beta h$ plane.

In conclusion, in this Section it has been shown that $\mathbf{Q}_{h_1..h_\nu}$ is an orthonormal matrix and is suitable for decoupling machine time harmonics of orders $h_1..h_\nu$ by projecting them onto independent subspaces. The transformed reference frame is composed by a set of stationary $\alpha h - \beta h$ orthogonal axis pairs, such that the h^{th} order harmonic is represented by a space vector rotating at $h\omega$ electrical speed in the $\alpha h - \beta h$ plane.

Decoupling transformation into rotating reference frames

For FOC implementation, it is useful to accomplish the VSD so that the generic h^{th} order time harmonic is mapped into a constant (fixed) space vector in the $dh - qh$ subspace. This can be achieved by replacing the stationary $\alpha h - \beta h$ orthogonal axes with a couple of revolving axes $dh - qh$ which rotate at speed $h\omega$. The two versors $\hat{\mathbf{u}}_{dh}$ and $\hat{\mathbf{u}}_{qh}$ of the $dh - qh$ reference frame have equations:

$$\hat{\mathbf{u}}_{dh} = \begin{pmatrix} \cos(\omega h t) \\ \sin(\omega h t) \end{pmatrix}, \quad \hat{\mathbf{u}}_{qh} = \begin{pmatrix} -\sin(\omega h t) \\ \cos(\omega h t) \end{pmatrix} \tag{2.22}$$

The coordinates of space vector (2.21), representing the h^{th} order harmonic, written in the new rotating $dh - qh$ reference frame defined by (2.22)

are[2]:

$$\begin{pmatrix} y_{dh}(t) \\ y_{qh}(t) \end{pmatrix} = \left(\begin{array}{c} \hat{\mathbf{u}}_{dh}^T \begin{pmatrix} y_{\alpha h}(t) \\ y_{\beta h}(t) \end{pmatrix} \\ \hdashline \hat{\mathbf{u}}_{qh}^T \begin{pmatrix} y_{\alpha h}(t) \\ y_{\beta h}(t) \end{pmatrix} \end{array}\right) = \begin{pmatrix} \hat{\mathbf{u}}_{dh}^T \\ \hat{\mathbf{u}}_{qh}^T \end{pmatrix} \begin{pmatrix} y_{\alpha h}(t) \\ y_{\beta h}(t) \end{pmatrix} =$$

$$= \begin{pmatrix} \cos(\omega h t) & \sin(\omega h t) \\ -\sin(\omega h t) & \cos(\omega h t) \end{pmatrix} \sqrt{\frac{2}{n}} Y_h \begin{pmatrix} \cos(\omega h t - \phi_h) \\ \sin(\omega h t - \phi_h) \end{pmatrix} = \sqrt{\frac{2}{n}} Y_h \begin{pmatrix} \cos(\phi_h) \\ -\sin(\phi_h) \end{pmatrix} \tag{2.23}$$

Writing (2.23) for all $h \epsilon \{h_1..h_\nu\}$ and resorting to matrix notation, the entire variable vector $\mathbf{y}_{dq}(t)$ in the rotating reference frame $dh-qh$ can be obtained from the vector $\mathbf{y}_{\alpha\beta}(t)$ in the stationary reference frames $\alpha h - \beta h$ as follows:

$$\left(\begin{array}{c} y_{dh_1}(t) \\ y_{qh_1}(t) \\ \hdashline y_{dh_2}(t) \\ y_{qh_2}(t) \\ \hdashline y_{dh_3}(t) \\ y_{qh_3}(t) \\ \hdashline \vdots \end{array}\right) = \sqrt{\frac{2}{n}} \left(\begin{array}{c} Y_{h_1}\cos(\phi_{h_1}) \\ -Y_{h_1}\sin(\phi_{h_1}) \\ \hdashline Y_{h_2}\cos(\phi_{h_2}) \\ -Y_{h_2}\sin(\phi_{h_2}) \\ \hdashline Y_{h_3}\cos(\phi_{h_3}) \\ -Y_{h_3}\sin(\phi_{h_3}) \\ \hdashline \vdots \end{array}\right) =$$

$$\left(\begin{array}{cc:cc:cc:c} \cos(\omega h_1 t) & \sin(\omega h_1 t) & 0 & 0 & 0 & 0 & \cdots \\ -\sin(\omega h_1 t) & \cos(\omega h_1 t) & 0 & 0 & 0 & 0 & \cdots \\ \hdashline 0 & 0 & \cos(\omega h_2 t) & \sin(\omega h_2 t) & 0 & 0 & \cdots \\ 0 & 0 & -\sin(\omega h_2 t) & \cos(\omega h_2 t) & 0 & 0 & \cdots \\ \hdashline 0 & 0 & 0 & 0 & \cos(\omega h_3 t) & \sin(\omega h_3 t) & \cdots \\ 0 & 0 & 0 & 0 & -\sin(\omega h_3 t) & \cos(\omega h_3 t) & \cdots \\ \hdashline \vdots & \vdots & \vdots & \vdots & \vdots & \vdots & \ddots \end{array}\right) \left(\begin{array}{c} y_{\alpha h_1}(t) \\ y_{\beta h_1}(t) \\ \hdashline y_{\alpha h_2}(t) \\ y_{\beta h_2}(t) \\ \hdashline y_{\alpha h_3}(t) \\ y_{\beta h_3}(t) \\ \hdashline \vdots \end{array}\right) \tag{2.24}$$

A Park's real transformation matrix $\mathbf{P}_{h_1..h_\nu}(\theta)$ can be usefully introduced. Its definition is given by either (2.25) or (2.26) depending on whether the

[2] see Werner formulas in Appendix C

number of phases n is even or odd, respectively.

$$\mathbf{P}_n(\theta) = \begin{pmatrix} \mathbf{P}_1(\theta) & \mathbf{0}_{2\times2} & \mathbf{0}_{2\times2} & \cdots & \mathbf{0}_{2\times2} \\ \mathbf{0}_{2\times2} & \mathbf{P}_2(\theta) & \mathbf{0}_{2\times2} & \cdots & \mathbf{0}_{2\times2} \\ \mathbf{0}_{2\times2} & \mathbf{0}_{2\times2} & \mathbf{P}_3(\theta) & \cdots & \mathbf{0}_{2\times2} \\ \vdots & \vdots & \vdots & \ddots & \vdots \\ \mathbf{0}_{2\times2} & \mathbf{0}_{2\times2} & \mathbf{0}_{2\times2} & \cdots & \mathbf{P}_\nu(\theta) \end{pmatrix} \tag{2.25}$$

$$\mathbf{P}_n(\theta) = \begin{pmatrix} \mathbf{P}_1(\theta) & \mathbf{0}_{2\times2} & \mathbf{0}_{2\times2} & \cdots & \mathbf{0}_{2\times2} & \mathbf{0}_{2\times1} \\ \mathbf{0}_{2\times2} & \mathbf{P}_2(\theta) & \mathbf{0}_{2\times2} & \cdots & \mathbf{0}_{2\times2} & \mathbf{0}_{2\times1} \\ \mathbf{0}_{2\times2} & \mathbf{0}_{2\times2} & \mathbf{P}_3(\theta) & \cdots & \mathbf{0}_{2\times2} & \mathbf{0}_{2\times1} \\ \vdots & \vdots & \vdots & \ddots & \vdots & \vdots \\ \mathbf{0}_{2\times2} & \mathbf{0}_{2\times2} & \mathbf{0}_{2\times2} & \cdots & \mathbf{P}_\nu(\theta) & \mathbf{0}_{2\times1} \\ \mathbf{0}_{1\times2} & \mathbf{0}_{1\times2} & \mathbf{0}_{1\times2} & \cdots & \mathbf{0}_{1\times2} & 1 \end{pmatrix} \tag{2.26}$$

In (2.25)-(2.26), the symbol $\mathbf{0}_{p\times q}$ indicates a $p \times q$ null matrix and

$$\mathbf{P}_h(\theta) = \begin{pmatrix} \cos(h\theta) & \sin(h\theta) \\ -\sin(h\theta) & \cos(h\theta) \end{pmatrix} \tag{2.27}$$

Combining (2.10) and (2.24) we can synthetically write:

$$\mathbf{y}_{dq}(t) = \mathbf{P}_n(\omega t)\mathbf{Q}_{h_1,..h_\nu}\mathbf{y}_{std}(t) \tag{2.28}$$

In conclusion, the decoupling transformation which performs the VSD into rotating reference frames in presence of ν time harmonics of orders $h_1..h_\nu$ is:

$$\mathbf{T}_{d(h_1..h_\nu)}(\theta) = \mathbf{P}_n(\theta)\mathbf{Q}_{h_1..h_\nu}; \tag{2.29}$$

It is worth noticing that Park's matrix, defined as per (2.25)-(2.26), is orthonormal, as can be easily proved observing that $\mathbf{P}_h(\theta)\mathbf{P}_h^T(\theta) = \mathbf{I}_{2\times2}$ for any h ($\mathbf{I}_{2\times2}$ being the 2×2 identity matrix) and thereby observing that $\mathbf{P}_n(\theta)\mathbf{P}_n^T(\theta) = \mathbf{I}$. This guarantees that $\mathbf{T}_{d(h_1..h_\nu)}(\theta)$ defined as per (2.29), is orthonormal, too, being the product of orthonormal matrices.

2.4.3 Selection of the harmonic orders for VSD

In general, phase variables may contain more than ν time harmonics, but in an n-phase winding the VSD process can work with a maximum number of harmonics equal to ν defined in (2.14). The selection of the ν time harmonics to be processed by VSD should obviously consider their amplitude (harmonics of smaller amplitude could be neglected without remarkable loss of accuracy) and also the condition expressed by (2.17). In case of multi-three-phase machines with winding arrangement like in Fig. 2.5a, both in case of even or odd n number of phases, the q-set of time harmonic orders to be processed which can be used for building matrix $\mathbf{Q}_{h_1,..h_\nu}$ is the following:

$$\begin{aligned} q &= 1, 3, 5, 7, .., 2\nu + 1 \text{ if } n \text{ is odd} \\ q &= 1, 3, 5, 7, .., 2\nu - 1 \text{ if } n \text{ is even} \end{aligned} \tag{2.30}$$

Its relative theorem and formal proof can be found in [49]. Since out of the scope of this thesis, the q-set of time harmonic orders to be considered for winding arrangements with $m \neq 3$ phases per set of windings is not reported but it can be found in [54, 55].

2.5 Conclusions

Diagonalisation of the inductance matrix for finding the harmonic inductances can be obtained analytically thanks to the vector space decomposition. The equivalent decoupled (hence diagonal) $\mathbf{L}_{vsd}$ matrix in the following equation is the so called harmonic inductance matrix:

$$\mathbf{L}_{vsd} = \mathbf{T}_{vsd}\mathbf{L}_{abc}\mathbf{T}_{vsd}^{T} \tag{2.31}$$

where $\mathbf{T}_{vsd}$ is the final real-valued orthonormal decoupling transformation matrix ($\mathbf{T}_{vsd}^{-1} = \mathbf{T}_{vsd}^{T}$) obtained cascading the decoupling transformation matrix $\mathbf{T}_d$ and the geometrical transformation matrix $\mathbf{W}$:

$$\mathbf{T}_{vsd}(\theta) = \mathbf{T}_d(\theta)\mathbf{W} \tag{2.32}$$

After building the de-coupling transformation matrix and applying it to $\mathbf{L}_{abc}$ like in (2.33), the $\mathbf{L}_{vsd}$ de-coupled harmonic inductance $n \times n$ matrix presents the following form:

$$\mathbf{L}_{vsd} = \begin{pmatrix} d_1 & 0 & 0 & 0 & \cdots & 0 & 0 & 0 \\ 0 & q_1 & 0 & 0 & \cdots & 0 & 0 & 0 \\ 0 & 0 & d_3 & 0 & \cdots & 0 & 0 & 0 \\ 0 & 0 & 0 & q_3 & \cdots & 0 & 0 & 0 \\ \vdots & \vdots & \vdots & \vdots & \ddots & 0 & 0 & 0 \\ 0 & 0 & 0 & 0 & 0 & q_{2\nu-1} & 0 & 0 \\ 0 & 0 & 0 & 0 & 0 & 0 & d_{2\nu+1} & 0 \\ 0 & 0 & 0 & 0 & 0 & 0 & 0 & q_{2\nu+1} \end{pmatrix} = \mathbf{T}_{vsd}\mathbf{L}_{abc}\mathbf{T}_{vsd}^{T} \tag{2.33}$$

where subscripts denote harmonic orders, and d or q denotes the axis of the rotor-attached orthogonal $dq0$. In case of odd number of phases, the last row and the last column do not appear. In case of even number of phases the last two rows and the last two columns do not appear. Values in (2.33) are the inductances the stator exhibits in nominal condition when subjected to a symmetrical supply voltage system. In Appendices A and B numerical examples for even and odd n are provided, respectively.

In the next chapter, values d_1 and q_1 will be used together with stator resistance value r_s for tuning the proportional-integral current controllers in Fig. 2.6. Furthermore, equivalence between $dq0$ and vsd models under balanced supply hypothesis will be provided. In Chapter 4, speed PI controllers will be designed considering the equivalent first order low pass filter transfer functions with cut-off frequencies ω_{cd} and ω_c shown in Fig. 2.6.

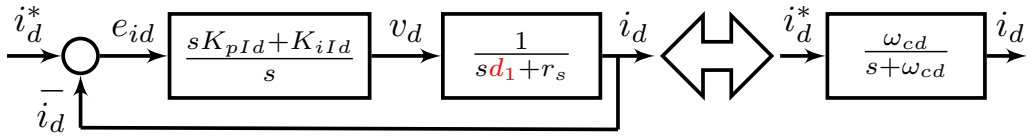

(a) d axis

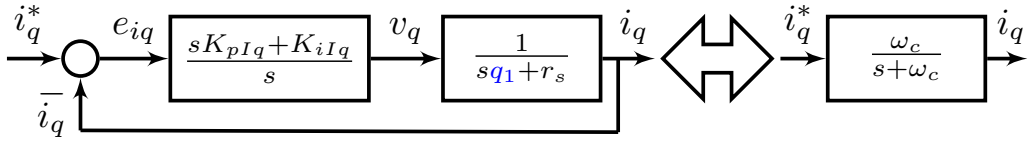

(b) q axis

Figure 2.6: Current control diagrams within the synchronous reference frame and their relative equivalent transfer functions. There is no axes decoupling. d_1 and q_1 are the first harmonic inductances, and r_s is the phase resistance. K_{pId}, K_{iId}, K_{pIq}, and K_{iIq} are the dq proportional integral current control gains, respectively.

Chapter 3

Distributed Current Control

In this thesis, distributed current control is done within the $dq0$ reference frame. Unfortunately the Park's transformation does not de-couple every output current to its relative input voltage. For this reason, the first harmonic inductances along the d and q axes exhibited by the stator under balanced voltage supply must be computed, through either numerical or analytical solution like discussed in Chapter 2. In Appendices A and B full diagonalisation with equations from Chapter 2 is provided.

Here, proportional-integral current controllers of a quadruple synchronous generator without saliency [65] are tuned on the first harmonic inductances from (2.33), d_1 and q_1. After de-coupling the inductance matrix and setting-up the current PI controllers on stator resistance r_s, d_1, and q_1 values, Matlab/Simulink current reference steps within the $dq0$ reference frame are compared against the current reference step within the orthonormal vsd space.

3.1 Introduction

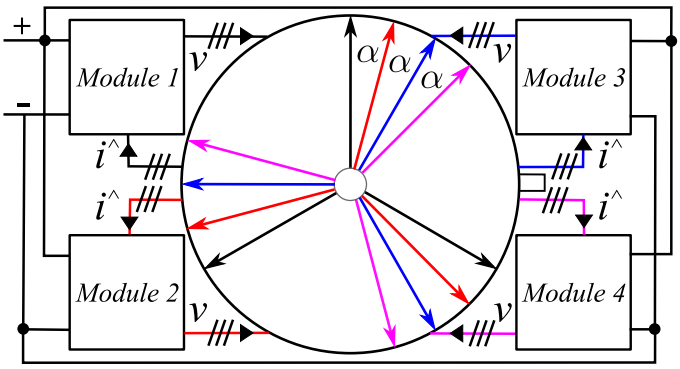

Figure 3.1: Quadruple multi-three-phase machine with paralleled distributed converters.

In Table 3.1, the stator leakage inductances M, H, and X in $p.u.$ of the quadruple-star synchronous motor under investigation in Fig. 3.1 are reported. L_{md} and L_{mq} are given in Appendix A together with a full numerical example better explaining Sections 3.2 and 3.3. Due to the fact that

Table 3.1: Stator leakage inductances in $dq0$ in $p.u.$

i-j	0-0	0-1	0-2	0-3
$M[p.u.]$	0.1	0.02	0.01	0.02
$H[p.u.]$	0.1	0.02	0	0.02
$X[p.u.]$	0	0	0	0

$X_{0-1} = 0$, there are no d-q interactions between different sets of windings. Values in Table 3.1 have been obtained with Finite Element Analysis (FEA) and they are referred to the rotor-attached $dq0$ reference frame. Since the vsd transformation matrix is meant to be applied to any multi-phase winding topology, the $\mathbf{L}_{vsd}$ matrix in (2.33) can be computed after anti-transforming

$\mathbf{L}_{dq0}$ into $\mathbf{L}_{abc}$ like in the following equation:

$$\mathbf{L}_{abc} = \mathbf{T}_{Park}^{T} \mathbf{L}_{dq0} \mathbf{T}_{Park} \tag{3.1}$$

and then applying $\mathbf{T}_{vsd} = \mathbf{T}_d(\theta)\mathbf{W}$ to $\mathbf{L}_{abc}$ in (3.1) like in (2.31). It is worth to recall that for every multi-phase winding topology there is a particular geometrical transformation matrix $\mathbf{W}$ mapping the practical winding arrangement into a n-phase equivalent scheme like explained in sub-section 2.4.1. In Fig. 3.2, a flow chart summarising the whole procedure is shown.

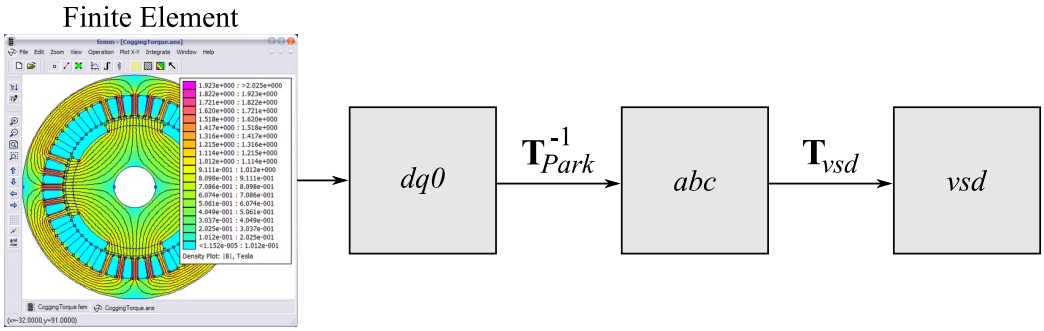

Figure 3.2: Finite element output is within the $dq0$ reference frame. In order to apply the $\mathbf{T}_{vsd}$ matrix, finite element output must be anti-transformed.

In the next section, for simplicity's sake, whenever the current dynamic is the same in all the modules, only data regarding the first module will be plotted. Furthermore, since in this particular case $L_{md} = L_{mq}$, only data regarding the q axis of the first module will be shown.

3.2 dq0 state space model

Speed regulation is obtained controlling the current flowing within the motor by an inner and faster current loop [66]. Since much faster than the rotor dynamic, the $dq0$ current control loop design based on the voltage stator equation (2.3) has been computed in blocked rotor condition. Therefore, the

speed (ω) is zero, and (2.3) becomes:

$$\mathbf{v}_{dq} = \mathbf{R}_{dq}\mathbf{i}_{dq} + \mathbf{L}_{dq}\frac{d\mathbf{i}_{dq}}{dt} \tag{3.2}$$

($\mathbf{L}_{dq}$ is given in A.2). In state space model form, (3.2) becomes:

$$\begin{aligned} \dot{\mathbf{x}}_{dq} &= \mathbf{A}_{dq}\mathbf{x}_{dq} + \mathbf{B}_{dq}\mathbf{u}_{dq} \\ \mathbf{y}_{dq} &= \mathbf{C}\mathbf{x}_{dq} + \mathbf{D}\mathbf{u}_{dq} \end{aligned} \tag{3.3}$$

where $\mathbf{x}_{dq}$ is the current state vector, $\mathbf{u}_{dq}$ is the applied voltage input vector, $\mathbf{y}_{dq}$ is the output current vector, $\mathbf{A}_{dq} = -\mathbf{L}_{dq}^{-1}\mathbf{R}_{dq}$, $\mathbf{B}_{dq} = \mathbf{L}_{dq}^{-1}$, $\mathbf{C}$ and $\mathbf{D}$ are respectively identity and null matrices $n \times n$. For clarity, the current vector $\mathbf{i}_{abc}$ and the state space variable vector $\mathbf{x}_{dq}$ corresponding to the current vector $\mathbf{i}_{dq}$ are reported in the equation below.

$$\mathbf{i}_{abc} = \begin{bmatrix} i_1 \\ i_2 \\ i_3 \\ \vdots \\ i_{10} \\ i_{11} \\ i_{12} \end{bmatrix}; \quad \mathbf{u}_{dq} = \begin{bmatrix} v_{d1} \\ v_{q1} \\ v_{01} \\ \vdots \\ v_{d4} \\ v_{q4} \\ v_{04} \end{bmatrix}; \quad \mathbf{x}_{dq} = \mathbf{i}_{dq} = \begin{bmatrix} x_1 \\ x_2 \\ x_3 \\ \vdots \\ x_{10} \\ x_{11} \\ x_{12} \end{bmatrix} = \begin{bmatrix} i_{d1} \\ i_{q1} \\ i_{01} \\ \vdots \\ i_{d4} \\ i_{q4} \\ i_{04} \end{bmatrix} \tag{3.4}$$

Looking at vectors in (3.4), the four i_q currents are mapped into state space variables x_2, x_5, x_8, and x_{11}. In a more compact form with $h = 1..N$, every i_{qh} current is mapped into its relative x_{3h-1} state space variable.

Since $\mathbf{L}_{dq}$ is not diagonal, it is not possible to get the decoupled transfer functions between the *i-th* input and *j-th* output with the following equation:

$$\mathbf{G}_{dq} = \mathbf{C}(s\mathbf{I} - \mathbf{A}_{dq})^{-1}\mathbf{B}_{dq} + \mathbf{D} = \mathbf{y}_{dq}/\mathbf{u}_{dq} \tag{3.5}$$

where $\mathbf{I}$ is identity matrix and s is the Laplace operator. Indeed $\mathbf{G}_{dq}$ is not diagonal [12]. In order to find the value of the first harmonic inductor needed for designing the current controller in nominal condition, the inductance matrix can be diagonalized either numerically or analytically thanks to the Vector Space Decomposition (VSD) like discussed in the previous chapter.

3.3 VSD state space model

Within the *vsd* orthonormal space, the new input $\mathbf{u}_{vsd}$, output $\mathbf{y}_{vsd}$ and state space vectors $\mathbf{x}_{vsd}$ in (3.6), are the odd harmonic values of applied voltages, output currents and state space values up to the $2\nu \pm 1$-th[3] harmonic on both d and q axes, respectively ($\mathbf{C} = \mathbf{I}$ and $\mathbf{D} = \mathbf{0}$, therefore $\mathbf{y}_{vsd} = \mathbf{x}_{vsd}$).

$$\mathbf{u}_{vsd} = \begin{bmatrix} u_{d1} \\ u_{q1} \\ \hdashline u_{d3} \\ u_{q3} \\ \hdashline \vdots \\ \hdashline u_{d(2\nu\pm1)} \\ u_{q(2\nu\pm1)} \end{bmatrix} \quad \mathbf{y}_{vsd} = \begin{bmatrix} y_{d1} \\ y_{q1} \\ \hdashline y_{d3} \\ y_{q3} \\ \hdashline \vdots \\ \hdashline y_{d(2\nu\pm1)} \\ y_{q(2\nu\pm1)} \end{bmatrix} \quad \mathbf{x}_{vsd} = \begin{bmatrix} x_{d1} \\ x_{q1} \\ \hdashline x_{d3} \\ x_{q3} \\ \hdashline \vdots \\ \hdashline x_{d(2\nu\pm1)} \\ x_{q(2\nu\pm1)} \end{bmatrix} \tag{3.6}$$

Therefore, defining the new state space matrices $\mathbf{A}_{vsd} = -\mathbf{L}_{vsd}^{-1}\mathbf{R}_{vsd}$ and $\mathbf{B}_{vsd} = \mathbf{L}_{vsd}^{-1}$, the decoupled transfer functions have been computed in the *vsd* space thanks to the following equation:

$$\mathbf{G}_{vsd} = \mathbf{C}(s\mathbf{I} - \mathbf{A}_{vsd})^{-1}\mathbf{B}_{vsd} + \mathbf{D} = \mathbf{y}_{vsd}/\mathbf{u}_{vsd} \tag{3.7}$$

(where $\mathbf{L}_{vsd}$ is given in A.12). Since both $\mathbf{L}_{vsd}$ and $\mathbf{R}_{vsd}$ are diagonal ($\mathbf{R}_{vsd} = \mathbf{R}_{abc} = \mathbf{R}_{dq}$), the matrix $\mathbf{G}_{vsd}$ describing the odd harmonic current values up to the $2\nu \pm 1$-th harmonic, on both d and q axes, is diagonal too.

The $\mathbf{G}_{vsd}$ and $\mathbf{G}_{dq}$ transfer function matrices link inputs and outputs of two equivalent orthonormal spaces, and in the next section, their equivalence will be presented.

3.3.1 dq0-VSD state space model equivalence

In nominal condition under balanced supply voltages, transfer function matrix $\mathbf{G}_{vsd} = \mathbf{y}_{vsd}/\mathbf{u}_{vsd}$ in (3.7) is diagonal and it presents the following pattern

[3]Like explained in Chapter 2, up to $(2\nu - 1)$ if n is even, and up to $(2\nu + 1)$ if n is odd

($d_{1,3,..}$ and $q_{1,3,..}$ are given in A.12):

$$\mathbf{G}_{vsd} = \begin{pmatrix} \frac{1}{sd_1+r_s} & 0 & 0 & 0 & \cdots & 0 & 0 \\ 0 & \frac{1}{sq_1+r_s} & 0 & 0 & \cdots & 0 & 0 \\ 0 & 0 & \frac{1}{sd_3+r_s} & 0 & \cdots & 0 & 0 \\ 0 & 0 & 0 & \frac{1}{sq_3+r_s} & \cdots & 0 & 0 \\ \vdots & \vdots & \vdots & \vdots & \ddots & 0 & 0 \\ 0 & 0 & 0 & 0 & 0 & \frac{1}{sd_{2\nu\pm1}+r_s} & 0 \\ 0 & 0 & 0 & 0 & 0 & 0 & \frac{1}{sq_{2\nu\pm1}+r_s} \end{pmatrix} \tag{3.8}$$

On the other hand, $\mathbf{G}_{dq} = \mathbf{y}_{dq}/\mathbf{u}_{dq}$ in (3.5) is not diagonal, and in this particular case, it presents the following pattern:

$$\mathbf{G}_{dq} = \begin{pmatrix} \Upsilon & 0 & 0 & \Upsilon & 0 & 0 & \Upsilon & 0 & 0 & \Upsilon & 0 & 0 \\ 0 & \Upsilon_{(2,2)} & 0 & 0 & \Upsilon & 0 & 0 & \Upsilon & 0 & 0 & \Upsilon & 0 \\ 0 & 0 & \Upsilon & 0 & 0 & \Upsilon & 0 & 0 & \Upsilon & 0 & 0 & \Upsilon \\ \Upsilon & 0 & 0 & \Upsilon & 0 & 0 & \Upsilon & 0 & 0 & \Upsilon & 0 & 0 \\ 0 & \Upsilon_{(5,2)} & 0 & 0 & \Upsilon & 0 & 0 & \Upsilon & 0 & 0 & \Upsilon & 0 \\ 0 & 0 & \Upsilon & 0 & 0 & \Upsilon & 0 & 0 & \Upsilon & 0 & 0 & \Upsilon \\ \Upsilon & 0 & 0 & \Upsilon & 0 & 0 & \Upsilon & 0 & 0 & \Upsilon & 0 & 0 \\ 0 & \Upsilon_{(8,2)} & 0 & 0 & \Upsilon & 0 & 0 & \Upsilon & 0 & 0 & \Upsilon & 0 \\ 0 & 0 & \Upsilon & 0 & 0 & \Upsilon & 0 & 0 & \Upsilon & 0 & 0 & \Upsilon \\ \Upsilon & 0 & 0 & \Upsilon & 0 & 0 & \Upsilon & 0 & 0 & \Upsilon & 0 & 0 \\ 0 & \Upsilon_{(11,2)} & 0 & 0 & \Upsilon & 0 & 0 & \Upsilon & 0 & 0 & \Upsilon & 0 \\ 0 & 0 & \Upsilon & 0 & 0 & \Upsilon & 0 & 0 & \Upsilon & 0 & 0 & \Upsilon \end{pmatrix} \tag{3.9}$$

where $\Upsilon_{(i,j)}$ is the transfer function linking the i^{th} input voltage to the j^{th} output current computed with (3.5). In other words, under balanced supply voltages (i.e.: $v_{d1} = v_{d2} = v_{d3} = v_{d4}$, $v_{q1} = v_{q2} = v_{q3} = v_{q4}$, and $v_{01} = v_{02} = v_{03} = v_{04}$), the i_q current of the first set is function of all the input voltages like in the following equation:

$$\begin{aligned} i_{q1} = 0v_{d1} + \Upsilon_{(2,2)}v_{q1} + 0v_{01} + 0v_{d2} + \Upsilon_{(5,2)}v_{q2} + 0v_{02} + \\ +0v_{d3} + \Upsilon_{(8,2)}v_{q3} + 0v_{03} + 0v_{d4} + \Upsilon_{(11,2)}v_{q4} + 0v_{04} \end{aligned} \tag{3.10}$$

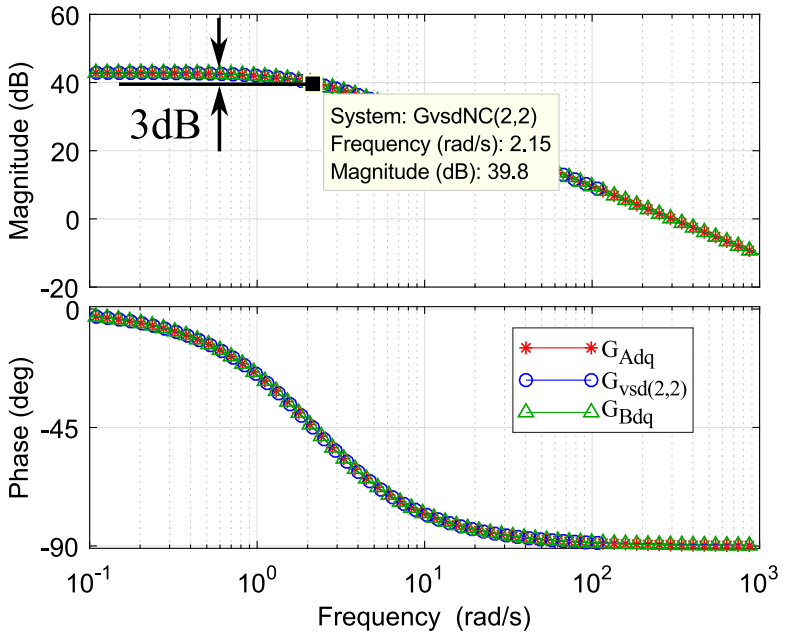

Figure 3.3: Bode diagram showing the equivalence between the two orthonormal spaces and the absence of interactions among different axes of different sets of windings. $\omega_c = 2.15[rad/s]$

In Fig.3.3, assuming balanced supply voltages, the equivalence of transfer function G_{Adq} defined as:

$$G_{Adq} = \sum_{k=1}^{n} G_{dq(k,2)} = \\ = 0 + \Upsilon_{(2,2)} + 0 + 0 + \Upsilon_{(5,2)} + 0 + 0 + \Upsilon_{(8,2)} + 0 + 0 + \Upsilon_{(11,2)} + 0 \tag{3.11}$$

and $G_{vsd(2,2)}$ in (3.8) is shown. G_{Adq} (in red asterisks) relates all the $dq0$ inputs with the q output current of the first set of windings $x_{dq(2,1)}$ in (3.4). $G_{vsd(2,2)}$ (in blue circles) relates the first harmonic q input voltage with the first harmonic q output current, x_{q1} in (3.6). In order to highlight that the mutual leakage inductance X_{0-1} in Fig. 2.3 is zero, in green triangles it is shown the transfer function

$$G_{Bdq} = \sum_{k=1}^{N} G_{dq(3k-1,2)} = \Upsilon_{(2,2)} + \Upsilon_{(5,2)} + \Upsilon_{(8,2)} + \Upsilon_{(11,2)} \tag{3.12}$$

describing just the q output current of the first set of windings taking into account only the q input voltages ($u_{dq(2,1)}$,$u_{dq(5,1)}$,$u_{dq(8,1)}$,$u_{dq(11,1)}$). This can be further verified looking at the elements in red in matrix $\mathbf{G}_{dq}$ in (3.9). The match between G_{Adq} and G_{Bdq} confirms that there are no interactions among different axes of different sets of windings.

The electrical dominant pole of the motor supplied by a symmetrical supply voltage system is given by the following equation:

$$\begin{aligned} \omega_c &= r_s/q_1 \\ \omega_{cd} &= r_s/d_1 \end{aligned} \tag{3.13}$$

where r_s is the phase resistance and q_1 is the first harmonic inductance of the q axis in nominal condition, and it coincides with the $G_{vsd(2,2)}$ transfer function pulsation shown in Fig.3.3. The pulsation in nominal condition ω_c can be either computed with (3.13) or graphically extrapolated from the cut-off frequency transfer function G_{Adq} highlighted in Fig.3.3. Since r_s can be easily measured, once ω_c is extrapolated from the bode plot, q_1 computation is trivial. Exactly the same considerations are valid for the d axis.

3.4 Regulators design

Once d_1 and q_1 are computed or graphically extrapolated from the Bode plot of their relative plants (depending on what is provided), both d and q current PI controllers described by the following equation can be computed:

$$PI_\Lambda = \frac{sK_{pI\Lambda} + K_{iI\Lambda}}{s} = C_\Lambda \tag{3.14}$$

In the above equation, Λ represents d or q axis and s is the Laplacian operator. The current PIs are tuned considering the plant G_Λ in (3.15):

$$G_\Lambda = \frac{1}{s\Lambda_1 + r_s} \tag{3.15}$$

A simplified control diagram not considering actuation nor filtering delays is shown in Fig. 3.4. Omitting Λ for simplicity, defining a_n,b_n,a_d,b_d the real

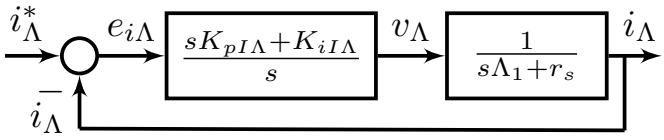

Figure 3.4: Current control diagram within the synchronous reference frame without axes decoupling with first harmonic inductance Λ_1 (Λ identifies d or q axis) and the phase resistance r_s. $K_{pI\Lambda}$ and $K_{iI\Lambda}$ are the PI gains.

and the imaginary part of the numerator and the denominator of the plant to be controlled, and defining:

$$Q_{ph} = \tan\left[\varphi_c - \frac{\pi}{2} - \arctan\left(\frac{b_n}{a_n}\right) + \arctan\left(\frac{b_d}{a_d}\right)\right] \tag{3.16}$$

$$Q_{magN} = a_n^2 + b_n^2 \tag{3.17}$$

$$Q_{magD} = a_d^2 + b_d^2 \tag{3.18}$$

for any cross-over bandwidth (ω_c) and phase margin (φ_c) design input parameter, the proportional and the integral gains can be calculated imposing the following conditions:

$$\begin{cases} \angle G_{OL}(j\omega_c) = \varphi_c - \pi \\ |G_{OL}(j\omega_c)| = 1 \end{cases} \tag{3.19}$$

where $G_{OL} = C_\Lambda G_\Lambda$ is the open loop transfer function. The resolution of the above system composed by two equations respect the integral and the proportional gain leads to (Λ has been omitted for simplicity):

$$K_{pI} = \sqrt{\frac{Q_{magD}}{Q_{magN}} \frac{Q_{ph}^2}{(Q_{ph}^2+1)}} \tag{3.20}$$

$$K_{iI} = \sqrt{\frac{Q_{magD}}{Q_{magN}} \frac{\omega_c^2}{(Q_{ph}^2+1)}} \tag{3.21}$$

Once the PI controllers in Fig. 3.4 are tuned with (3.20) and (3.21) for both the dq axes, when designing the speed control loop, the current loop

dynamic can be modelled like a low-pass filter with bandwidth $\omega_{c\Lambda}$ and phase margin $\varphi_{c\Lambda}$ described by the following transfer function:

$$G_{I\Lambda} = \frac{i_\Lambda}{i_\Lambda^*} = \frac{\omega_{c\Lambda}}{s + \omega_{c\Lambda}} = \frac{C_\Lambda G_\Lambda}{1 + C_\Lambda G_\Lambda} \tag{3.22}$$

3.5 Simulation results

Considering the motor in Fig. 3.1, distributed current control based on the previous discussions is here validated by means of comparison between output *vsd* currents from diagrams in Fig. 3.5 and output $dq0$ currents from a Matlab/Simulink model based on the $dq0$ state space model in (3.2). Since in this particular case $L_{md} = L_{mq}$, only results regarding the q axis will be shown.

The q currents $i_{q1}, i_{q2}, i_{q3}, i_{q4}$ of the four sets of windings are respectively the 2-nd, 5-th, 8-th and 11-th element of the state space vector $\mathbf{x}_{dq}$ in (3.4). The stator leakage inductances in *p.u.* are reported in Table 3.1, the magnetizing inductances and stator phase resistor are respectively $L_{mq} = L_{md} = 1.62 p.u.$ and $r_s = 0.0072\Omega$ and they were computed by the machine designer using FE software. In nominal condition, the resulting first harmonic inductance q_1 has been computed by (2.33) equal to $0.0033H$ and further verified thanks to (3.13) together with Fig. 3.3 ($q_1 = r_s/\omega_c$). In Appendix A, the full numerical example is given. Every current PI controller has been set up with current bandwidth $\omega_c = 600[rad/s]$ and phase margin $\varphi_c = 60°$. Second order current filter and microprocessor actuation delays ($e^{-s1.5T_s}$) have been introduced as shown by control diagram in Fig. 3.5. The delay has been set as $T_s = 2\pi/(25\omega_c)[s]$ and the current filter cut-off frequency as $\omega_f = 66 \cdot 10^3[rad/s]$. Taking into account actuation and acquisition delays, the new open loop transfer function becomes:

$$G_{OL\Lambda} = C_\Lambda \frac{1}{s1.5T_s + 1} G_\Lambda \frac{\omega_f^2}{s^2 + \sqrt{2}\omega_f s + \omega_f^2} \tag{3.23}$$

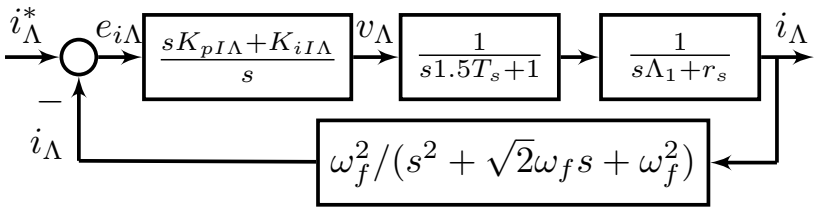

Figure 3.5: Actuation delay and current filter have been introduced in order to highlight stability margin variations while keeping constant the PI gains in faulty conditions.

PI parameters computation in nominal condition using algorithm in Sec. 3.4 has led to $K_{pIq} = K_{pId} = 2.12$ and $K_{iIq} = K_{iId} = 197$.

The output *vsd* current from control diagram in Fig.3.5 (labelled Desired dynamic) has been compared with the four output i_q currents (i_{q1}, i_{q2}, i_{q3}, i_{q4}) of a Simulink simulation with the four PI controllers regulating the whole $dq0$ machine model.

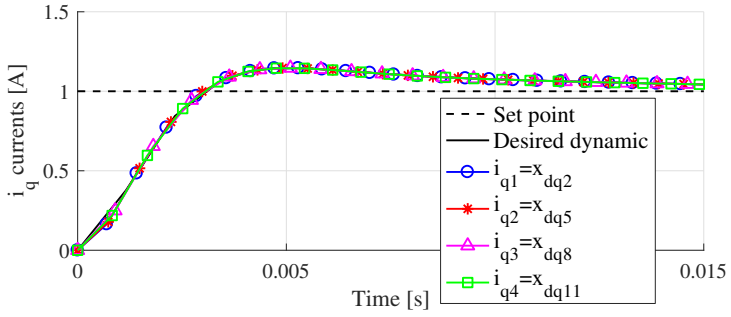

Figure 3.6: Current step in nominal condition. The "Desired dynamic" is the first harmonic *vsd* output current (i_Λ) from control diagram in Fig. 3.5.

In Fig. 3.6, it is possible to appreciate the match between the desired dynamic from the *vsd* control diagram in Fig.3.5 and the four Simulink output i_q currents with the same PI parameters.

In the next chapter, the speed control loop will be presented modelling the inner current loops as a low pass filter like in Eq. (3.22).

Chapter 4

Distributed Speed Control

The two main speed configurations for multi-drive systems previously introduced in Chapter 1 are the common speed reference (CSR) and the torque follower (TF), shown in Fig. 1.11a and 1.11b, respectively. As previously stated, due to skews and non-stiff couplings, in multi-drive systems speed and position of the shafts cannot be considered the same. Contrarily, since in multi-three-phase electrical motors the shaft is one, position information is the same among all the drives.

In this chapter, distributed speed control is introduced and speed PI regulator design for a synchronous multi-three-phase electrical machine with nine phases and with disconnected neutral points like the one in Fig. 4.1 is presented. The CSR (where all the drives are configured in speed mode) and the TF configuration (where one drive is in speed mode and all the others are in torque mode) are compared in order to highlight similarities and differences. In-fact, due to the shaft stiffness, under same conditions the two configurations presents the same speed dynamics. However, the TF is not fault tolerant in case of master fault. Contrarily, thanks to its distributed nature, the CSR is not compromised in case of module failure. Analytical equations and simulations by means of Matlab/Simulink models are provided. In Chapter 8, experimental results will be provided.

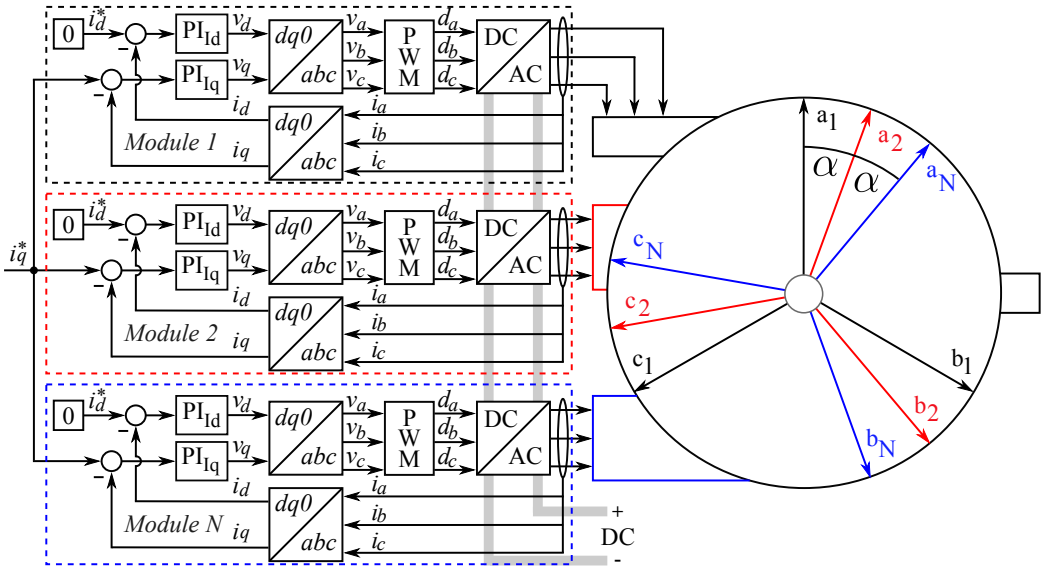

Figure 4.1: Distributed current control.

4.1 Equivalent current control diagram

Distributed speed control is achieved regulating the current with an inner control loop [66]. In the previous chapter, current control loop design has been introduced and discussed. Current control within a multi-three-phase motor can be achieved by connecting to every set of windings one power converter commanded by its relative drive configured in torque mode, Fig. 4.1. Like anticipated in Section 3.4, for both d and q axis, every current control loop is modelled as a low-pass filter with bandwidth ω_c and phase margin φ_c described by the following transfer function:

$$G_I = \frac{i}{i^*} = \frac{\omega_c}{s + \omega_c} \tag{4.1}$$

Defining the angular speed of the shaft ω, the machine constant K_t relating torque and i_q current, the inertia J and the friction F, the simplified control diagram of the machine configured in torque mode is shown in Fig. 4.2. T_L is the load torque. Provided that torque and i_q current are directly proportional ($T = K_t i_q$), at steady state the final speed of the shaft is set by the balance

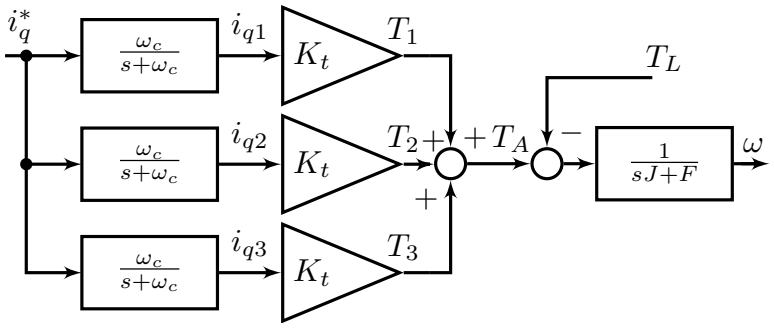

Figure 4.2: Torque mode simplified diagram. Every i_q current control loop has been replaced by a low pass filter with bandwidth ω_c.

between the load torque T_L and the torque T_A produced by the modules supplying the motor [66].

$$T_A = \sum_{j}^{N} T_j \tag{4.2}$$

The parallel of the three i_q current loops in Fig. 4.2 can be further simplified with control diagram in Fig. 4.3, in which at steady state $T_A = Ni_qK_t$.

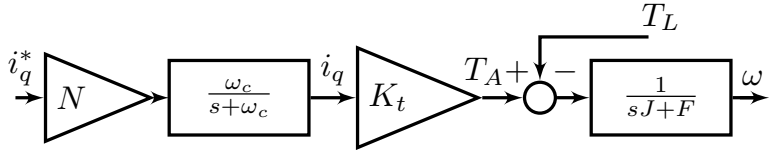

Figure 4.3: Equivalent torque mode simplified diagram.

4.2 Equivalent speed control diagram

In general, speed control is set by the outer speed loop governed by a speed PI regulator. Assuming all the modules produce torque, regulators in multi-three-phase applications can be computed considering the loop in Fig. 4.4, where the equivalent (EQ) closed speed loop is shown. Once the speed PI

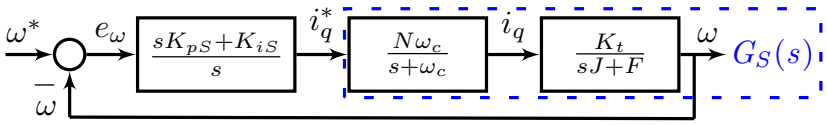

Figure 4.4: Equivalent (EQ) speed control diagram. K_{pS} and K_{iS} are the PI gains.

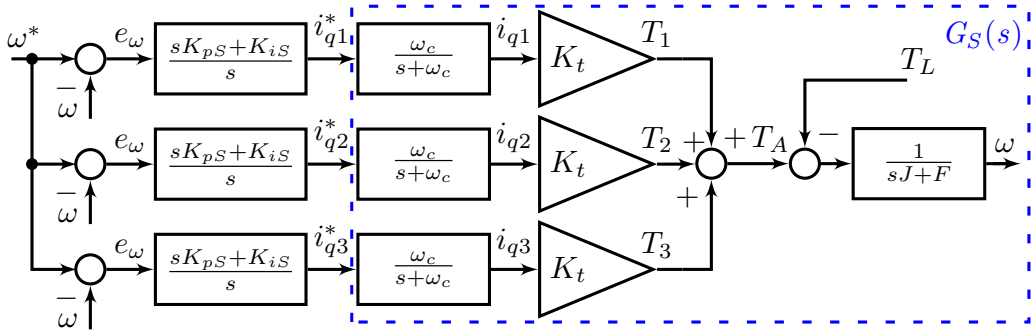

(a) Simplified common speed reference control diagram (CSR).

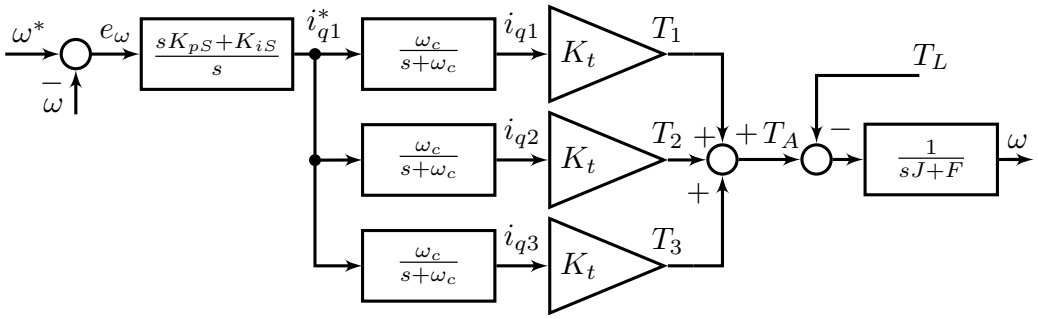

(b) Simplified torque follower control diagram (TF).

Figure 4.5: Common Speed Reference - Torque Follower control diagram comparison.

parameters have been computed on plant $G_S(s)$ defined as:

$$G_S(s) = N \frac{\omega_c}{s+\omega_c} K_t \frac{1}{sJ+F} \tag{4.3}$$

the same PI regulator values (K_{pS} and K_{iS}) can be used in the final simplified CSR control diagram in Fig. 4.5a, where there are three speed control loops in parallel.

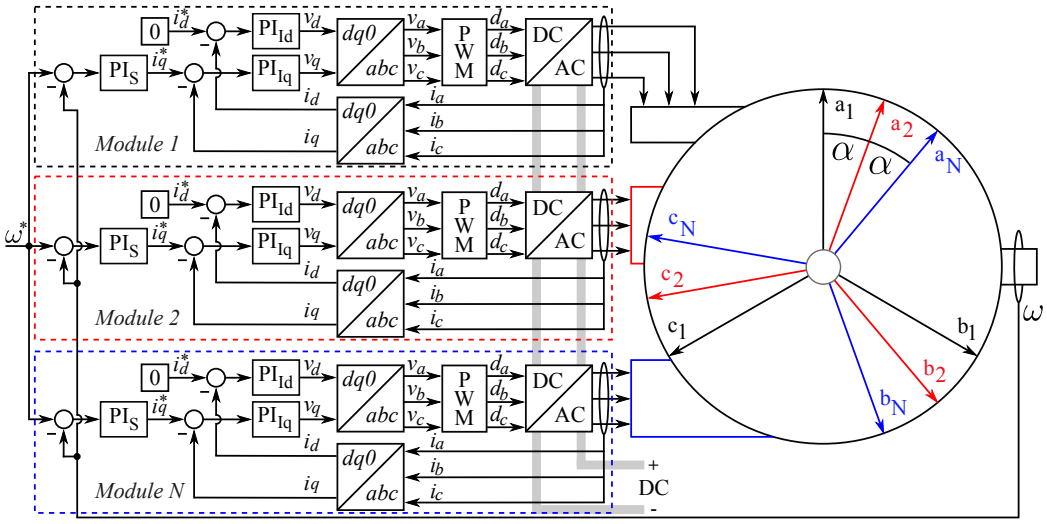

Figure 4.6: Distributed Speed control in CSR configuration.

4.3 CSR - TF comparison in faulty operation

In Fig. 4.5 the simplified Common Speed Reference and Torque Follower control diagrams are shown. In the TF configuration in Fig. 4.5b, only the master drive on top is configured in speed mode. All the slaves are configured in torque mode and inputs are provided with the internal i^*_{q1} current set-point from the master drive. Considering the previous discussion in section 1.4 regarding infinitely rigid couplings, the absence of skews since there is only one shaft, and assuming that all speed set-points ω^* and speed feedbacks ω in Figs. 4.5a and 4.5b are the same in every drive, the CSR and the TF simplified diagrams in Fig. 4.5 are equivalent. In Fig. 4.6, the CSR implementation is shown. For a given set-point $\omega^* = 30[rad/sec]$ in nominal condition where all the modules produce torque, the output speeds of the EQ, CSR, and TF configuration are all the same like it is highlighted in Fig. 4.7.

The difference between the CSR and the TF configuration is from the fault tolerance point of view. In-fact, if the master drive in Fig. 4.5b fails, the output speed is not regulated any more since the follower drives are

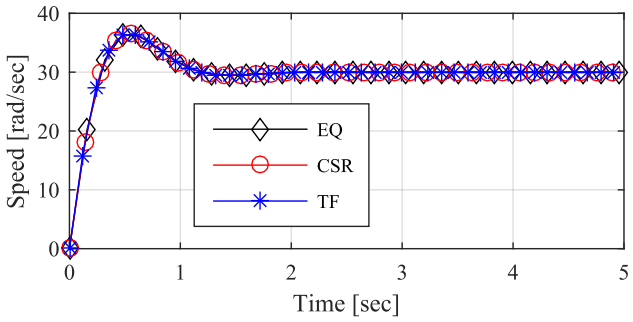

Figure 4.7: Equivalence between EQ (Fig. 4.4), CSR (Fig. 4.5a) and TF (Fig. 4.5b) control diagram output speeds with $\omega^* = 30[rad/sec]$ and $T_L = 0[Nm]$.

provided with the i_{q1} internal current set-point. In Fig. 4.8, CSR and TF output speeds in Fault Condition (FC) are compared against the CSR in Nominal Condition (NC). From now on, it is assumed that in case of a generic fault, the affected module is able to disconnect itself in open circuit condition and to notify the other modules. From Fig. 4.8, it can be seen

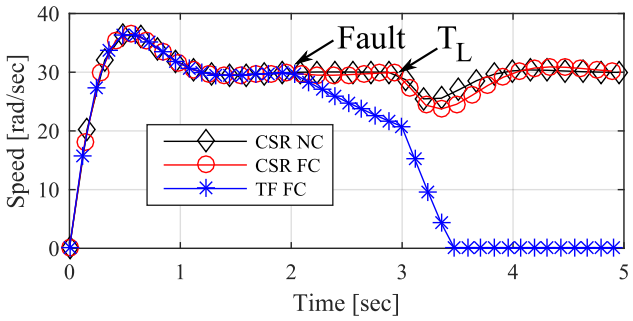

Figure 4.8: TF configuration is not fault tolerant in case of master fault. After 3 seconds the load is attached and the output speed is regulated. However, CSR speed dynamic in fault condition is degraded.

how the CSR is able to regulate the speed of the shaft. However, the speed dynamic is degraded if compared to the one in nominal condition. Post-fault compensation strategy keeping constant the speed bandwidth will be given in section 5.3. From this point, nominal and open circuit condition will be denoted respectively with subscript $_{NC}$ and $_{OC}$.

Chapter 5

Power Sharing

In section 1.3, some of the advantages introduced by multi-three-phase machines in a real case marine scenario have been discussed. In general, complexity increases both at system and machine-drive level. However, in some particular applications the benefits introduced by multi-three-phase motors with their relative tailored drives are worth the effort. Among the features enabled by multi-three-phase systems, like for example augmented reliability and fault tolerance at system level, power sharing is probably the most interesting one.

In this chapter, load sharing in multi-three-phase motors with disconnected neutral points is introduced and discussed by means of analytical equations and Matlab/Simulink simulations. In Chapter 8, the relative experimental results to this chapter will be used as benchmark when presenting the droop controller experimental work.

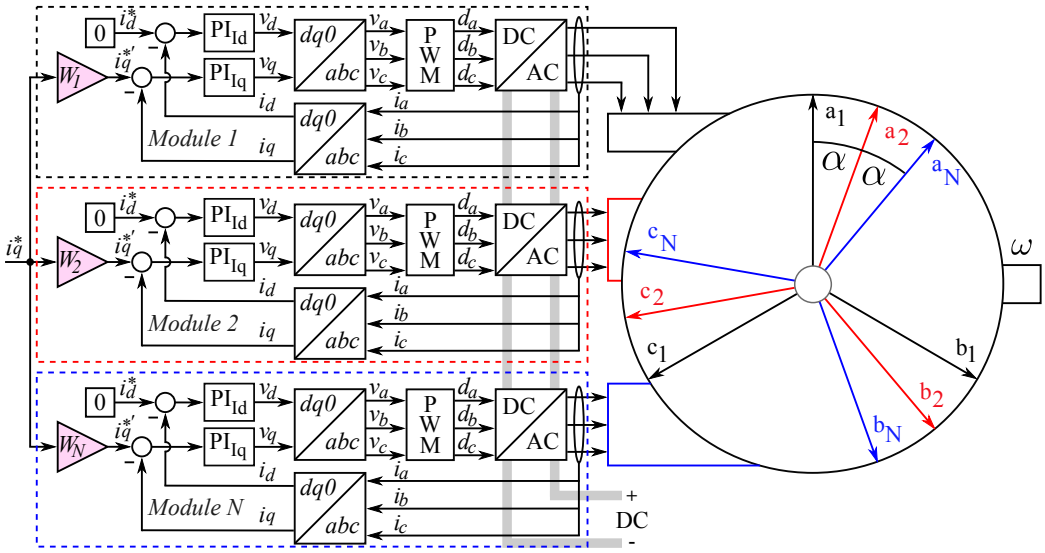

Figure 5.1: Distributed current control with power sharing capability.

Considering the distributed current control in Fig. 4.2 the total amount of torque T_A produced by all the modules could be set varying the i_q^* current set-points. Introducing a *sharing coefficient* (W_j with $j = 1..N$) per module like in Fig. 5.1, the current set-point, and therefore the torque produced by every single module, can be set. The *sharing coefficients* W_j define the new current set-points $i_{q1,2,3}^{*'}$ described by the following equation: $i_{qj}^{*'} = i_{qj}^* W_j$. In nominal condition, power is equally split (ES) and loop gains are assumed to be equal to one, $W_1 = W_2 = W_3 = 1$. Depending on the particular application, like previously discussed in Sec. 1.5, unbalanced sharing (US) can be obtained varying the *sharing coefficients*.

In Fig. 5.2, the simplified Torque Follower diagram with power sharing capabilities is shown. The total power P_{TOT} is given by the sum of all the nominal torques produced by each module multiplied by the shaft speed. Since currents and torques are directly proportional ($T_j = K_t i_{qj}$), the *j-th* power in *p.u.* is described by the following:

$$P_j = \frac{I_{q,j}}{\sum_j^N I_{q,j}} [p.u.] \tag{5.1}$$

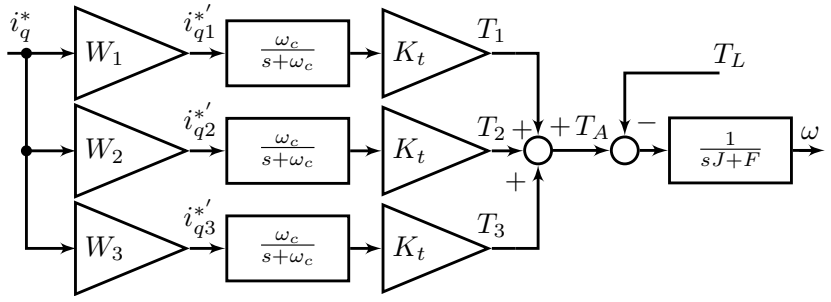

Figure 5.2: Torque follower simplified control schematic with *sharing coefficients* $W_{1,2,3}$.

where $I_{q,j}$ is the nominal current on the q-axis of the *j-th* module. Looking at Fig. 5.2, it can be seen that the new current set-points $i_{q1,2,3}^{*'}$ are defined by the *sharing coefficients* $W_{1,2,3}$, therefore the power P_j in *p.u.* produced by the *j-th* can be written as:

$$P_j = \frac{W_j}{\sum_j^N W_j} \tag{5.2}$$

Defining the *global sharing coefficient* W_T:

$$W_T = \sum_j^N W_j \tag{5.3}$$

equations (5.2) becomes:

$$P_j = \frac{W_j}{W_T} \tag{5.4}$$

Thanks to (5.4), as long as W_T is kept constant, unbalanced power sharing can be achieved just changing the *sharing coefficients*. Whenever unbalanced sharing (US) ratio is needed (not equal sharing (ES) like previously supposed), the *sharing coefficients* W_j could be updated by a supervisory controller or programmed off-line a priori using (5.4):

$$W_j^{(US)} = P_j^{(US)} W_T^{(US)} \tag{5.5}$$

Assuming W_T is kept constant and that in ES condition $W_j^{(ES)} = 1$, equations (5.3) and (5.4) become $W_T^{(ES)} = W_T^{(US)} = N$ and $P_j^{(ES)} = 1/N \neq P_j^{(US)} = W_j^{(US)}/W_T^{(US)}$, respectively.

5.1 CSR with power sharing capability - Control design procedure

Based on the previous discussion, a design procedure for a system with N modules is presented here. Firstly, current PIs are tuned with (3.19) and speed PI_S are calculated considering the equivalent control scheme (EQ) in Fig. 4.4. The same speed PI parameters can be put into control schematic in Fig. 5.3 where $W_{1,2,3}$ are initially set to one for equal sharing (ES) operation. Load sharing, or unbalanced sharing (US), can be further achieved with (5.3), (5.4), and (5.5) keeping constant the *global sharing coefficient* W_T.

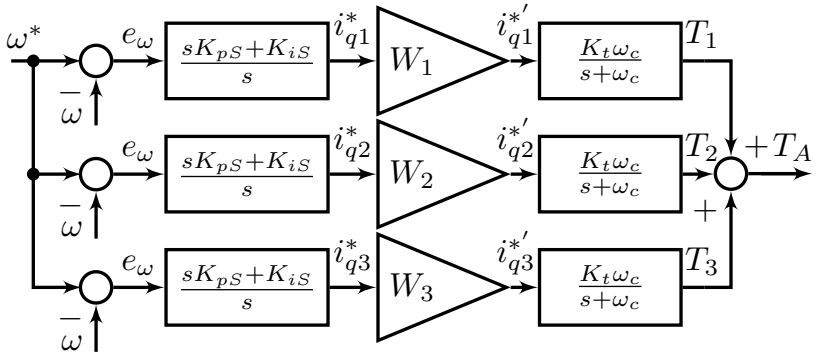

Figure 5.3: Common Speed Reference (CSR) simplified control schematic. $W_{1,2,3}$ are the sharing coefficients. The mechanical plant is not shown for simplicity.

5.2 Simulations

In this section, output speeds and output currents from control diagram in Fig. 5.3 with constant and variable *global sharing coefficient* W_T are shown. Aim of this section is at showing that without keeping constant W_T, the speed of the shaft is not constant during sharing step transients.

5.2.1 Constant global sharing coefficient

In Fig. 5.4, i_q currents in ES from simplified control schematic in Fig. 5.3 with $W_{1,2,3} = 1$ are shown. When connecting the load T_L after three seconds,

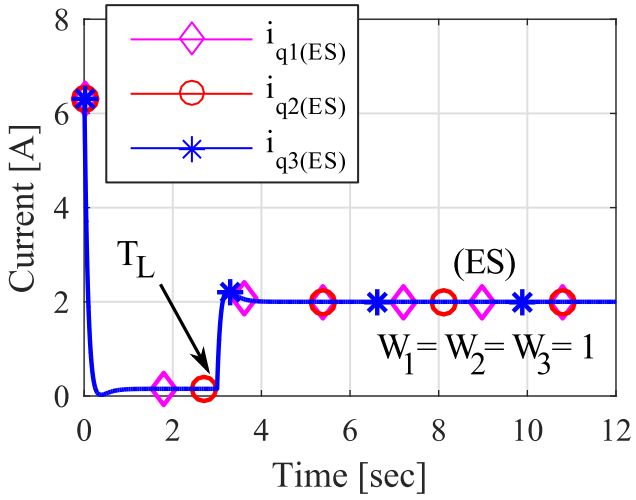

Figure 5.4: i_q currents under ES operation.

current of $2A$ per set of windings are flowing. According to (5.3) and (5.4), the power is equally split among the modules. Overall, $6A = N2A$ are flowing within the machine and $P_j^{(ES)} = W_j^{(ES)}/W_T^{(ES)} = 1/N = 1/3$.

In Fig. 5.5, speed dynamic equivalence between the control schematic in Fig. 4.4 - EQ - and the CSR simplified control schematic in Fig. 5.3 either in equal sharing operation - CSR(ES) - and unbalanced sharing operation - CSR(US) - is shown. In Fig. 5.6, the relative i_q currents from simulation in Fig. 5.5 are shown. Until second six, the power is equally split with $W_{1,2,3} = 1$. After six seconds, the load has been unbalanced with the following power ratios $P_1^{(US)} = 2/3$, $P_2^{(US)} = 1/12$, and $P_3^{(US)} = 1/4$. The relative *sharing coefficients* in US can be obtained from (5.5). At second nine, first and second power ratios have been swapped. In Table 5.1, sharing coefficients computed with (5.3) and (5.5) and their relative i_q current values are reported for both ES and US condition.

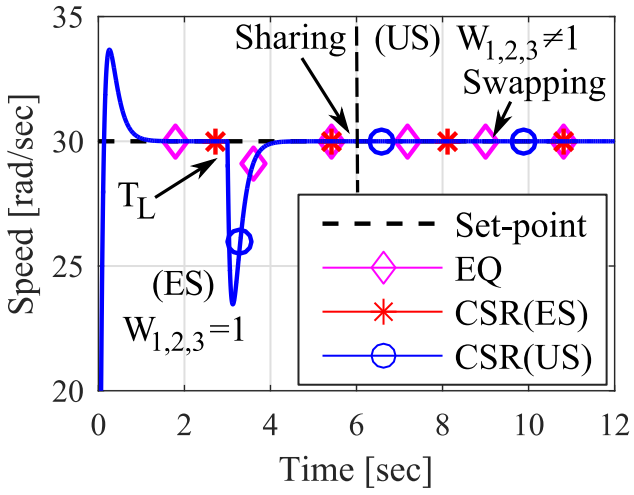

Figure 5.5: Keeping constant W_T guarantees constant speed during sharing transient.

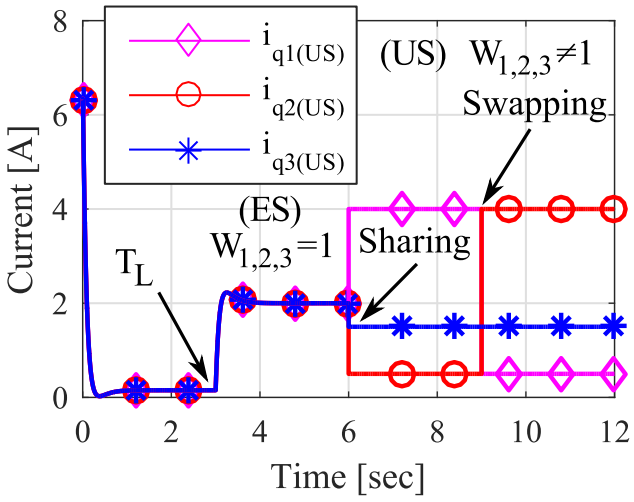

Figure 5.6: Load sharing (US operation).

Table 5.1: Sharing coefficients with constant W_T - (US) run

	$0 \div 6[sec]$			$6 \div 9[sec]$			$9 \div 12[sec]$		
j	$P^{(ES)}$	$W^{(ES)}$	$i_q^{(ES)}$	$P^{(US)}$	$W^{(US)}$	$i_q^{(US)}$	$P^{(US)}$	$W^{(US)}$	$i_q^{(US)}$
1	1/3	1	2	2/3	2	4	1/12	0.25	0.5
2	1/3	1	2	1/12	0.25	0.5	2/3	2	4
3	1/3	1	2	1/4	0.75	1.5	1/4	0.75	1.5
$\sum$	1	$N=3$	6	1	$N=3$	6	1	$N=3$	6

5.2.2 Variable global sharing coefficient

The last row in Table 5.1 highlights that $W_T = \sum_j^N W_j$ and $i_{qT} = \sum_j^N i_{qj}$ are constant before and after sharing and swapping operations guaranteeing constant speed as shown in Fig. 5.5. Power sharing without keeping constant the *global sharing coefficient* does not guarantee constant speed regulation as shown in Fig. 5.7.

The output speed from CSR control diagram in Fig. 5.3 with wrong *sharing coefficients* labelled CSR(WS) is compared against the previous simulation shown in Fig. 5.5 with constant W_T and labelled CSR(US). The relative i_q currents with wrong *sharing coefficients* ($i_{q1(WS)}$,$i_{q2(WS)}$,$i_{q3(WS)}$) are shown in Fig. 5.8 and compared against the ones from the run with constant W_T in Fig. 5.6 and plotted in dashed black lines ($i_{qj(US)}$). Before 6^{th} second, $W_1 = W_2 = W_3 = 1$ in both (US) and (WS) runs. After 6 seconds, $W_1^{(WS)}$ has been set to 4 leading to $P_T^{(WS)} = 1.\bar{6}$ and to $W_T^{(WS)} = 5$. In Table 5.2, wrong values for the (WS) run are reported.

Clearly, looking at Figs. 5.7, 5.8 and at Table 5.2, if the global sharing coefficient W_T is not kept constant during sharing transients, the output speed is affected. In-fact, like it is shown in Fig. 5.9, during load transients

at second 6^{th} and 9^{th}, the sum $i_{qT}^{(WS)}$ in (5.6) is not constant.

$$i_{qT}^{(WS)} = \sum_{j}^{N} i_{qj}^{(WS)} \tag{5.6}$$

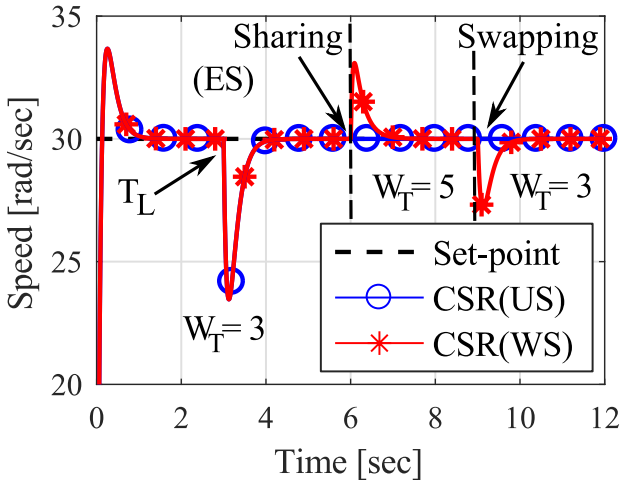

Figure 5.7: Simulated output speed without keeping constant the global sharing coefficient W_T.

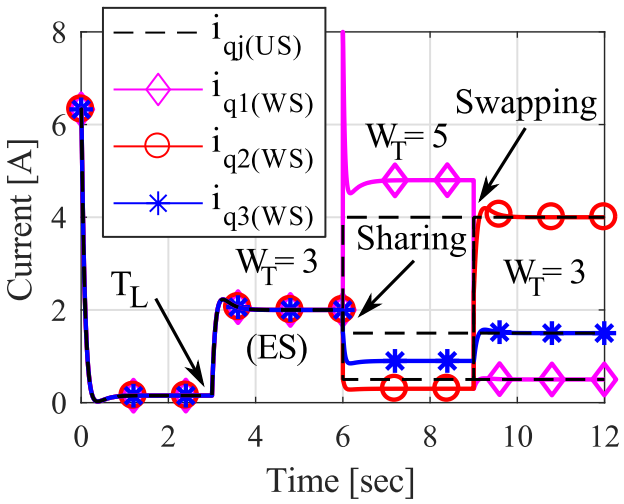

Figure 5.8: Simulated i_q currents without keeping constant the global sharing coefficient W_T.

Table 5.2: Sharing coefficients with variable W_T - (WS) run

	$0 \div 6[sec]$			$6 \div 9[sec]$			$9 \div 12[sec]$		
j	$P^{(WS)}$	$W^{(WS)}$	$i_q^{(WS)}$	$P^{(WS)}$	$W^{(WS)}$	$i_q^{(WS)}$	$P^{(WS)}$	$W^{(WS)}$	$i_q^{(WS)}$
1	1/3	1	2	4/3	4	4.8	1/12	0.25	0.5
2	1/3	1	2	1/12	0.25	0.3	2/3	2	4
3	1/3	1	2	1/14	0.75	0.9	1/4	0.75	1.5
$\sum$	1	$N = 3$	6	$1.\bar{6}$	5	6	1	$N = 3$	6

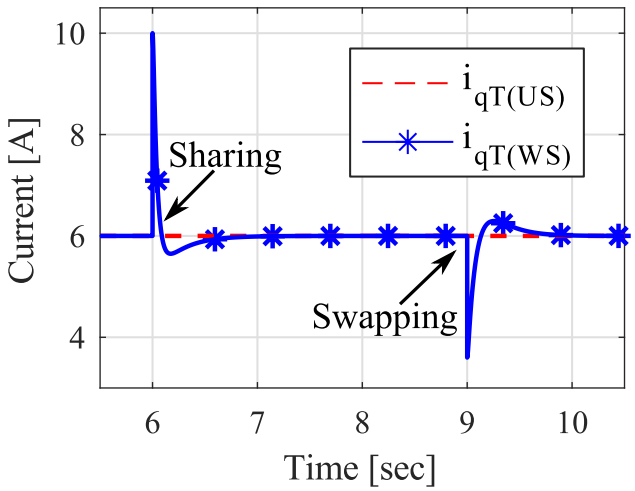

Figure 5.9: With variable W_T, $i_{qT} = \sum_j^N i_{qj}^{(WS)}$ is not constant.

Considering the previous discussion, it is possible to conclude that constant speed during sharing transients is achieved if and only if the sum of the i_q currents is kept constant during sharing transients (5.7).

$$i_{qT}^{(ES)} = \sum_j^N i_{qj}^{(ES)} = i_{qT}^{(US)} = \sum_j^N i_{qj}^{(US)} \tag{5.7}$$

5.3 Post-fault compensation strategy

In this section, a speed dynamic compensation strategy based on the power sharing capability discussed in 5.2.2 is presented. In this section, it is assumed the following:

1. After a generic fault, the module is able to disconnect the machine from the converter (open circuit condition denoted with $_{OC}$);
2. Current bandwidths $\omega_{c\Lambda}$ can be considered constant;
3. After the fault occurred, all the modules are aware of the fault in order to re-configure itself.

Due to its distributed nature, if compared to the TF configuration in Fig. 4.5b, improved fault tolerance can be achieved with the CSR configuration in Fig. 5.3. However, if the *global sharing coefficient* in (5.3) is not kept constant in case of fault, speed dynamic is degraded. Assuming current bandwidths $\omega_{c\Lambda}$ are kept constant after the fault occurred, defining N_A the number of segments producing torque in faulty condition, fully fault compensation in case of fault is guaranteed by the following equation:

$$W_T^{(FC)} = \sum_j^{N_A} W_j^{(FC)} = W_T^{(NC)} = \sum_j^{N} W_j^{(NC)} \tag{5.8}$$

where (FC) and (NC) denote fault and nominal condition, respectively.

For example, if in nominal condition $W_1^{(NC)} = W_2^{(NC)} = W_3^{(NC)} = 1$, assuming constant $\omega_{c\Lambda}$ in case of fault of the third drive, the remaining two loop gains should be updated with $W_1^{(FC)} = W_2^{(FC)} = 1.5$ ($W_3^{(OC)}$ can be assumed equal to zero). In Fig. 5.10, start-up and load step response in the following operating conditions:

1. nominal condition (CSR NC) - ($W_{1,2,3}^{(NC)} = 1$);
2. fault condition not updating (CSR FC NU) loop gains - ($W_{1,2}^{(FC)} = 1$);

3. fault condition updating (CSR FC U) loop gains - ($W_{1,2}^{(FC)} = 1.5$);

are shown. If $\omega_{c\Lambda}$ do not change in case of fault, updating the sharing gains

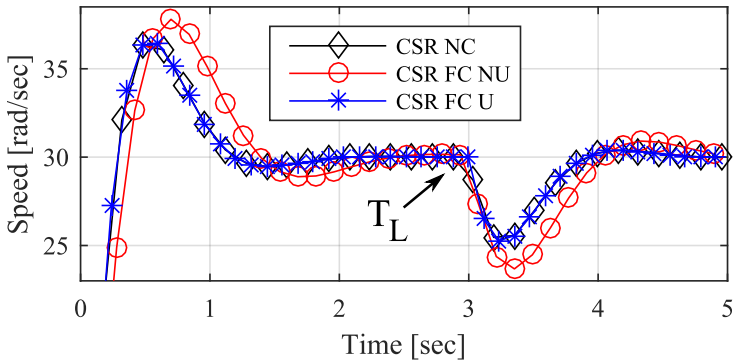

Figure 5.10: In case of fault, (5.8) guarantees constant speed dynamics.

allows the speed dynamic to be restored to its nominal condition. How much the current bandwidths $\omega_{c\Lambda}$ are affected cannot be generalised and it should be evaluated case by case. If current control loop performance degradation is found not acceptable, current PI controllers should be adjusted in order to keep constant $\omega_{c\Lambda}$ as much as possible.

5.4 Final considerations

In this chapter, how to achieve power sharing without affecting the shaft speed has been explained. For a given application, the following are the possible solutions to set the desired sharing coefficients in order to keep constant the global sharing coefficient W_T:

- Pre-programming the coefficients;
- Super-visioning centralised controller;
- Inter-module communication in a distributed cooperative control framework like explained in [67];

For simplicity, in Chapter 8 when presenting the experimental work, the first solution is adopted.

As later shown in section 6.3, a step change in the *sharing coefficients* is instantaneously reflected in a step of the current loop set-points, causing current harmonic distortion leading to the following undesired effects:

- higher Electro Magnetic Interferences (EMI);
- poorly damped sharing transient leading to torque stresses and undesired vibrations;

In the next chapter, a novel droop controller guaranteeing smoother transients after step changes in power sharing demand is presented.

Chapter 6

Novel Speed-Drooped controller for power sharing

In this chapter, the novel speed-drooped controller will be introduced. For simplicity, a multi-drive system with just two modules is considered. The speed-drooped controller, or droop or sharing controller, is capable of controlling the time constant of power sharing transients, thus it guarantees reduced current harmonic distortion during sharing transients. In Section 6.3, the novel controller is compared against the sharing coefficients explained in Chapter 5. Furthermore, keeping constant the sum of the i_q currents like in (5.7), constant output speed during power sharing transients is guaranteed.

In Chapters 7 and 8, the droop controller will be experimentally validated on the two following rigs:

- multi-drive system with two induction motors on the same shaft;
- multi-three-phase electrical machine with nine phases;

respectively.

6.1 Introduction

From a general perspective, droop control is a very well known technique used in power systems to share power demanded by the grid among different generation systems [68, 69], in un-interruptible power supply (UPS)[70], and DC/DC converter [71] scenarios. In AC power system scenario, the basic droop characteristic is a linear function with a negative coefficient on the Frequency-Active power plane governed by the following equation [72]:

$$\omega_i = \omega_0 - K_D P_i \tag{6.1}$$

where ω_i and ω_0 are the angular frequency of the output voltage and of the base reference respectively, P_i is the output active power, and K_D is the droop coefficient. The greater the frequency the less is the power produced by the generation plant. Changing the coefficients of individual power stations sets the power produced by each one of them, Fig. 6.1a. Thanks to this, the way power injected into the grid is partitioned among generation plants is a function of the droop coefficients [73].

Translating these concepts into a torque control diagram like the one in Fig 4.2 and its implementation in Fig. 4.1, power sharing among the drives is possible. The key point here is the droop plane in Fig. 6.1b. Generation

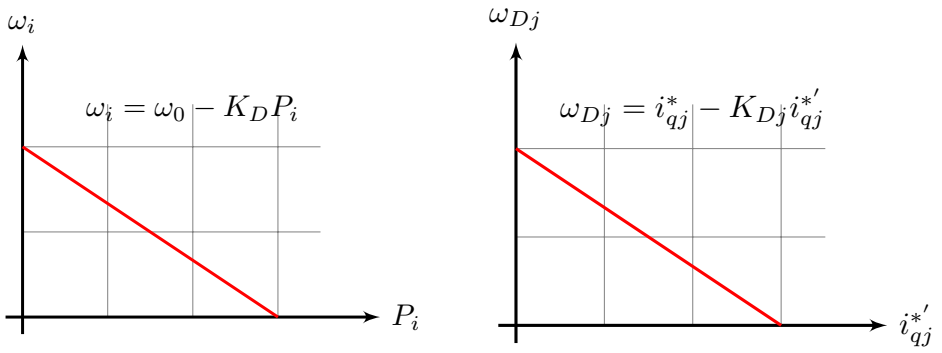

(a) Droop plane in power system. (b) Droop plane in motor control.

Figure 6.1: Droop planes comparison.

systems are defined by angular frequency ω and the active power P (Fig. 6.1a), however multi-drive systems are described by the current reference i^*_{qj} - set by the speed regulator - and the new current set-point $i^{*'}_{qj}$ like in the following equation (Fig. 6.2):

$$\omega_{Dj} = i^*_{qj} - K_{Dj} i^{*'}_{qj} \tag{6.2}$$

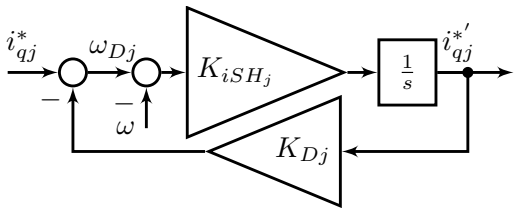

Figure 6.2: Novel droop controller G_{Dj} implementation with speed feedback.

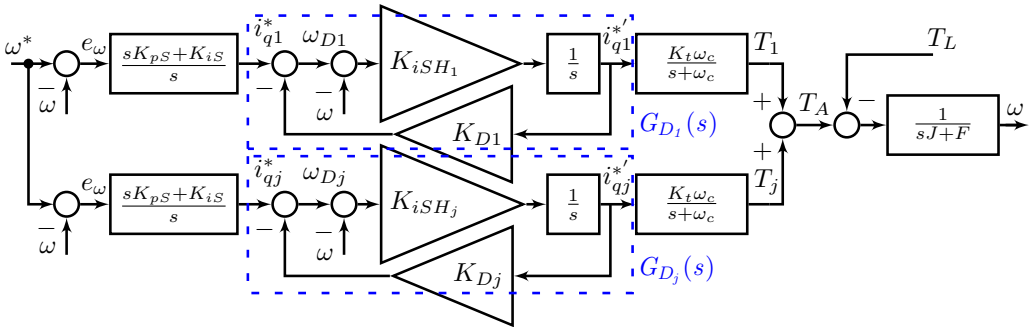

Figure 6.3: Novel speed-drooped control diagram with droop controllers.

Indicating the generic inverter (or module) with j, Fig. 6.3 shows how the droop has been implemented in the proposed speed droop system. Even if the same approach can be applied to a multi-three-phase system with a generic number N of modules, in Fig. 6.3 the full control scheme is reported for $N = 2$. Like in Fig. 4.2, the mechanical load is common and represented with a linear model with inertia J and friction F, and every q-current control loop is modelled as a low-pass filter with bandwidth ω_c and phase margin φ_c. The controllers in control schematic in Fig. 6.3 are the following:

- Proportional-Integral q-current controller

$$PI_{Iq} = K_{pIq} + K_{iIq}/s \tag{6.3}$$

  within the current loop modelled by the transfer function $\omega_c/(s+\omega_c)$ as discussed in section 3.4;

- Speed-drooped, or droop or sharing, controller G_{Dj} shown in Fig. 6.2 characterised by bandwidth and phase margin ω_{SH} and φ_{SH}, respectively. It will be explained in the next section;

- Proportional-Integral speed, or compensation, controller characterised by bandwidth and phase margin ω_s and φ_s, respectively.

$$PI_S = K_{pS} + K_{iS}/s \tag{6.4}$$

  with the goal of restoring the desired speed set-point and of fulfilling the speed dynamic constraints

After reading section 6.4, it will be clear that the sharing dynamic can not be faster than the current one and slower than the speed one. For now, the following inequality:

$$\omega_s \leq \omega_{SH} \leq \omega_c \tag{6.5}$$

can be verified looking at the three nested loops in Fig. 6.3.

6.2 Speed drop and compensation loop

In order to better understand the droop controller G_{Dj} (Fig. 6.2) between the current PI and the compensation PI, consider first a simple integral controller where $K_{Dj} = 0$ like in Fig. 6.4. The regulator K_{iSHj}/s processes the error with respect to a constant reference $\omega_{Dj} = i^*_{qj}$, and it defines the current set-point $i^{*'}_{qj}$. Introducing the droop coefficients K_{Dj}, the speed set-point ω_{Dj} is now a function of the ideal set-point i^*_{qj} minus a component

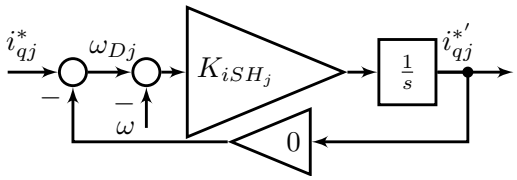

Figure 6.4: Droop controller with $K_D = 0$.

dependent on the actual current set-point $i^{*'}_{qj}$ and proportional to the current torque demand. The correlation among values is reported in Fig. 6.1b and the droop regulator in Fig. 6.2 can be written as:

$$G_{Dj}(s) = \frac{K_{iSHj}}{s + K_{iSHj}K_{Dj}} = \frac{i^{*'}_{qj}}{i^*_{qj}} \tag{6.6}$$

If we assume an ideal inner current loop, i.e. $i_{qj} = i^{*'}_{qj}$, and we assume constant current set-point $i^*_{qj} = \omega^*$, the steady state speed error resulting from the inner drooped loops can be calculated from Fig. 6.3 taking the limit for $s \to 0$:

$$\begin{gathered} \omega = \omega^* \frac{\gamma}{\gamma + 1} - \frac{T_L}{F + \varepsilon K_t} \\ \text{with } \varepsilon = \sum_j^N \frac{1}{K_{Dj}} \text{ and } \gamma = \frac{\varepsilon K_t}{F} \end{gathered} \tag{6.7}$$

As expected, the droop causes an error on the speed ω, and the compensation PI (PI_S) has been introduced to restore the speed set-point ω^* (Fig. 6.5), by shifting the droop characteristics up or down to guarantee that the steady state equilibrium in (6.7) matches the set-point ω^*.

In a previous work, other researchers [74] developed a similar drooped-speed control for mitigating the 0-sequence current between two paralleled drives connected to a three phase machine, but without compensating the error introduced by the droop coefficient. In the proposed procedure, in Section 6.5, the droop loop has been taken into account from the beginning, compensating the final speed and guaranteeing desired performances.

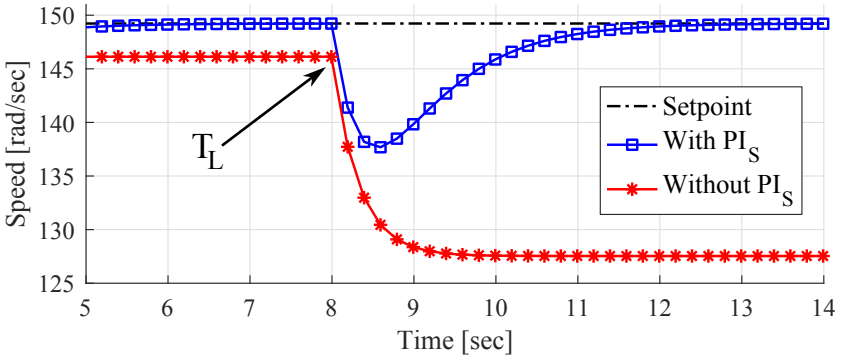

Figure 6.5: With compensation PI the final speed tracks the set-point. At second 8 the load ($T_L = 17Nm$) is attached and the speed error increases like described by (6.7).

6.3 Novel droop controller versus sharing coefficients

Assuming that at the frequencies of interest the integrator of the droop regulator I_{SHj} has a gain which is high enough to assume

$$|I_{SHj}| = |\frac{K_{iSHj}}{s}| >> K_{D_j} \tag{6.8}$$

an intuitive understanding of the system operation can be better gained. Under the condition in (6.8) the scheme in Fig. 6.3 can be simplified into a Common Speed Reference system with power sharing capabilities like the one in Fig. 5.3, where the PI_S remain in place but all the inner loops with droop, including K_{iSHj}, K_{Dj} and the inner adder, can be replaced by a gain $1/K_{Dj} = W_j$ receiving the output of the speed PIs, and directly providing the current reference for the inner current loops in Fig. 6.6.

This simplified approach where the droop is reduced to a set of paralleled controllers with different gains ($1/K_{Dj} = W_j$) would be the simplest approach for a system with power sharing capabilities. Such a kind of arrangement would be equivalent to a common speed reference system with *sharing coefficients* like the one discussed in chapter 5 and shown in Fig. 5.3.

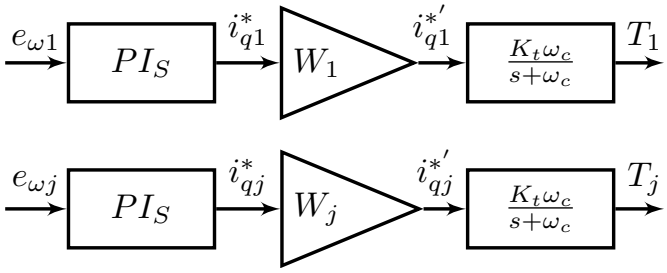

Figure 6.6: Simplified droop under condition in (6.8) is a CSR with *sharing coefficients* $W_j = 1/K_{Dj}$.

However in the latter case, a change in the coefficients W_j would be instantaneously reflected in a change of the references for the current loops, causing a poorly damped sharing transient leading to torque stresses and undesired vibrations.

In the control structure proposed in this thesis, one of the desired features is to be able to control the current sharing dynamic after sharing ratio step changes. In this case, the droop controller in Fig. 6.2 instead of a simple *sharing coefficient* (Figs. 5.3 and 6.6) guarantees smoother transients after step changes in power sharing demand.

In order to better explain this concept and the benefits introduced by the droop controller, different minimalistic input control diagrams and their relative transformed time domain value a are shown in Figs. 6.7 and 6.8, respectively. The droop controller in Fig. 6.7c allows the step change in power demand to be regulated with a transient characterised by a time constant $\tau_{sharing}$ defined later on in Sec. 6.6. Looking at the time domain values in Fig. 6.8, Electro Magnetic Interferences (EMI) and current harmonic distortion are clearly reduced when using the droop controller instead of a simple step or ramp in Fig. 6.7a and 6.7b, respectively.

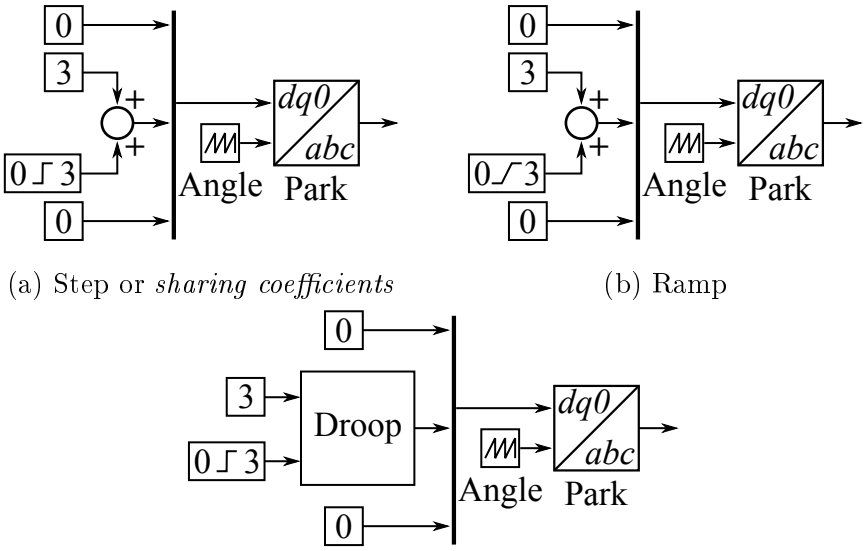

(a) Step or *sharing coefficients* (b) Ramp

(c) Droop controller in Fig. 6.2

Figure 6.7: Different sharing controller implementation. Angle period has been set equal to 2 seconds.

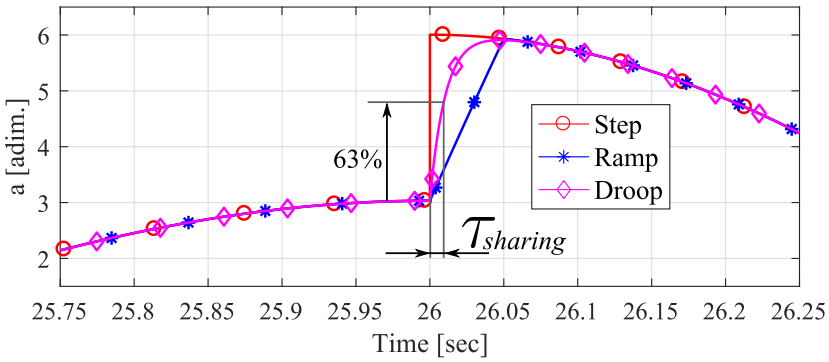

Figure 6.8: a value from Park's transformations in Fig.s 6.7.

6.4 Simplified equivalent model

Tuning of compensation PIs and droop controllers has to be done on a plant considering the whole system assuming equal power sharing (ES) where every module is producing $1/N$ of the total power. The simplified equivalent model here explained will be used in section 6.5 where the overall control design

procedure is summarised.

Assuming that the load power is equally split among the N modules, the schematic in Fig. 6.3 can be simplified with the collective one in Fig. 6.9. The parallel of the N droop controllers $G_{Dj}^{(ES)}$ (where (ES) stands for equal

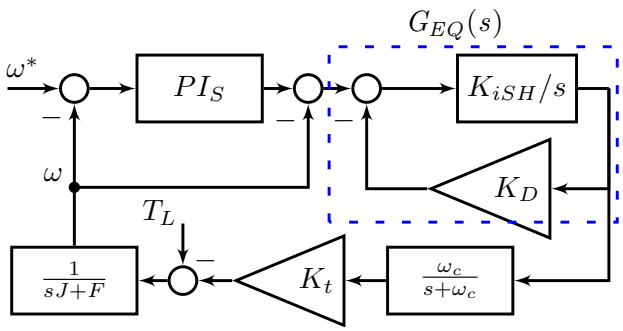

Figure 6.9: Equivalent collective control scheme valid when the load power is equally split among the N modules.

sharing) has been replaced by an equivalent collective controller:

$$G_{EQ} = NG_{Dj}^{(ES)} \tag{6.9}$$

The equality in (6.9) can be satisfied if and only if $K_{iSH} = K_{iSHj}^{(ES)}N$ and $K_D = K_{Dj}^{(ES)}/N$ as emphasised by:

$$G_{EQ}(s) = \frac{NK_{iSHj}^{(ES)}}{s + K_{iSHj}^{(ES)}N\frac{K_{Dj}^{(ES)}}{N}} = NG_{Dj}^{(ES)}(s) \tag{6.10}$$

From the above equation it can be observed that the whole system can be modelled as an equivalent single module with integral sharing gain K_{iSH} and droop gain K_D:

$$K_{iSH} = K_{iSH_j}^{(ES)}N \quad K_D = \frac{K_{D_j}^{(ES)}}{N} \tag{6.11}$$

The K_D and the K_{iSH} gains in (6.11) can be defined as the collective droop and the collective integral gain coefficient, respectively.

The equivalence in (6.9) can be verified by plotting the Bode diagrams in Fig. 6.10.

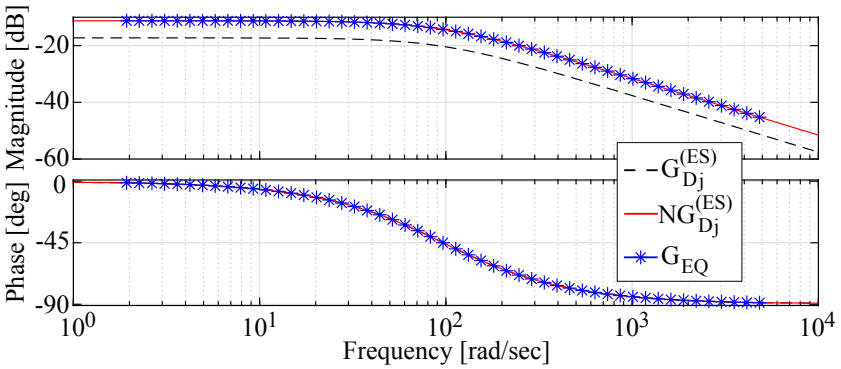

Figure 6.10: Bode diagrams of transfer functions in (6.9).

6.5 Control design approach

Based on the previous discussion, and maintaining the same approximations, a simple design procedure can be proposed. The inner current loop is designed to guarantee maximum bandwidth (ω_c). Then, the collective droop coefficient K_D must be chosen with (see Fig. 6.1b):

$$K_D = \Delta\omega_{MAX}/I_{TOT} = \Delta\omega_{MAX}/\left(\sum_j^N I_{nom_j}\right) \tag{6.12}$$

where $\Delta\omega_{MAX} = (\omega^* - \omega)$ is the steady state speed error (without compensation PI) at full load, $I_{nom,j}$ is the nominal current on the q-axis of the j-th module. Referring to Fig. 6.9 and for a given sharing bandwidth

$$\omega_s < \omega_{SH} \leq \omega_c \tag{6.13}$$

the collective integral gain K_{iSH} can be calculated imposing the phase margin φ_{SH} (from now called sharing phase margin) on the opened sharing loop transfer function described by the following:

$$\angle G_{SH_{OL}}(s) = \angle G_{EQ}(s) G_I(s) K_t G_M(s) = \varphi_{SH} - \pi \tag{6.14}$$

where $G_M(s) = 1/(sJ + F)$ is the transfer function of the mechanical load, K_t is the machine constant ($K_t = T/i_q$), and $G_I(s) = \omega_c/(s + \omega_c)$ is the

current control closed loop. Equation (6.14) leads to the following analytical expression for the collective integral gain:

$$K_{iSH} = \frac{\omega_{SH}}{\tan\left[-\varphi_{SH} + \pi - \operatorname{atan}\left(\frac{\omega_{SH}}{\omega_c}\right) - \operatorname{atan}\left(\frac{\omega_{SH}J}{F}\right)\right] K_D} \tag{6.15}$$

The design of the compensation PI can be based on the equivalent collective scheme in Fig. 6.9. The plant for designing PI_S is the closed inner sharing loop transfer function $G_{SH_{CL}}(s)$, that can be written as:

$$\begin{aligned} G_{SH_{CL}}(s) &= G_{SH_{OL}}(s)/(1 + G_{SH_{OL}}(s)) \\ G_{SH_{OL}}(s) &= G_{EQ}(s)G_I(s)K_tG_M(s) \end{aligned} \tag{6.16}$$

Under the previous hypothesis of balanced load and provided that $G_{EQ} = NG_{Dj}^{(ES)}$, the same response of the designed equivalent collective system when using N modules can be achieved multiplying by N the collective droop gain and dividing by N the collective integral gain like in (6.11).

In Fig. 6.11, output speed from the speed-drooped control diagram in Fig. 6.3 and the equivalent collective scheme in Fig. 6.9 in equal sharing (ES) condition are compared. Design input parameters, regulator coefficients, and

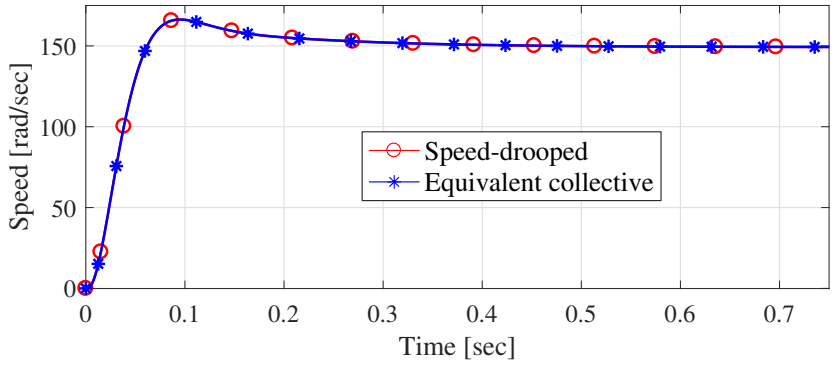

Figure 6.11: Equivalence between the speed-drooped control diagram in Fig. 6.3 and the equivalent collective scheme in Fig. 6.9 in ES condition.

their relative equations are summarised in Table 6.1.

Table 6.1: Design summary

Input data	Design input data	Output data	Eq.
Current loops			
r_s, q_1, d_1 from (2.33)	ω_{cq}, φ_{cq}, ω_{cd}, φ_{cd}	K_{pIq}, K_{iIq}, K_{pId}, K_{iId}	(3.20), (3.21)
Sharing loops - I			
I_{TOT}	$\Delta\omega_{MAX}$	K_D	(6.12)
K_D	N	$K_{Dj}^{(ES)}$	(6.11)
K_t, ω_c, J, F	ω_{SH}, φ_{SH}	K_{iSH}	(6.15)
K_{iSH}	N	$K_{iSHj}^{(ES)}$	(6.11)
Speed loops			
K_D, K_{iSH}, K_t, ω_{cq}, J, F	ω_s, φ_s	K_{pS}, K_{iS}	(6.16)

6.6 Droop slopes and current sharing dynamic

The equivalent collective model (Fig. 6.9) built on the previous section has assumed power equally shared among the N modules of the multi-three-phase system. The total power P_{TOT} is given by the sum of all the nominal torques produced by each module multiplied by the shaft speed. Since currents and torques are directly proportional ($T = K_t i$), the *j-th* power in *p.u.* is described by the following:

$$P_j = \frac{I_{nom,j}}{\sum_j^N I_{nom,j}} [p.u.] \tag{6.17}$$

where $I_{nom,j}$ is the nominal current on the q-axis of the *j-th* module. From Fig. 6.3, it can be noticed that the current set-points are the output of the sharing regulators G_{Dj}. Provided that in the steady state the magnitude of the droop loops is the reciprocal of the droop coefficient $|G_{Dj}|_{s\to 0} = 1/K_{Dj}$, the total power P_{TOT} can be described as ε (the sum of the reciprocals as previously defined in (6.7)). Therefore, the power provided by each of the N modules in general (not only when the power is equally split) can be written

as:

$$P_j = \frac{1/K_{Dj}}{\sum_j^N (1/K_{Dj})} = \frac{1/K_{Dj}}{\varepsilon} \; [p.u.] \tag{6.18}$$

Thanks to (6.18), as long as ε is kept constant, unbalanced power sharing can be achieved just by changing the droop coefficients. Whenever a different sharing ratio is needed (not equal sharing like previously supposed), the droop coefficients K_{Dj} could be updated by a supervisory controller or programmed off-line a priori. The graphical representation of (6.18) is given in Fig. 6.12. Unfortunately, simply changing the droop gains leads to different

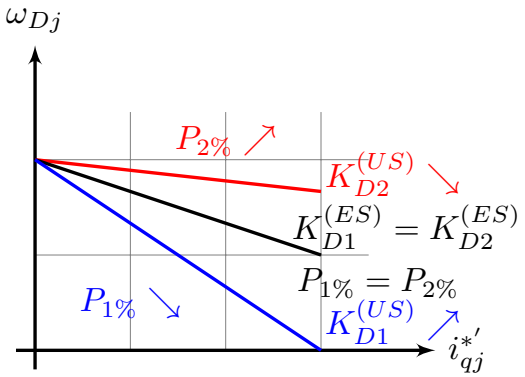

Figure 6.12: Different coefficients produce different amount of torque.

and dynamically unbalanced droop controllers with different time constants as shown later on. Constant speed of the shaft on power sharing transients can be achieved if and only if the collective sharing regulator transfer function is kept constant:

$$\sum_j^N G_{Dj}^{(US)}(s) = N G_{Dj}^{(ES)}(s) = G_{EQ}(s) \tag{6.19}$$

Equations (6.19) and (6.10) emphasise that whenever $K_{Dj}^{(ES)}$ is updated, $K_{iSHj}^{(ES)}$ must be updated accordingly. Provided that $\sum_j^N P_j = 1$, (6.19) can be satisfied by dividing the individual equal power droop coefficients $K_{Dj}^{(ES)}$ by a factor:

$$\xi_j = N P_j \tag{6.20}$$

and multiplying the individual integral gain $K_{iSHj}^{(ES)}$ by the same factor ξ_j like in the following combining (6.6) and (6.19):

$$\frac{NK_{iSHj}^{(ES)}}{s + K_{iSHj}^{(ES)}K_{Dj}^{(ES)}} = \sum_{j}^{N} \frac{\overbrace{K_{iSHj}^{(ES)}\xi_j}^{K_{iSHj}^{(US)}}}{s + \underbrace{K_{iSHj}^{(ES)}\xi_j}_{K_{iSHj}^{(US)}} \underbrace{\frac{K_{Dj}^{(ES)}}{\xi_j}}_{K_{Dj}^{(US)}}} \tag{6.21}$$

Fig. 6.12 shows a graphical representation of the power sharing change for $N = 2$, referring to the single-module droop characteristics. As a final result, changing the power contribution of module 1 from $0.5[p.u.]$ (equal sharing) to an arbitrary P_1 can be achieved dividing the droop slope K_{D_1} by $\xi_1 = NP_1$ and dividing the slope K_{D_2} by $\xi_2 = N(1 - P_1) = NP_2$. Since the current sharing dynamic is governed by the droop controller G_{Dj}, its closed loop time constant is described by the following equation:

$$\tau_{sharing,j} = \frac{1}{K_{Dj}K_{iSHj}} \tag{6.22}$$

Equation (6.22) confirms that updating the integral gains, constant sharing dynamic is guaranteed. For this reason, in order to keep constant the sharing regulator transfer function, both the integral gains $K_{iSHj}^{(ES)}$ must be scaled accordingly like in (6.21).

Bode plots in Fig. 6.13 show transfer functions equivalence in (6.19).

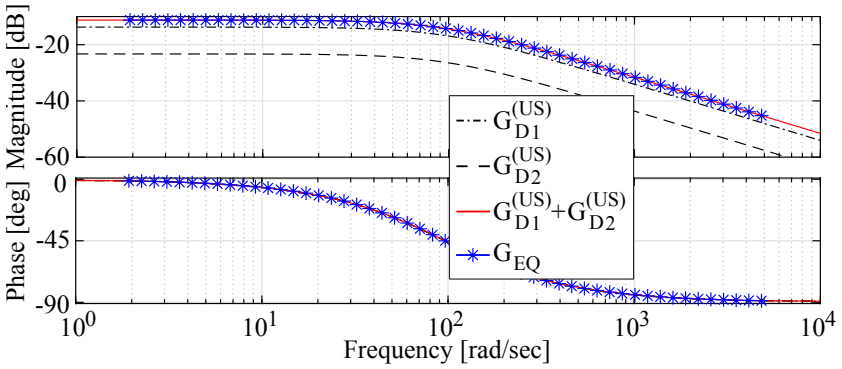

Figure 6.13: Updating the integral gains K_{iSHj}, constant magnitude with different power ratios is guaranteed.

In Fig. 6.14, the two i_q currents after a sharing ratio step are reported. After 26 seconds, the sharing ratios have been set from $0.50\% \div 0.50\%$ to $0.75\% \div 0.25\%$, and the i_q currents at steady state changed from $3A$ to $4.5A$ and $1.5A$, respectively. It is possible to notice how without updating the

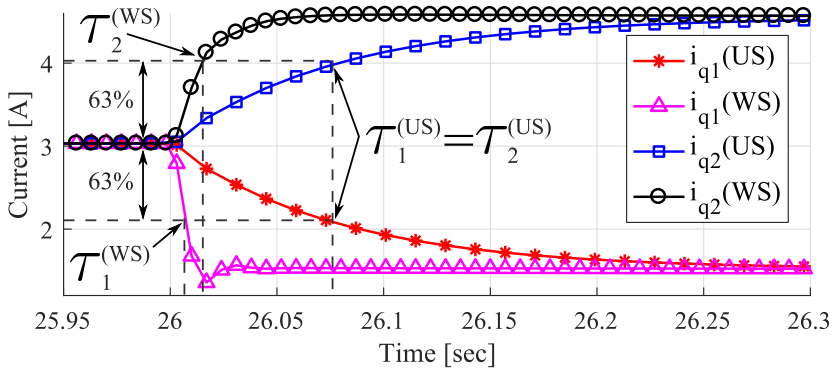

Figure 6.14: Current sharing dynamic with and without updating the integral gains K_{iSHj}. Sharing ratio from 0.5%÷0.5% (equal sharing) to 0.75%÷0.25%.

integral gains K_{iSHj} (denoted by (WS)), different time constant ($\tau_{sharing,j}$ from (6.22)) are obtained. In-fact, whilst $\tau_1^{US} = \tau_2^{US}$, $\tau_1^{WS} \neq \tau_2^{WS}$. Constant integral gains K_{iSHj} lead to total current variation within the electrical motor during sharing transients. In Fig. 6.15, the total current $i_{qTOT} = i_{q1} + i_{q2}$

during the power sharing transient for constant (WS) and not constant (US) integral gains are shown.

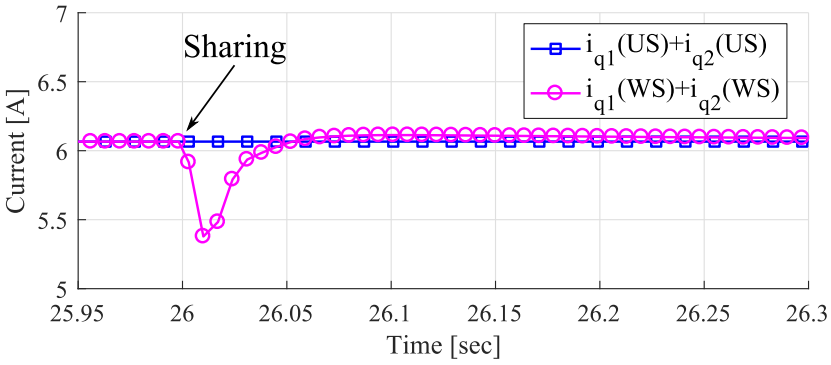

Figure 6.15: i_q currents sum updating (US) and not updating (WS) the integral sharing coefficient.

Not constant i_{qTOT} is reflected on the angular speed of the shaft in Fig. 6.16. In-fact, updating the integral gains, the speed is tracking the set-point during power sharing transients.

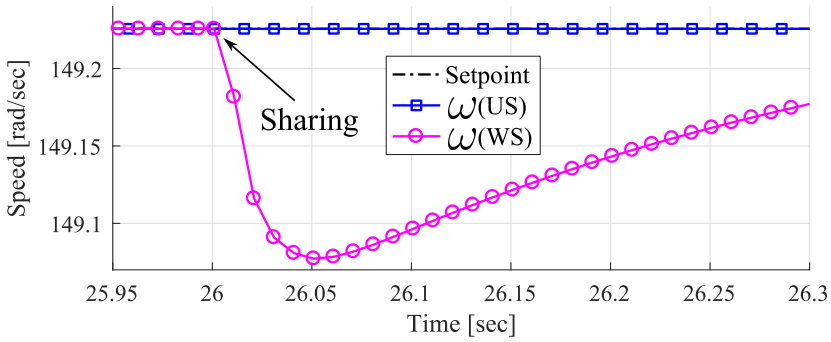

Figure 6.16: Updating the integral gains, the final speed is not affected.

Two different case studies on a multi-drive rig and on a multi-three-phase motor with relative experimental results will be provided in Chapters 7 and 8, respectively.

6.7 Summary

In order to provide a clearer vision of the whole picture, a short summary is provided.

For a given multi-three-phase motor or a multi-drive system with N modules and rated current $I_{TOT} = \sum_j^N I_{nom_j}$, controller coefficients can be computed with equations in Table 6.2. Per-module droop controller coefficients $K_{Dj}^{(ES)}$ and $K_{iSHj}^{(ES)}$ are assuming the power equally split among the N modules. After computing $K_D^{(ES)}$ with (6.12), $K_{iSH}^{(ES)}$ can be computed with the two following methods:

1. with (6.15) imposing φ_{SH} and ω_{SH} (with $\omega_s < \omega_{SH} \leq \omega_c$).

2. imposing $\tau_{sharing}$ with the following equation:

$$K_{iSH} = \frac{1}{K_D \tau_{sharing}} \tag{6.23}$$

   However, condition in (6.13) and stability margins of $G_{SH_{OL}}(s)$ in (6.16) must be verified. If the $G_{SH_{OL}}$ is stable and the droop loop cross-over frequency is in between the current loop and the speed loop cross-over frequencies, the speed regulator can be designed;

Once the droop controller is designed with one of the two methods above, the speed regulator PI_S can be computed on the $G_{SH_{CL}}$ plant in (6.16) imposing ω_s (with $\omega_s < \omega_{SH}$) and φ_s;

Provided that $\sum_j^N P_j = 1$, whenever required by the particular application, power ratios can be changed by dividing the individual equal power droop coefficients $K_{Dj}^{(ES)}$ by a factor $\xi_j = NP_j$ and multiplying the individual integral gain $K_{iSHj}^{(ES)}$ by the same factor ξ_j.

$$K_{iSHj}^{(US)} = K_{iSHj}^{(ES)} \xi_j \quad K_{Dj}^{(US)} = \frac{K_{D_j}^{(ES)}}{\xi_j} \tag{6.24}$$

These guarantee constant speed during power sharing transients.

Table 6.2 expands Table 6.1 adding equations for designing the sharing loops with the two different methods explained above.

Table 6.2: Expanded design summary

Input data	**Design input data**	**Output data**	**Eq.**
Current loops			
r_s, q_1, d_1 from (2.33)	ω_{cq}, φ_{cq}, ω_{cd}, φ_{cd}	K_{pIq}, K_{iIq}, K_{pId}, K_{iId}	(3.20), (3.21)
Sharing loops - Method I			
I_{TOT}	$\Delta\omega_{MAX}$	K_D	(6.12)
K_D	N	$K_{Dj}^{(ES)}$	(6.11)
K_t, ω_c, J, F	ω_{SH}, φ_{SH}	K_{iSH}	(6.15)
K_{iSH}	N	$K_{iSHj}^{(ES)}$	(6.11)
Sharing loops - Method II (stability of $G_{SH_{OL}}(s)$ in (6.16) and (6.13) must be verified)			
I_{TOT}	$\Delta\omega_{MAX}$	K_D	(6.12)
K_D	$\tau_{sharing}$	K_{iSH}	(6.23)
K_D	N	$K_{Dj}^{(ES)}$	(6.11)
K_{iSH}	N	$K_{iSHj}^{(ES)}$	(6.11)
Speed loops			
K_D, K_{iSH}, K_t, ω_{cq}, J, F	ω_s, φ_s	K_{pS}, K_{iS}	(6.16)
Power sharing			
N, $K_{Dj}^{(ES)}$, $K_{iSHj}^{(ES)}$	P_j	$K_{Dj}^{(US)}$, $K_{iSHj}^{(US)}$	(6.20),(6.24)

Chapter 7

Experimental results - Multi-drive rig

In this chapter and in the following one, experimental validation of the novel droop controller introduced in Chapter 6 is provided on the multi-drive rig with two induction motors on the same shaft. Having two different stators, there are no mutual electro-magnetic interactions between the two rotating reference frames. The coupling between the motors are stiff enough to be considered infinitely rigid.

In Chapter 8, the proposed droop controller is validated on a multi-three-phase machine with nine phases where current controllers have been designed on the first harmonic inductances d_1 and q_1. Furthermore, the droop controller sharing transient will be compared against the one obtained thank to sharing coefficients.

7.1 Introduction

The drop controller has been validated on the experimental rig in Fig. 7.1. The multi-three-phase motor has been emulated using three independent

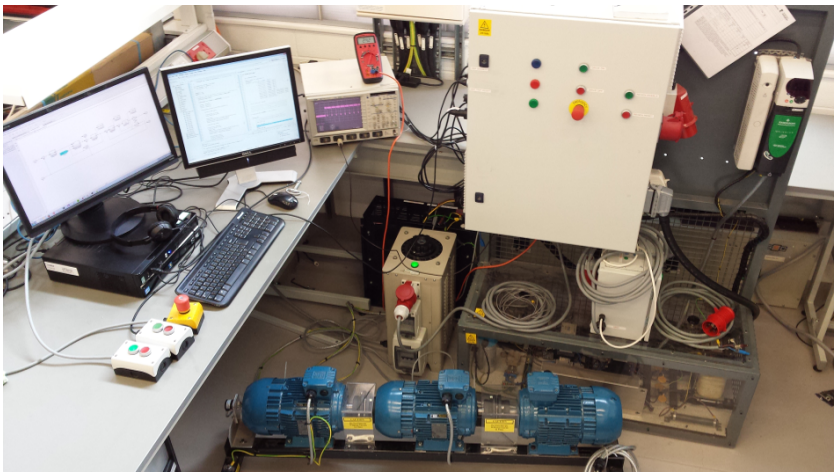

Figure 7.1: Experimental rig

induction machines on the same shaft. Every motor is coupled to the next one by a rigid joint. Speed information is provided by an incremental encoder coupled to the left motor.

In this configuration the mutual interactions between the three-phase sets of windings are not present. The first two machines have been controlled as an equivalent multi-three-phase motor with $N = 2$ and they have been fed by a custom two level inverter [30, 75], switching at $f_{SW} = 5kHz$ and with DC bus at $V_{DC} = 540V$. The third motor has been controlled as a load with a commercial inverter (Unidrive SP by Emerson). The three motors are identical and their plate data is reported in Table 7.1.

The custom inverter was controlled by a custom control platform with one Digital Signal Processor (DSP) and one Field Programmable Gate Array (FPGA) [30, 75]. Even if the drive is unique, in order to emulate the condition where the modules are completely independent, control loops for the two modules have been written independently without sharing information except

Table 7.1: Motors plate data

V	Hz	kW	rad/sec	A	$\cos(\phi)$
380	50	3.0	149.2	6.13	0.85

for the speed. The speed-drooped controller has been validated coding on the custom platform two Field Oriented Controllers (FOCs) with Indirect Rotor Flux Observer (IRFO). In Fig. 7.2, implementation of the controllers are shown, the IRFO and the speed filter have been omitted for simplicity.

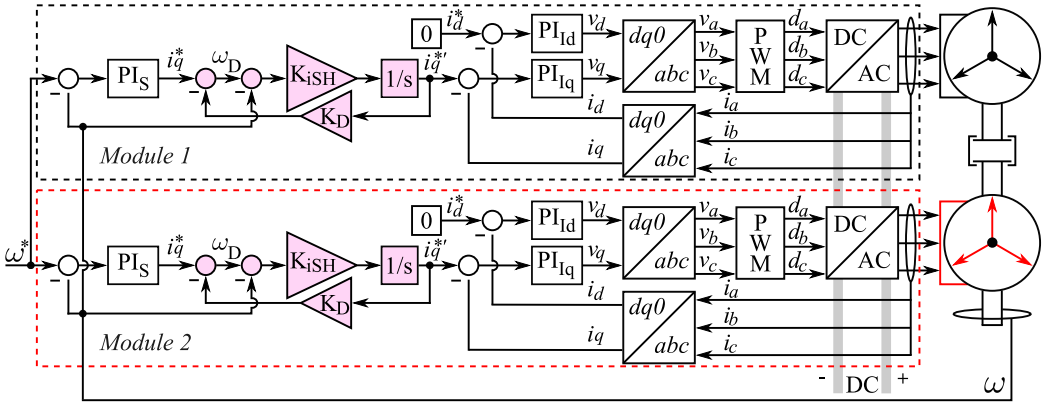

Figure 7.2: Droop controller implementation. IRFO and speed filter have been omitted.

7.2 Control design - Case study

The system has been designed considering a set-point speed $\omega^* = 149.2[rad/s]$ equal to the nominal speed in Table 7.1. Referring to the equivalent collective scheme in Fig. 6.9, the current controller has been assigned a bandwidth $\omega_{cq} = 300[rad/sec]$ and a phase margin $\varphi_{cq} = 60°$, whereas the outer loop (PI_S) has been tuned with a bandwidth $\omega_s = 30[rad/sec]$ and $\varphi_S = 60°$. The droop loop, or sharing loop, has been set up with different bandwidth ($\omega_s \leq \omega_{SH} \leq \omega_{cq}$) and phase margin ($\varphi_{SH}$) values in order to highlight

and validate how the proposed strategy is able to control the current sharing dynamic. The collective droop gain coefficient can be obtained with (6.12) imposing $\Delta\omega_{MAX}$. This would be the steady state output speed of the system without the compensation PI_S. In this particular case, the maximum delta has been set up equal to the 15% of the reference speed ($\Delta\omega_{MAX} = 22.38[rad/sec]$). Considering a total nominal current of $6.13[A]$ in order to accommodate the fault of one of the two motors, (6.12) leads to the collective droop coefficient $K_D = 3.65[(rad/sec)/A]$. In the first results, the sharing loop has been set with $\omega_{SH} = 40[rad/sec]$ and $\varphi_{SH} = 60°$. The impact of this choice on the sharing dynamic will be discussed later in Sec. 7.5.

The parameters required for the design have been estimated from the experimental set-up with two motors on the same shaft in Fig. 7.1. The magnetizing inductance and the stator resistance of the two motor sections have been measured with the no-load and short-circuit tests. The inertia and the friction of the system have been obtained from the data-sheets and measuring the time constant of the shaft. All the parameters are reported in Table 7.2.

Table 7.2: Estimated machine parameters

Stator Magnetising Inductance $L[H]$ & Resistance $R[\Omega]$	0.257, 3.7
Shaft inertia $J[Nms^2]$ & Friction $F[Nms]$	0.3, 0.09
Machine constant $K_t[Nm/A]$	3.27

7.3 Speed dynamic in equal sharing condition

The first experimental validation has been the implementation of the equivalent collective system in Fig. 6.9, and designed in Section 6.5, without

the compensation loop. The obtained current and sharing controller parameters have been scaled by N according to the discussion in Section 6.5, hence the droop coefficients become $K_{D_1}^{(ES)} = K_{D_2}^{(ES)} = NK_D = 2 \cdot 3.65 = 7.3[(rad/sec)/A]$, whereas $K_{iSH1}^{(ES)} = K_{iSH2}^{(ES)} = K_{iSH}/N = 26/2 = 13$. Fig. 7.3

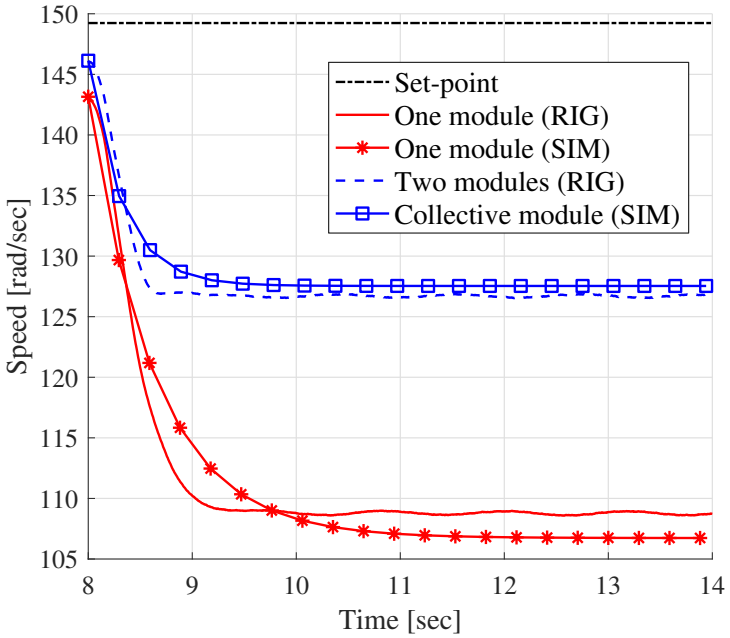

Figure 7.3: Experimental validation of the design control loops for the equivalent collective *not* compensated system from zero to full load step $T_L = 17Nm$

reports experimental (RIG) and simulated (SIM) response of the speed from a zero to a full load step $T_{L_{NOM}} = 17[Nm]$ to verify the response of the real system in the same conditions of the designed and simulated one. The speed reference is $\omega^* = 149.2[rad/sec]$ and the load torque T_L has been attached after 8 seconds. Looking at the figure it is possible to appreciate how the collective simulated module (blue line with squared markers) presents similar dynamics of the two motors in the experiment (dashed blue line). Representing the case of $N = 2$, if one of the module fails, the continuous red line and the one with the asterisk markers are respectively the real and simulated speed of one single motor with scaled values. The steady state values, with

and without T_L, can be verified with (6.7) and (6.12) either. In Fig. 7.4 the speeds under the same conditions of Fig. 7.3, except for the addition of the compensation loop, are reported.

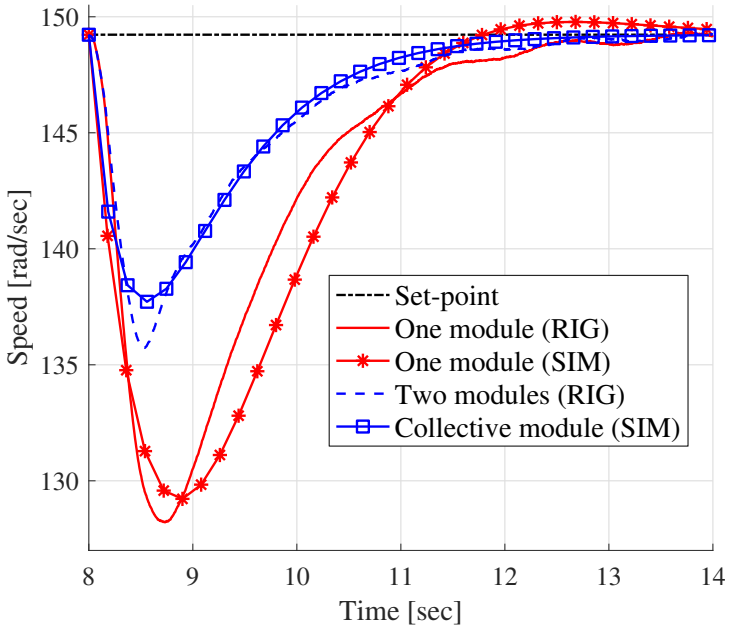

Figure 7.4: Experimental validation of the design control loops for the equivalent collective compensated system from zero to full load step $T_L = 17Nm$

7.4 Current sharing dynamic

The second step of the experimental validation is the implementation and prediction of the current sharing dynamic in response to a change in an external sharing command. In order to do so, the emulated multi-three-phase motor is brought to steady state with equally shared power ($3.06[A]$ per motor) and full load torque $T_{L_{NOM}} = 17[Nm]$. At $t = 8[sec]$ the power sharing is changed to 25% to module 1 and 75% to module 2, i.e. $K_{D1}^{(US)} = K_{D1}^{(ES)}/\xi_1 = 7.3/(2 \cdot 0.25) = 14.6$ and $K_{D2}^{(US)} = K_{D2}^{(ES)}/\xi_2 = 7.3/(2 \cdot 0.75) = 4.86$. Moreover, for keeping constant the droop loop gain, the integral gains

have been scaled accordingly ($K_{iSH1}^{(US)} = K_{iSH1}^{(ES)}\xi_1 = 13 \cdot 2 \cdot 0.75 = 19.5$ and $K_{iSH2}^{(US)} = K_{iSH2}^{(ES)}\xi_2 = 13 \cdot 2 \cdot 0.25 = 6.5$). Fig. 7.5 shows the current sharing

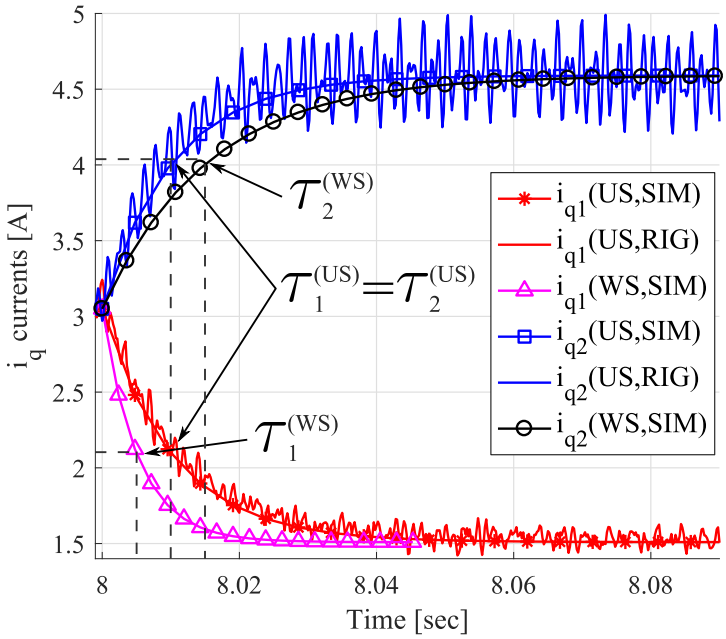

Figure 7.5: Current sharing with $(\tau_1^{(US)}, \tau_2^{(US)})$ and without $(\tau_1^{(WS)}, \tau_2^{(WS)})$ updating the integral gain of the droop loop. Before second 8^{th}, the power is equally split ($3.06A$ per motor). At $t = 8sec$ the power is split with a $75\% - 25\%$ ratio (4.59[A]-1.53[A]).

dynamic. Based on the discussion in Section 6.6, these sharing dynamics can be predicted thanks to (6.22). Looking at the steps at $t = 8[sec]$, the 63% of the relative steps from $i_q = 3.06A$ to the final values ($4.59A$ and $1.53A$) are, in terms of absolute current, $4.02A$ and $2.09A$, respectively. Table 7.3 reports all the values of K_{iSHj}, K_{Dj}, and the relative time constants computed with (6.22) in all the operating conditions: ES (Equal Sharing), US (Unbalanced Sharing), and WS (Wrong Sharing). The calculations are validated for every experiment and simulation in Fig.7.5. As expected, the values of $\tau_1^{(WS)}$ and $\tau_2^{(WS)}$ are different because the sharing loop gain has not been kept constant. This means that the sum of the currents ($i_{qTOT} = i_{q1} + i_{q2}$) is not constant

Table 7.3: Sharing controller parameters and time constants

Operation	$P_{\%j}$	K_{iSj}	K_{Dj}	$\tau_j[sec] - 8sec$	|63% relative step|$[A]$	
ES	50%	13	7.3		3.06	
US	25%	6.5	14.6	$0.01 = \tau_1^{(US)}$	2.09	✓
US	75%	19.5	4.86	$0.01 = \tau_2^{(US)}$	4.02	✓
WS	25%	13	14.6	$0.005 = \tau_1^{(WS)}$	2.09	✗
WS	75%	13	4.86	$0.015 = \tau_2^{(WS)}$	4.02	✗

during the transient, thus the final speed of the shaft is affected as shown in the next subsection.

7.5 Conclusions

By not updating the integral gain of the droop loop, the sharing time constants described by (6.22) are different for the two modules. This difference is reflected in the angular speed of the shaft as highlighted in Fig. 7.6. The fully loaded system $T_L = 17[Nm]$ is brought to steady state with equally shared power, and at $t = 8[sec]$ the sharing ratio has been set to $25\% - 75\%$, exactly like in Fig. 7.5. In this set of experiments, at $t = 9[sec]$ the ratio has been swapped $(75\% - 25\%)$.

Fig. 7.7 shows the same experiment with a different sharing loop bandwidth (in Fig. 7.7 $\omega_{SH} = 120[rad/sec]$, whereas in Fig. 7.6 $\omega_{SH} = 40[rad/sec]$).

Both the experiments have been run updating (red line with diamond markers, US condition) and not updating (continuous blue line, WS condition) the integral gains of the two modules. As long as the ω_{SH} increases, the current sharing dynamics become faster increasing vibrations during the

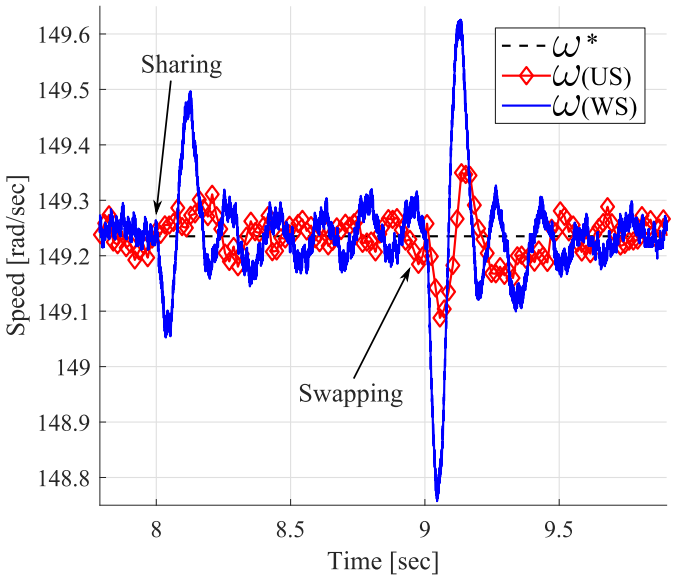

Figure 7.6: The angular speed of the shaft with (US) and with (WS) without updating the integral gains K_{iSHj} with the *slower* sharing set-up ($\omega_{SH} = 40 rad/sec$)

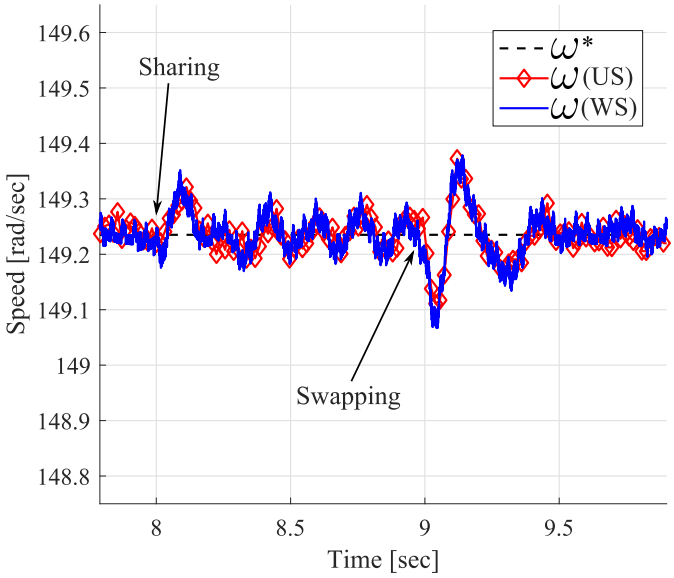

Figure 7.7: The angular speed of the shaft with and without updating the integral gains K_{iSHj} with the *faster* sharing set-up ($\omega_{SH} = 120 rad/sec$)

sharing transient caused by the *quasi-step* torque change.

Assuming both the current (ω_c) and the speed (ω_s) dynamics are designed to be as fast as possible, the sharing dynamic (ω_{SH}) has to be set in between the two: $\omega_s \leq \omega_{SH} \leq \omega_{cq}$. The best trade-off between current harmonic distortion (thus vibration) and speed dynamics is achieved imposing the following condition:

$$\omega_c - \omega_{SH} = \omega_{SH} - \omega_s \tag{7.1}$$

Depending on the particular application, vibrations could be minimised setting $\omega_{SH} \to \omega_s$ affecting more the speed dynamics like in Fig. 7.6, and vice versa, speed dynamics could be kept as much as possible constant setting $\omega_{SH} \to \omega_c$ like in Fig. 7.7, but increasing vibrations with *quasi-step* torque changes.

Chapter 8

Experimental results - Multi-three-phase rig

In this chapter, experimental validation of the novel droop controller introduced in Chapter 6 is provided on a multi-three-phase electrical machine with nine phases at the University of Trieste. Loop designs have been carried on with aid of Table 6.2 using method II for the sharing loops. The chapter concludes with a comparison between the CSR configuration with sharing coefficients and the novel droop controller validating the control design approach in Section 6.5 and equations in Table 6.2.

The experiments have been carried on with the help of Professor Alberto Tessarolo and Professor Roberto Menis. This second set of experiments have been possible thanks to a custom control platform called *uCube* [76], developed with the help of Dr. Giovanni Lo Calzo and Dr. Andrea Formentini.

The droop controller has been further validated on the experimental rig in Fig. 8.1. In Fig. 8.1a, bottom left, it is possible to notice the custom control board used in this set of experiments. The control platform has been

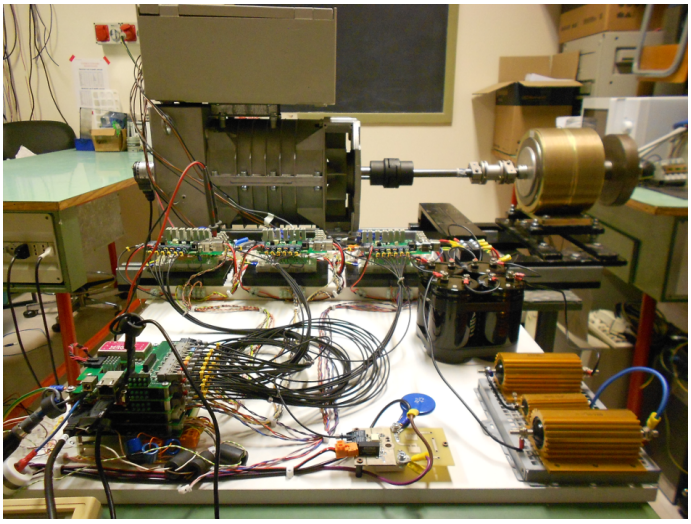

(a) Configurable multi-three-phase motor coupled to the break.

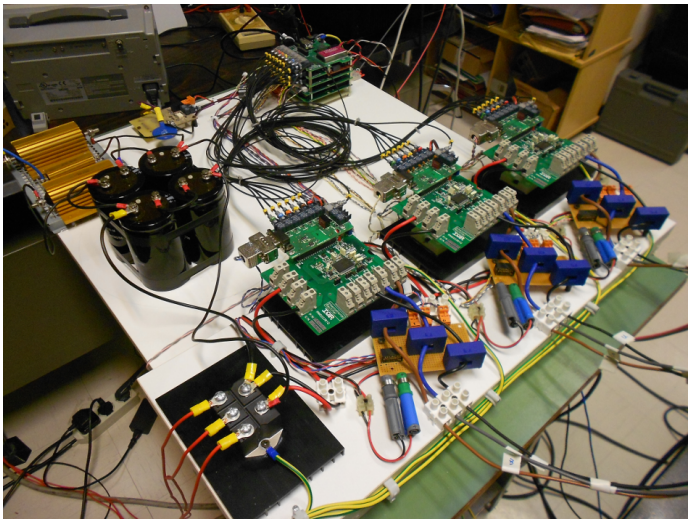

(b) Three converters with nine current sensors, diode rectifier, and DC-link capacitors.

Figure 8.1: Two different views of the multi-three-phase motor rig.

called *uCube* [76] and it has been developed as general as possible to carry on research on a wide range of power electronics systems (i.e. multi-level converters, matrix converters, motor control, etc.).

In the following subsection, a brief introduction regarding the *uCube* will be given.

8.1 uCube

The *uCube* has been developed at the PEMC Group, University of Nottingham, by Giovanni Lo Calzo, Andrea Formentini, and Alessandro Galassini. It

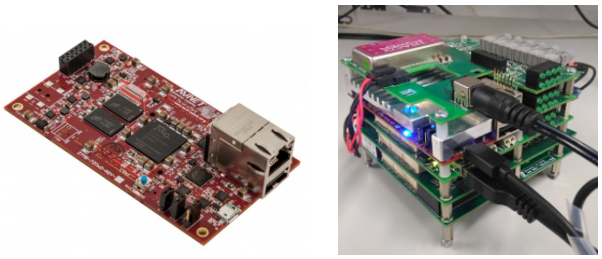

(a) Microzed. (b) *uCube* assembly.

Figure 8.2: The Avnet Microzed board (a) and the uCube control board (b).

is based on the off-the-shelf Microzed board [77] from Avnet (Fig.8.2a), a low-cost development board based on the Xilinx Zynq-7000 All Programmable SoC. The Zynq is a heterogeneous SoC [78] integrating in a single device a dual-core ARM Cortex-A9 based Processing System (PS) and a Field Programmable Gate Array (FPGA) Programmable Logic (PL) [79, 80].

In not heterogeneous systems, where a separate Micro Controller Unit (MCU), or a Digital Signal Processor (DSP), is used in conjunction with a FPGA device, it often happens that the data communication between these two entities represents a serious bottleneck in terms of performance. In fact, in presence of an external communication bus between the two packages, the data clock frequency has to be limited in the range of few tens of mega-hertz.

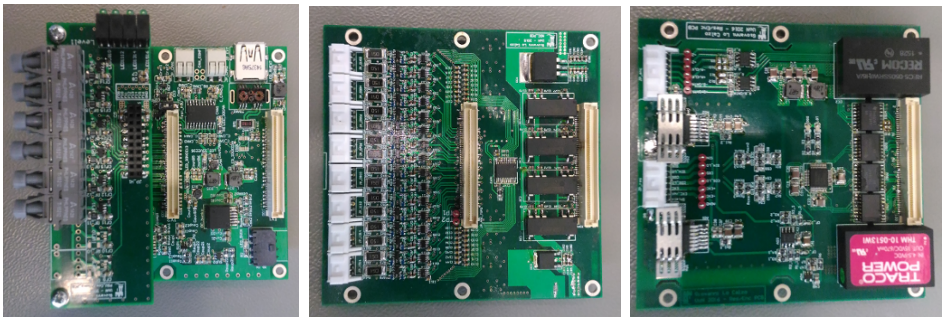

(a) Fibre optics. (b) ADC. (c) Encoder/Resolver.

Figure 8.3: (a) Main expansion board. (b) Analogue-to-Digital Converters expansion board. (c) Resolver and Incremental/Absolute Encoder board.

The SoC Zynq family provides on-chip, high bandwidth (up to 150 MHz), low latency AXI interfaces to connect PS and PL and the possibility for the FPGA to direct access system memory for very fast data transfers.

The core concept at the basis of the *uCube* design is to exploit the power of the dual-core ARM PS to execute complex control algorithms and the programming flexibility of the FPGA to design custom made peripherals to interface the control board with the outer world. In order to fully take advantage of the before mentioned flexibility, three expansion boards (Fig. 8.3) have been designed to allow the PL to be electrically interfaced with sensors and transceivers. The first expansion board hosts 24 fibre optics channels, the second board hosts 16 Analogue-to-Digital-Converters (ADC), the third board is instead oriented to motor controlling applications and provides for a sin-cos resolver interface and absolute/incremental encoder interface. System configuration and software architecture are based on the XAPP1078 application note from Xilinx [81] where the CPU0 is running Petalinux - a GNU/Linux OS baked by Xilinx. Signals coming from and directed to the expansion boards are routed to the FPGA circuitry. Once stored in the form of digital data, they will be used by the two ARM cores to execute the real time control algorithm, also referred at as bare-metal

application running on CPU1, and for data exchange with a PC running a specifically designed Matlab Graphical User Interface (GUI).

8.1.1 Software architecture

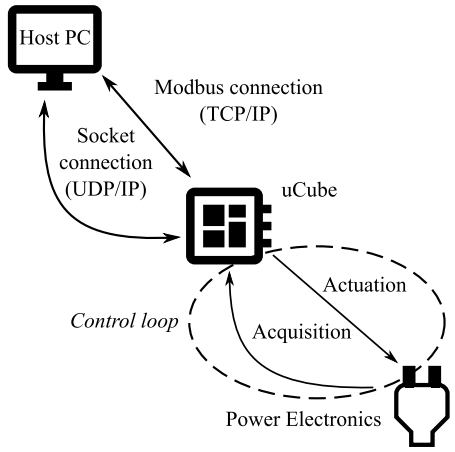

(a) High level connection layout.

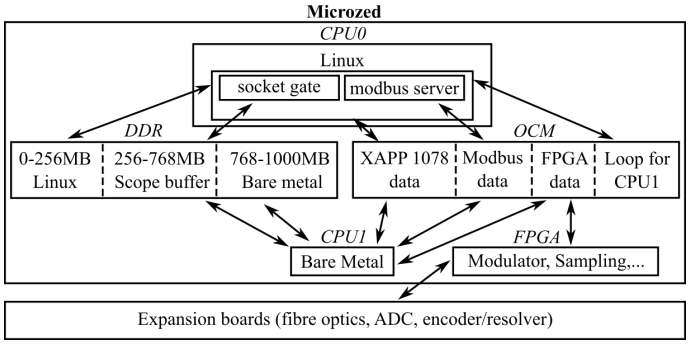

(b) Software architecure.

Figure 8.4: The Host PC in Fig. 8.4a is used for setting control parameters, on/off flags, set-points and for saving and eventually plotting acquired data and derived variables. The *uCube* software architecure in Fig.8.4b has been derived by the XAPP1078 application note from Xilinx.

In the proposed *uCube* control platform, the full flexibility and potential of the Zynq SoC have been obtained by coding specific software for

each entity available in the SoC (CPU0, CPU1, and FPGA), as depicted in Fig.8.4b. Data exchange has been achieved sharing On-Chip Memory (OCM) and Double Data Rate Synchronous Dynamic Random Access Memory (DDR SDRAM). All the hardware elements detailed in the previous section have been physically connected to the FPGA pins and custom software modules have been implemented for each expansion board. On the CPU1, real time bare metal code (or firmware) implementing the control algorithm scheme for the connected power electronics converter(s) is executed (Fig.8.4a). During start-up operation, Linux is loaded on CPU0. While supervising the whole system, Linux is in charge of handling Host PC communication (Fig.8.4a). Acquired data, parameter and set-point input forms are presented to the final user thanks to a Matlab Graphical-User-Interface (GUI) shown in Fig. 8.5. In the next subsections, software components and core interactions will be described in detail.

FPGA

In the current control board version, three three-phase modulators have been coded in the PL, featuring independently configurable switching frequencies and dead-times. Each modulator uses 7 fibre optics channels to control the inverter gate drives (six legs and a possible braking leg). The remaining 3 channels are configured as independent fault inputs.

The FPGA also implements a trip mechanism to protect the system under unwanted and potentially harmful operating system conditions. Every value acquired from each ADC channel is continuously compared against a low and a high, PS configurable, threshold. If the received value exceeds one of these two thresholds, a fault is asserted, the PWM units turned off and all the outputs brought to the off state with a delay of less then one microsecond. This time is usually sufficient to protect the power electronics converter(s) even in case of shot-through fault.

Bare metal

The real-time bare metal C code runs in CPU1. It is executed at each sample time and it usually implements the core control algorithms. A complete function library has been developed to handle the communication with the PL and speed-up the coding. It also includes a scope functionality: a configurable number of system variables can be recorded every sample time (or its multiple in down-sampling mode) and stored in memory. Thanks to the high dimension RAM available on the Microzed and the high bandwidth communications described in the next sub-section, the scope system allows an high number of signals and variables to be monitored, simplifying considerably the debugging process.

Linux

The main Linux tasks are the following:

- Starting and stopping the bare metal application;
- Checking if the bare metal is running or not;
- Printing redirected output bare metal *printf* function;
- Forwarding modbus data from the Host PC to the bare metal application (and vice-versa) through the OCM thanks to the modbus server (Fig. 8.4a and 8.4b);
- Serving UDP/IP socket connection for downloading the scope buffer within DDR memory through the *socket gate* user space process (Fig. 8.4a and 8.4b).

Linux constantly monitors the bare metal execution and it shares information with the host PC. Furthermore, it allows bare metal *printf* output function redirection thanks to a Linux user space process called *softuart*.

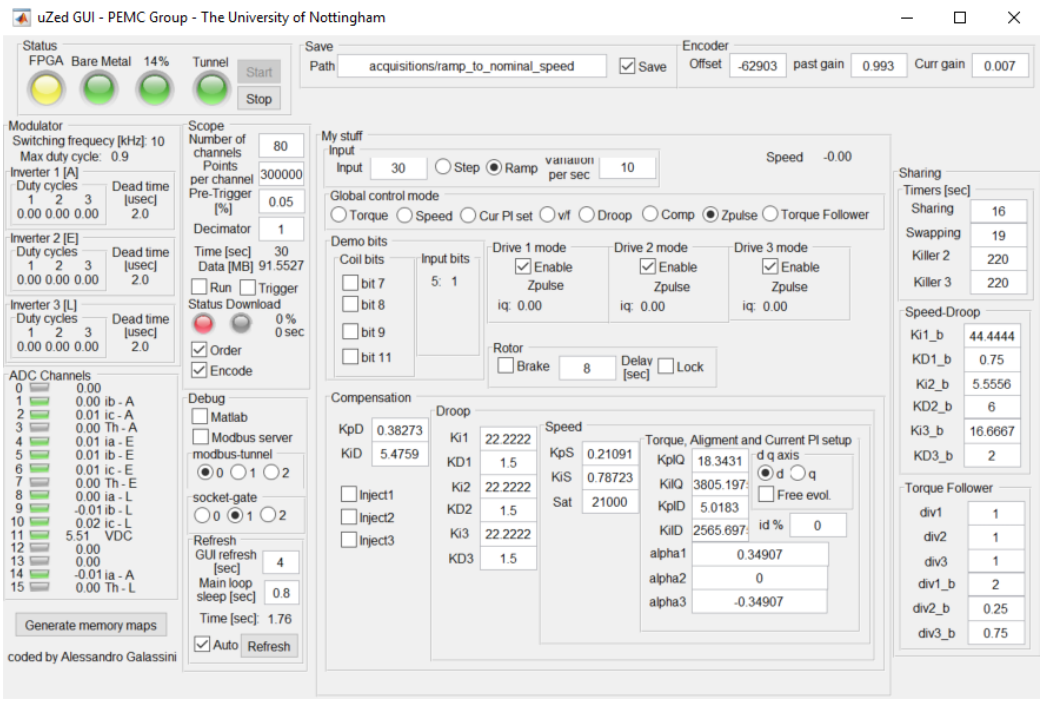

Figure 8.5: Bare metal, hardware, and scope buffer status together with set-point, parameter, and flag input forms are shown to the final user on a Matlab GUI.

This redirection is needed because the UART peripheral is kept busy by the Linux shell.

Set-points, on/off flags, control parameters, etc., are set by a Matlab GUI (Fig. 8.5) running on the Host PC thanks to a Modbus connection (Fig. 8.4a)[82]. Modbus is currently implemented using TCP/IP over Ethernet or asynchronous serial transmission over a variety of media (EIA/TIA-232-E, EIA-422, EIA/TIA-485-A, etc.). Two physical links have been set-up: the 10/100/1000 Ethernet port and the USB Host 2.0 port thanks to the Remote Network Driver Interface Specification (RNDIS) present in Linux kernel. The modbus server running on Linux has been coded linking against the open-source *libmodbus C* library [83].

Once the bare metal scope routine is triggered and the acquisition is

done, the *socket gate* Linux process starts serving recorded data into the scope buffer within DDR memory through UDP/IP socket (Fig.8.4).

Host PC

On the Host PC, the modbus client has been embedded into a *C* daemon process (called modbus tunnel) forwarding information between the modbus client and a local socket (and vice-versa).

In this way, the so called modbus tunnel allows the *uCube* to be queried with any programming language with local socket support. In order to present many different information to the final user, a Matlab GUI interface has been created (Fig. 8.5).

Whilst only few kilo-Bytes can be addressed by the Modbus protocol, 512MB DDR memory have been assigned to the scope buffer where real time data and derived variables can be saved. Firstly, once the acquisition is done, data are transferred from DDR to the Host PC through the Ethernet or the USB Host 2.0 (3.5MB/sec) port. Secondly, data are saved and eventually processed and plotted by a custom Matlab script coded by the final user. Furthermore, after every acquisition, modbus data are dumped and saved into a *.pdf* file automatically generated on the host PC.

8.2 Rig set-up

The multi-three-phase prototype motor in Fig. 8.1a is a two poles synchronous generator obtained from the SINCRO GS140 05 001 COD 2FF514001 from Soga Energy Team. Thanks to the junction box on top, it can be configured with different number of sets of windings (1,2,3,4). In this experimental set, the machine has been configured with a triple star, therefore $N = 3$ and $n = 9$. The brake coupled to the motor in Fig. 8.1a is an hysteresis brake from Magtrol. The machine has been wired to three converters shown in the same figure. They have been obtained combining the FP25R12KE3 power

module from Infineon with the IRMD22381Q demo board for the relative IR22381Q gate drive, both from IOR.

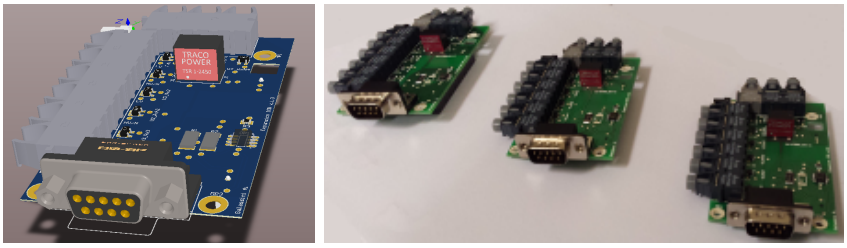

(a) PCB Altium design. (b) Software architecture.

Figure 8.6: Three custom PCB interfaces for fibre optic links and ADCs.

Every demo board has been connected thanks to a custom Printed Circuit Board (PCB) interface. All the converters were controlled by the *uCube*, previously discussed in section 8.1. Even if the drive is unique, in order to emulate the condition where the modules are completely independent, control loops for the three modules have been written independently without common information except for the speed signal from the incremental encoder EL-ER72A/B from Eltra.

DC link voltage and switching frequency have been set up to 350$[V]$ and 10$[kHz]$, respectively. Input parameters are shown in Table 8.1. In Table 8.2, electrical and mechanical machine parameters are reported.

Table 8.1: Input parameters

Stepped speed set-point	18$[rad/sec]$
Ramped speed set-point	30$[rad/sec]$
Rotor field DC current	1.58$[A]$
Breaking torque	55.2$[Nm]$

Table 8.2: Machine parameters

First harmonic stator inductance $d_1[H]$	171.5×10^{-3}
First harmonic stator inductance $q_1[H]$	120.2×10^{-3}
Stator resistance $r_s[\Omega]$	9.1
Machine constant $K_t[Nm/A]$	3.06
Shaft inertia $J[Nms^2]$	380×10^{-3}
Friction $F[Nms]$	140×10^{-3}

8.3 Current loops design

Considering the plant in (3.23) and shown in Fig. 3.5, current loops have been designed with aid of equations (3.20) and (3.21) imposing the following bandwidth and phase margins: $\omega_{cd} = \omega_{cq} = 211[rad/s]$ and $\varphi_{cd} = \varphi_{cq} = 65°$. In Fig. 8.7, current step responses on d and q axes in locked rotor condition are shown.

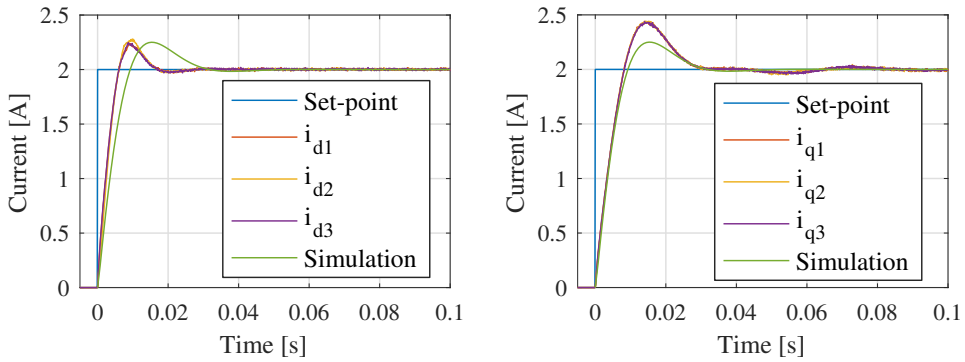

(a) d-axis step (2A). (b) q-axis step (2A).

Figure 8.7: d-current and q-current loops design validation.

8.4 Speed loop design

The speed regulator has been designed using (3.20) and (3.21) considering the plant in (4.3), and shown in Fig. 4.4, imposing the following bandwidth and phase margin: $\omega_s = 6[rad/s]$ and $\varphi_s = 60°$. Speed step response and

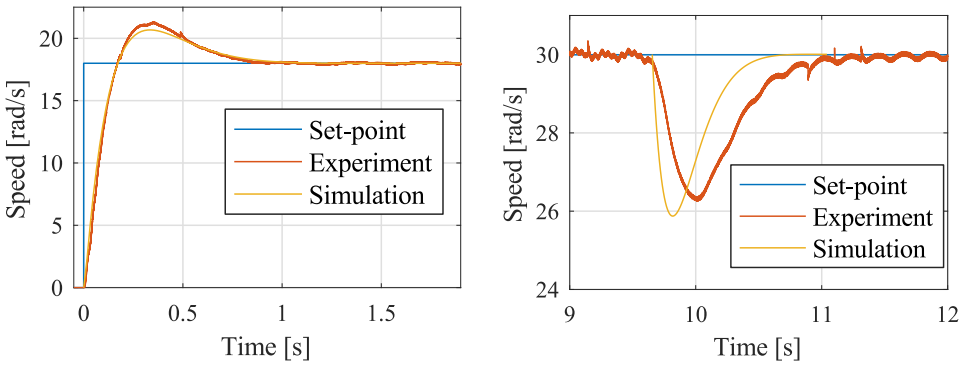

(a) Speed step (18rad/s) in CSR.

(b) Speed variation with load step in CSR.

Figure 8.8: d-current and q-current loops design validation.

speed variation with load step from zero to full load $T_L = 55.2Nm$ with all the drives in speed mode (CSR configuration) are shown in Fig. 8.8a and 8.8b, respectively.

8.4.1 Common Speed Reference - Torque Follower comparison

Equivalence between CSR and TF configuration previously introduced in Section 4.3 is here experimentally validated. Currents under load transient, both in CSR and TF configuration, are shown in Fig. 8.9. For clarity's sake, only four out eighteen currents have been highlighted. The shift of an angle $2\alpha = 2\pi/9$ between i_{a1} and i_{a3} is highlighted. Since the two configurations are equivalent and the machine has been started with the rotor aligned to

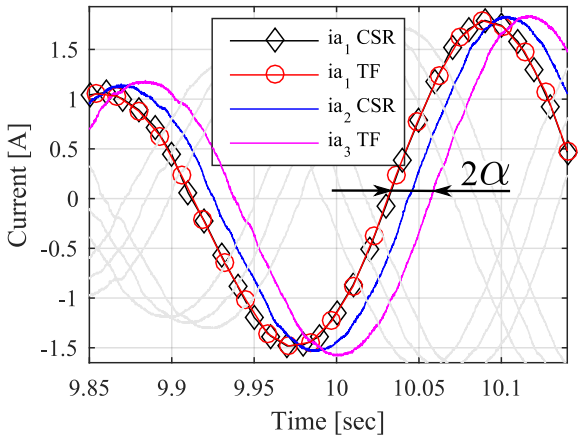

Figure 8.9: Current comparison under load transient

the same position, same currents from different configurations are matching (i.e. $i_{a1}CSR$ with $i_{a1}TF$). Equivalence between the CSR and the TF configuration is further confirmed by the output speeds shown in Fig. 8.10.

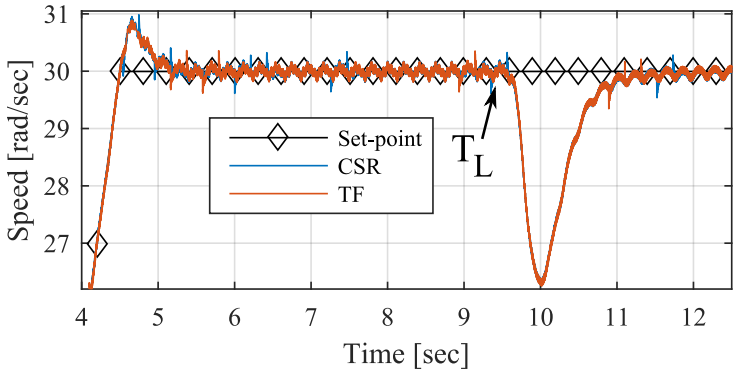

Figure 8.10: During start-up and load transient operations, output speeds in CSR and TF configuration are the same.

8.4.2 Post-fault compensation strategy

Open circuit condition has been validated disconnecting the third converter. Assuming constant current bandwidth without updating the current PI gains, nominal speed dynamic is guaranteed by (5.8). In Fig. 8.11, faulty

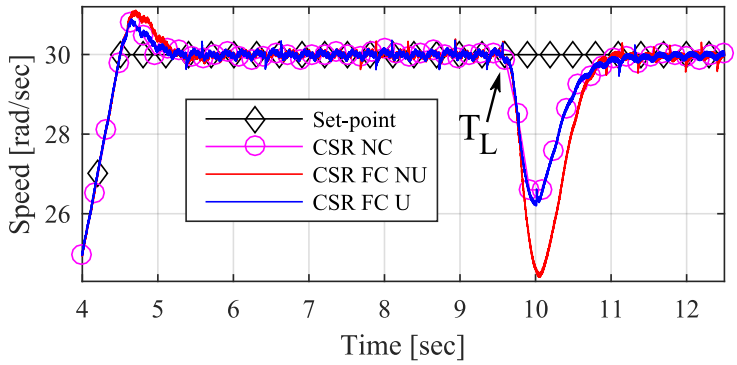

Figure 8.11: In nominal condition $W_{1NC} = W_{2NC} = W_{3NC} = 1$, whilst in fault condition with updated loop gains $W_{1FC} = W_{2FC} = 1.5$.

output speeds updating (FC U) and not updating (FC NU) the loop gains W_j are compared against the CSR output speed in nominal condition (NC). Looking at the figure, (5.8) clearly guarantees constant speed dynamics during both start-up and load transient regulation. Assuming constant current bandwidths ω_{cd} and ω_{cq}, elements in (2.33) are considered constant. In general this is not true, but in this particular case the difference is negligible. In Fig. 8.12, i_{q2} currents in nominal and fault conditions are shown. If in nominal condition there are $6A$ flowing within the machine, $2[A]$ per set, in fault condition constant power is guaranteed with $3[A]$ per set.

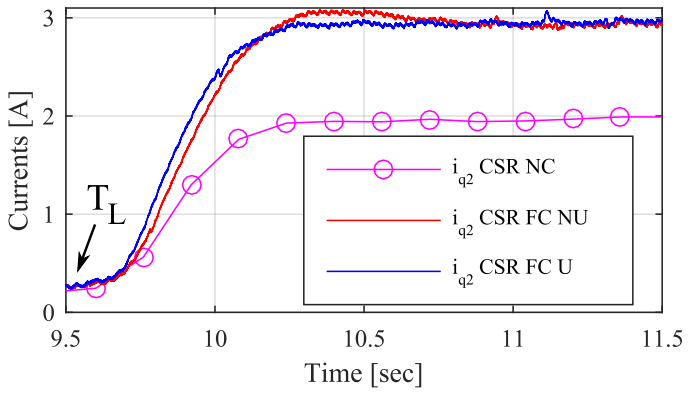

Figure 8.12: Defining I_T the total current within the motor, in NC $N_A = 3$ and $I_T = (2 \cdot N_A) = 6A$, whereas in FC $N_A = 2$ and $I_T = (3 \cdot N_A) = 6A$.

8.5 Power sharing

In this section, power sharing with sharing coefficients is given and further compared against the novel speed-drooped controller. Control schematic of the CSR configuration with *sharing coefficients* is shown in Fig. 8.13. Referring to the coefficients in Table 5.1, in Fig. 8.14a, constant rotor speed

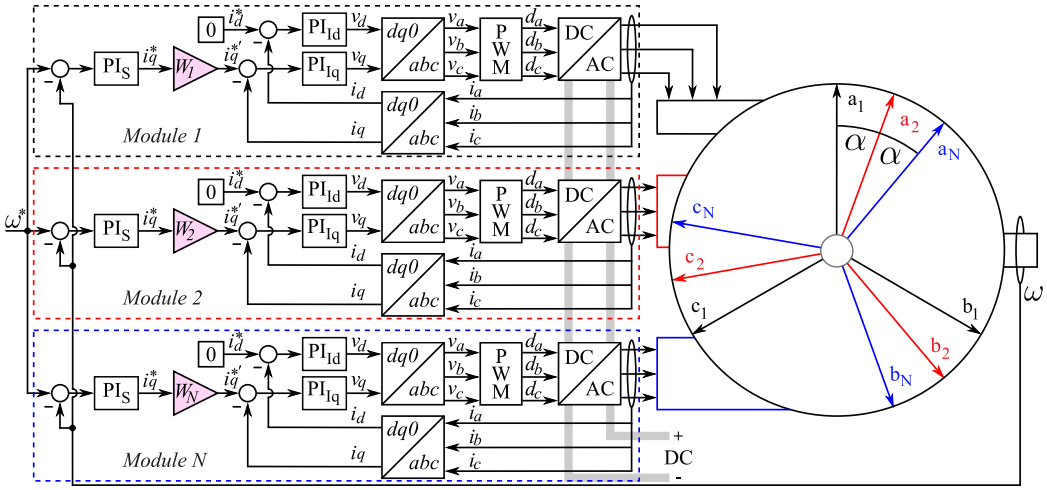

Figure 8.13: Common Speed Reference (CSR) control schematic for speed control with load sharing capabilities implemented within the *uCube*. Sharing gains $W_{1,2,3}$ are highlighted in magenta. The speed filter has been omitted.

under load sharing transients in Fig. 8.14b is highlighted. Unlike in Table 5.1, power sharing has been done after 17.5$[s]$ and coefficients have been swapped after 20.5$[s]$. In Fig. 8.15a, phase currents while swapping the first power ratio with the second one are shown. Signals within the dotted circle are zoomed in Fig. 8.15b. Due to the presence of mutual electromagnetic couplings among different sets of windings, currents of the third set of windings are affected by current transients within the other two sets of windings (for sake of clarity only i_a currents are shown). Controlled current transients during load sharing operations can be achieved with the speed-drooped control strategy validated in section 8.6.

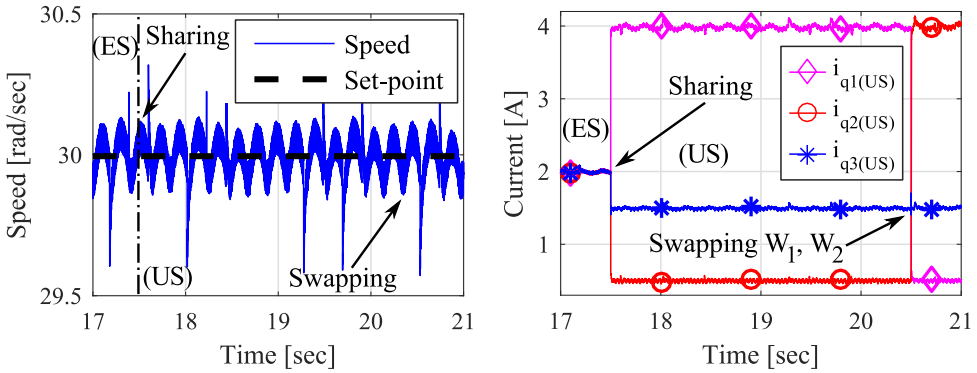

(a) Speed is not affected. (b) i_q currents under US conditions.

Figure 8.14: In Fig. 8.14a, constant speed during sharing and swapping W_1 with W_2 is highlighted. In Fig. 8.14b, i_q current transients not affecting the speed in Fig. 8.14a are highlighted.

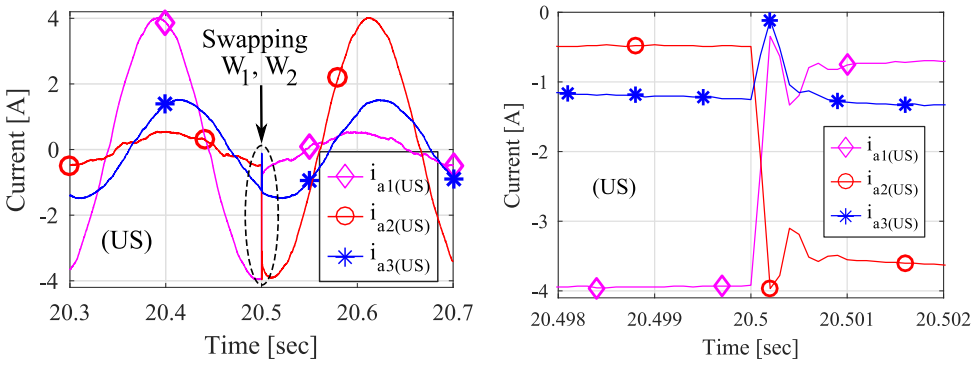

(a) Phase current transients. (b) i_{a3} is affected by the other sets.

Figure 8.15: In Fig. 8.15a, phase current transients during swapping W_1 with W_2 are shown. Signals within the dotted circle are zoomed in Fig. 8.15b. Even if W_3 is constant, i_{a3} is not constant due to the mutual electrical coupling.

8.6 Speed-Drooped controller

Referring to Fig. 6.3, the Speed-Drooped controller has been implemented on the *uCube* like in Fig. 8.16. The inner current loop has been designed

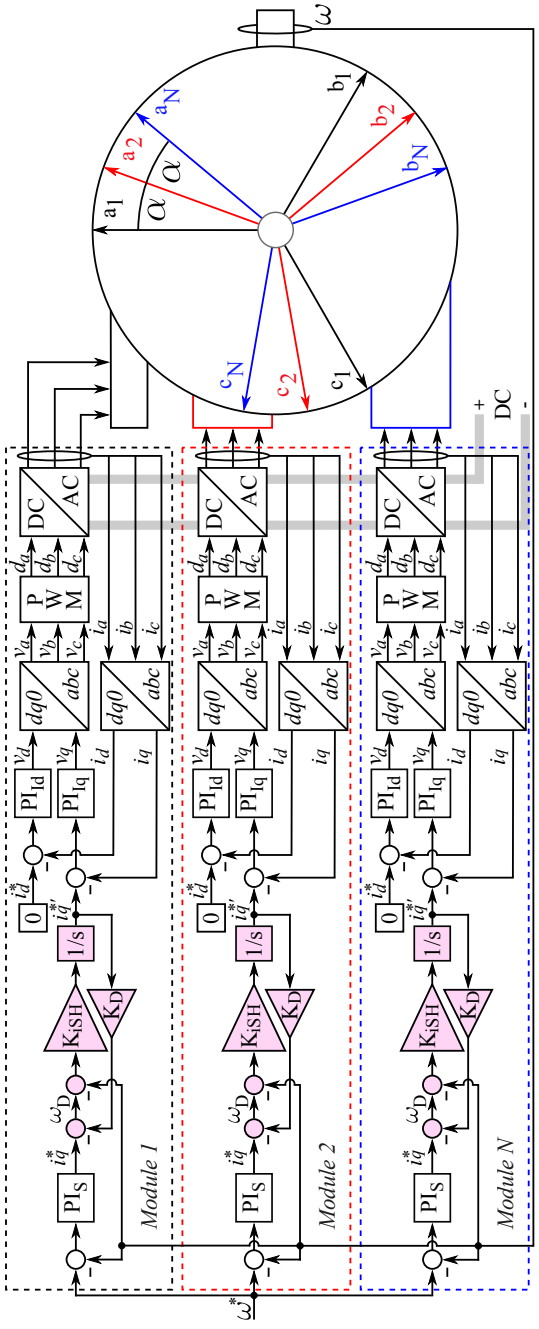

Figure 8.16: Droop controller implementation. Speed filter has been omitted. Droop controllers are in magenta.

like in Section 8.3. The droop loop, or sharing loop, has been designed with method II from Table 6.2 with different sharing time constant $\tau_{sharing}$ in order to demonstrate how the proposed strategy is able to control current sharing dynamics. Looking at the droop plane in Fig. 6.1b, the collective droop gain coefficient can be obtained imposing the maximum speed drop with (6.12). The maximum speed drop would be the steady state output speed of the system without the PI_S in nominal condition. In this particular case, the maximum delta has been set up equal to the 10% of the ramped reference speed ($\Delta\omega_{max} = 3[rad/s]$). Considering a total nominal current of $6[A]$, the collective droop coefficient $K_D^{(ES)} = \Delta\omega_{max}/(\sum_j^N I_{nom,j}) = 0.5[(rad/s)/A]$ has been computed. Therefore, $K_{Dj}^{(ES)} = NK_D^{(ES)} = 1.5[(rad/s)/A]$. The integral gain $K_{iSH}^{(ES)} = 1/(K_D^{(ES)}\tau_{sharing})$ has been computed for $\tau_{sharing} = 1[ms]$ and $\tau_{sharing} = 30[ms]$ leading to $K_{iSH}^{(ES)} = 2000$ and $K_{iSH}^{(ES)} = 66.\bar{6}$, respectively. The integral gains per module have been obtained dividing $K_{iSH}^{(ES)}$ by N ($K_{iSH}^{(ES)} = 2000/N = 666.\bar{6}$ and $K_{iSH}^{(ES)} = 66.\bar{6}/N = 22.\bar{2}$). Stability of $G_{SH_{OL}}$ and inequality $(\omega_s = 6[rad/s]) < \omega_{SH} \leq (\omega_c = 211[rad/s])$ have been verified for both sharing time constants. Phase margin φ_{SH}, gain margin G_{mSH}, and cross-over frequency ω_{SH} are reported in Table 8.3.

Finally, dividing the droop gain and multiplying the integral gain by the same factor $\xi_j = NP_j$ (for $P_j = 2/3, 1/12, 1/4$) power unbalancing has been obtained. Both the droop and the integral gain per each module for $\tau_{sharing} = 1[ms]$ and $\tau_{sharing} = 30[ms]$ are summarised in Table 8.3.

Table 8.3: Droop controller parameters

$\tau_{sharing} = 1[ms]$ ($\varphi_{SH} = 75.1[deg]$, $\omega_{SH} = 47.2[rad/s]$, $G_{mSH} = 27.9[dB]$) ✓					$\tau_{sharing} = 30[ms]$ ($\varphi_{SH} = 36.6[deg]$, $\omega_{SH} = 33.6[rad/s]$, $G_{mSH} = 14.2[dB]$) ✓				
j	P_j	Current	K_{Dj}	K_{iShj}	j	P_j	Current	K_{Dj}	K_{iShj}
$1,2,3(ES)$	$1/3(ES)$	2	$1.5(ES)$	$666.\bar{6}(ES)$	$1,2,3(ES)$	$1/3(ES)$	2	$1.5(ES)$	$22.\bar{2}(ES)$
1	2/3	4	0.75	1333.3	1	2/3	4	0.75	44.4
2	1/12	0.5	6	166.6	2	1/12	0.5	6	5.5
3	1/4	1.5	2	500	3	1/4	1.5	2	16.6

8.6.1 Droop loop

Fig. 8.17a and 8.17b show the speed step response and the speed variation with load step without compensation loop like discussed in section 6.2. In this particular case the sharing time constant has been set to $30ms$. In Fig. 8.17b, it is possible to appreciate how the speed drop increases with T_L.

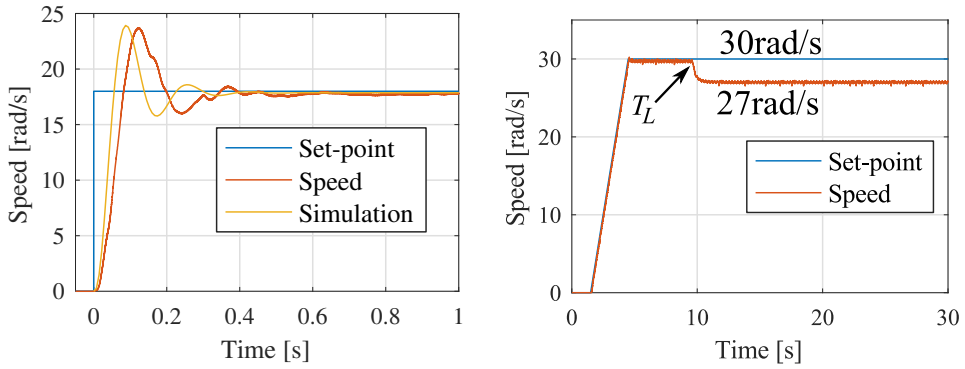

(a) Speed step (18rad/s) without PI_S.

(b) At full load $\Delta\omega_{max} = 3rad/s$.

Figure 8.17: Speed dynamics as in Fig. 6.3 but without compensation PI_S.

8.6.2 Compensation loop

The outer speed regulator has been designed imposing the same bandwidth and phase margin used for the CSR configuration in Sec. 8.4: $\omega_s = 6[rad/s]$ and $\varphi_s = 60°$. However, instead of considering plant G_S in (4.3), the design has been done on plant $G_{SH_{CL}}$ in (6.16) taking into account the sharing dynamics regulators like explained in section 6.5. In Fig 8.18, the speed step response with system configured like in Fig. 6.3 with $\tau_{sharing} = 30[ms]$ is shown.

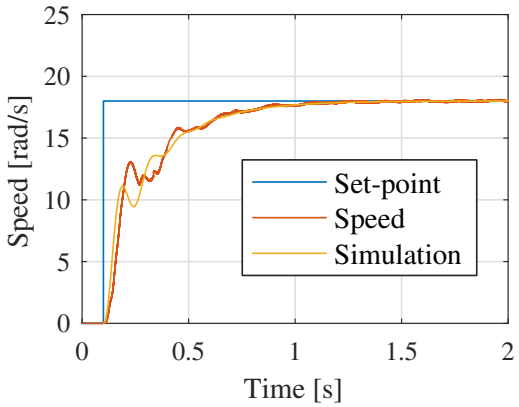

Figure 8.18: Speed step (18rad/s).

8.6.3 Power sharing with droop controller

Looking at Fig. 8.19, the i_q currents under ramped input from zero to nominal speed are shown. After $10s$ the brake have been enabled. The system was in (ES) condition until second 17.5. At that point, the droop and the integral coefficients have been programmed for unbalanced sharing like reported in Table 8.3. In Fig. 8.20, the difference between power sharing achieved with sharing coefficients like in Fig. 8.14b and power sharing achieved with the droop controller like in Fig. 8.19 is highlighted. Whilst current set-point step change leads to current distortion and could potentially excite mechanical resonances, droop controlled transients smoothly reach the steady state

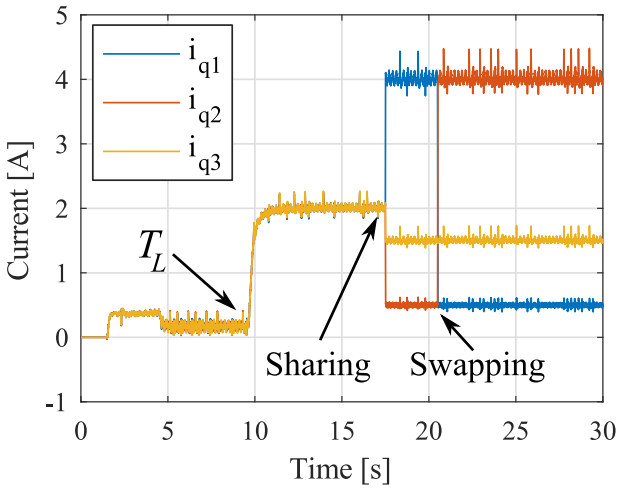

Figure 8.19: Power sharing with $\tau = 1ms$. Sharing and swapping operation are highlighted.

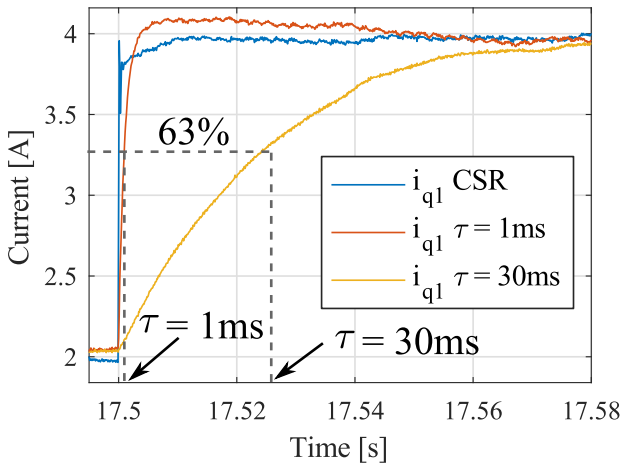

Figure 8.20: Sharing time constants comparison.

with predicted time constants reported in Table 8.3. In Fig. 8.21, unaffected speed dynamics under power sharing transient for different time constant are shown.

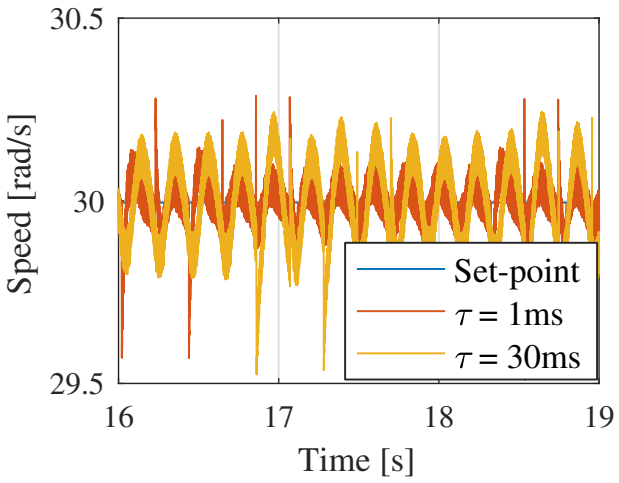

Figure 8.21: Speed dynamics under different sharing time constants.

8.7 Conclusions

In this section, for comparison's sake, phase currents during swapping transient from the system configured in CSR and in Speed-Droop mode are compared.

In Fig. 8.22, speed-drooped phase currents during swapping operation with $\tau = 1ms$ (dashed lines) are compared against common speed reference ones (continuous lines). For simplicity, only phases a of each module are shown. Clearly, the positive impact of the novel controller while swapping the first power ratio with the second one can be appreciated within the red circle at second 20.5. In-fact, looking at a currents of the third module in blue, when the system is configured in CSR (continuous blue line with asterisk), the current presents a steep spike. Contrarily, when the system is configured in speed-drooped mode (dashed blue line with asterisk), the current does not presents any spike like highlighted by the red circle. The same phase currents with $\tau = 30ms$ are shown in Fig. 8.23.

Looking at both figures, it is clear how increasing the time sharing constant, and therefore the sharing bandwidth ω_{SH}, the current harmonic dis-

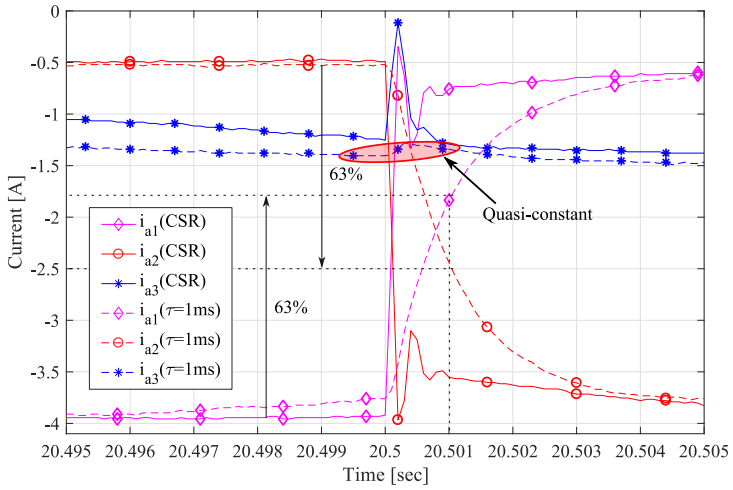

Figure 8.22: Common speed reference versus speed-drooped phase currents with $\tau = 1ms$ under swapping operation.

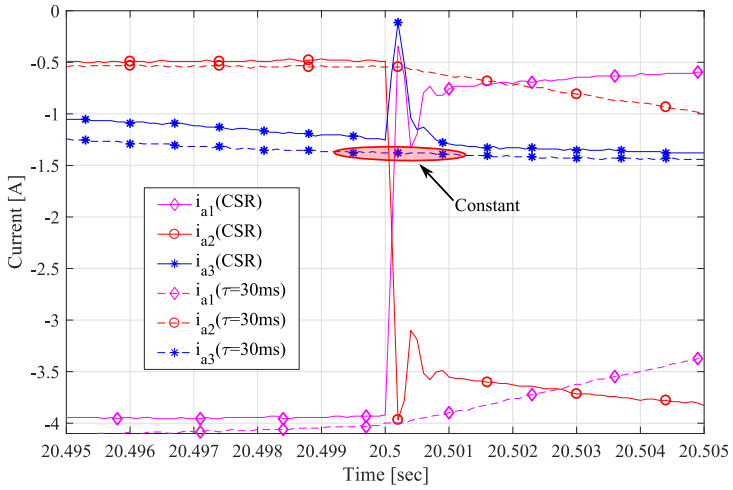

Figure 8.23: Common speed reference versus speed-drooped phase currents with $\tau = 30ms$ under swapping operation.

tortion decreases.

Chapter 9

Conclusions

The undertaken work summarised in this thesis has led to the development of the novel speed-droop controller for modular multi-three-phase systems. The novel control strategy allows the power among different modules to be shared, keeping constant the speed of the shaft at the same time. Every module has been assumed to be made of one three-phase set of windings, one three-phase Voltage Source Inverter, and one Field Oriented Controller. Furthermore, every module has been assumed to be electrically and logically isolated from each other. In other words, the neutral points have been assumed disconnected and only the three local currents (a, b, c) have been assumed to be fed back to each relative controller.

During the preliminary stages, the droop controller has been derived from the power system field where many generation plants are able to supply different amount of power to the grid, and then the droop controller has been translated for motor control application. Firstly, the control design procedure has been developed, secondly, it has been validated on a multi-three-phase rig with two induction motors on the same shaft with rigid couplings. However, due to the presence of different stators on the same shaft, the relative reference frames of different machines are not coupled.

During the middle stages of the PhD, the Vector Space Decomposition

technique for de-coupling the reference frames of a multi-three-phase machine supplied by a balanced voltage source has been studied. Thanks to it, the first $d-q$ harmonic inductances needed for designing the current control loops have been computed. At the same time, a new control platform based on the off-the-shelf Microzed board has been developed in order to control a triple star two poles synchronous generator. Hardware and software co-design took a big effort to develop and test the expansion boards together with the software for the two ARM processors and the firmware for the FPGA. The overall system named *uCube* has been implemented thanks to the help of Dr. Andrea Formentini and Dr. Giovanni Lo Calzo from the Power Electronics Machine and Control Group.

The last stage of the work has seen the validation of the proposed speed-droop control strategy on a triple star two poles synchronous machine. Firstly, current control loops design has been validated on the aforementioned first harmonic inductances taking into account all the mutual electro-magnetic couplings within the machine. Secondly, the speed-droop controller design has been validated. Lastly, the droop control has been compared against the common speed reference and the torque follower control configurations. Last but not least, the capability of the novel speed-droop regulator to control power sharing transients among different drives connected to the same multi-three-phase motor has been proved and demonstrated.

9.1 Summary of achievements and scientific contributions

The achievements and contributions of the presented work are following:

1. The review of multi-three-phase motors for Integrated Modular Motor Drives (IMMD).

2. The review of some possible applications enabled by the modular multi-three-phase motors.

3. The review of multi-three-phase motor modelling within the rotating reference frame and the review of the Vector Space Decomposition for split-phase winding arrangements.

4. The design of current control loops for modular multi-three-phase motors by means of analytical equations, Matlab/Simulink simulations, and experiments.

5. The design of speed control loops for modular multi-three-phase motors by means of analytical equations, Matlab/Simulink simulations, and experiments.

6. The comparison between the Common Speed Reference and the Torque Follower configuration by mean of Matlab/Simulink simulations and experiments.

7. The novel speed-drooped controller is proposed. Analytical design based on provided equations is validated by means of Matlab/Simulink simulations.

8. The experimental evaluation of the novel speed-drooped controller on a multi-drive system with two induction motors on the same shaft and on a triple-star two poles synchronous generator.

9. The comparison between the proposed speed-drooped controller and the Common Speed Reference configuration during power sharing transients.

The list of the papers published based on the achievements presented in this thesis is given in sub-section 1.6.2.

9.2 Possible future works and investigations

The presented work has shown the feasibility of the speed-drooped controller in multi-three-phase applications, and current harmonic distortion reduction during power sharing transients has been proven. The followings are some of the further investigations and works that could be carried on:

- The self-adaptive droop coefficients like in [67] to avoid any inter-module communication or any super-visor controller;
- Identification of the most common faults in multi-three-phase systems and their reduction to a minimal set of faulty states (i.e.: three phases in open circuit, three phases in short circuit, etc. etc.);
- The post-fault compensation strategies for keeping constant the current control loops bandwidth ω_c in case of well known faulty state (i.e.: three phases in open circuit, three phases in short circuit, etc. etc.).
- The Sensor-less control for getting rid of the speed sensor. In-fact, at the moment in case of speed sensor fault, the system is compromised;
- The inter-module communication injecting high frequency signals exploiting the electro-magnetic reference frame couplings;
- The realisation of an Integrated Modular Motor Drive prototype with post-fault compensation capabilities;
- The machine design optimized for reducing the electro-magnetic couplings among different sets of windings.

Bibliography

[1] P. V. McMahon, "Electric locomotives in practice, and tractive resistance in tunnels, with notes on electric locomotive design," *Electrical Engineers, Journal of the Institution of*, vol. 28, no. 141, pp. 508–607, August 1899.

[2] R. B. Matthews, "Electric ploughing," *Electrical Engineers, Journal of the Institution of*, vol. 66, no. 383, pp. 1180–1190, November 1928.

[3] J. Bardeen and W. H. Brattain, "Physical principles involved in transistor action," *The Bell System Technical Journal*, vol. 28, no. 2, pp. 239–277, April 1949.

[4] C. J. Cowie, "Variable frequency drive (cover removed)," Wikipedia, January 2006.

[5] A. M. Wright, "Electrification of railways," *Electrical Engineers, Journal of the Institution of*, vol. 77, no. 468, pp. 826–844, December 1935.

[6] B. Sarlioglu and C. T. Morris, "More electric aircraft: Review, challenges, and opportunities for commercial transport aircraft," *IEEE Transactions on Transportation Electrification*, vol. 1, no. 1, pp. 54–64, June 2015.

[7] A. Eid, H. El-Kishky, M. Abdel-Salam, and M. T. El-Mohandes, "On power quality of variable-speed constant-frequency aircraft electric

power systems," *IEEE Transactions on Power Delivery*, vol. 25, no. 1, pp. 55–65, Jan 2010.

[8] M. G. Jahromi, G. Mirzaeva, S. D. Mitchell, and D. Gay, "Powering mobile mining machines: Dc versus ac power," *IEEE Industry Applications Magazine*, vol. 22, no. 5, pp. 63–72, Sept 2016.

[9] G. Parise, L. Parise, A. Malerba, F. M. Pepe, A. Honorati, and P. B. Chavdarian, "Comprehensive peak-shaving solutions for port cranes," *IEEE Transactions on Industry Applications*, vol. PP, no. 99, pp. 1–1, 2016.

[10] Z. Jin, G. Sulligoi, R. Cuzner, L. Meng, J. C. Vasquez, and J. M. Guerrero, "Next-generation shipboard dc power system: Introduction smart grid and dc microgrid technologies into maritime electrical netowrks," *IEEE Electrification Magazine*, vol. 4, no. 2, pp. 45–57, June 2016.

[11] G. Sulligoi, A. Vicenzutti, and R. Menis, "All-electric ship design: From electrical propulsion to integrated electrical and electronic power systems," *IEEE Transactions on Transportation Electrification*, vol. 2, no. 4, pp. 507–521, Dec 2016.

[12] E. Prieto-Araujo, A. Junyent-Ferré, D. Lavèrnia-Ferrer, and O. Gomis-Bellmunt, "Decentralized control of a nine-phase permanent magnet generator for offshore wind turbines," *IEEE Transactions on Energy Conversion*, vol. 30, no. 3, pp. 1103–1112, Sept 2015.

[13] E. Jung, H. Yoo, S. K. Sul, H. S. Choi, and Y. Y. Choi, "A nine-phase permanent-magnet motor drive system for an ultrahigh-speed elevator," *IEEE Transactions on Industry Applications*, vol. 48, no. 3, pp. 987–995, May 2012.

[14] G. Pistoia, *Electric and Hybrid Vehicles - Power Sources, Models, Sustainability, Infrastructure and the Market.* Elsevier, 2010.

[15] R. Abebe, G. Vakil, G. L. Calzo, T. Cox, S. Lambert, M. Johnson, C. Gerada, and B. Mecrow, "Integrated motor drives: state of the art and future trends," *IET Electric Power Applications*, vol. 10, no. 8, pp. 757–771, 2016.

[16] R. Drath and A. Horch, "Industrie 4.0: Hit or hype? [industry forum]," *IEEE Industrial Electronics Magazine*, vol. 8, no. 2, pp. 56–58, June 2014.

[17] A. Emadi, "Guest editorial: Special issue on transportation electrification and vehicle systems," *IEEE Transactions on Power Electronics*, vol. 28, no. 12, pp. 5435–5436, Dec 2013.

[18] Y. Shakweh, G. H. Owen, D. J. Hall, and H. Miller, "Plug and play integrated motor drives," in *Power Electronics, Machines and Drives, 2002. International Conference on (Conf. Publ. No. 487)*, June 2002, pp. 655–661.

[19] J. Wang, Y. Li, and Y. Han, "Evaluation and design for an integrated modular motor drive (IMMD) with gan devices," in *Energy Conversion Congress and Exposition (ECCE), 2013 IEEE*, Sept 2013, pp. 4318–4325.

[20] ——, "Integrated modular motor drive design with gan power fets," *IEEE Transactions on Industry Applications*, vol. 51, no. 4, pp. 3198–3207, July 2015.

[21] P. Wheeler, J. Clare, M. Apap, L. Empringham, K. Bradley, S. Pickering, and D. Lampard, "A fully integrated 30 kW motor drive using matrix converter technology," in *Power Electronics and Applications, 2005 European Conference on*, 2005, pp. 9 pp.–P.9.

[22] A. Iyer, R. Kandula, R. Moghe, J. Hernandez, F. Lambert, and D. Divan, "Validation of the plug-and-play ac/ac power electronics building

block (ac-pebb) for medium-voltage grid control applications," *Industry Applications, IEEE Transactions on*, vol. 50, no. 5, pp. 3549–3557, Sept 2014.

[23] Y. Tadros, J. Ranneberg, and U. Schafer, "Ring shaped motor-integrated electric drive for hybrid electric vehicles," in *European Power Electronics conference (EPE)*, Toulouse, France, September 2003.

[24] C. Klumpner and F. Blaabjerg, "Short term braking capability during power interruptions for integrated matrix converter-motor drives," *Power Electronics, IEEE Transactions on*, vol. 19, no. 2, pp. 303–311, March 2004.

[25] N. R. Brown, T. Jahns, and R. Lorenz, "Power converter design for an integrated modular motor drive," in *Industry Applications Conference, 2007. 42nd IAS Annual Meeting. Conference Record of the 2007 IEEE*, Sept 2007, pp. 1322–1328.

[26] A. Shea and T. Jahns, "Hardware integration for an integrated modular motor drive including distributed control," in *Energy Conversion Congress and Exposition (ECCE), 2014 IEEE*, Sept 2014, pp. 4881–4887.

[27] M. Pulvirenti, G. Scarcella, G. Scelba, M. Cacciato, and A. Testa, "Fault-tolerant ac multidrive system," *Emerging and Selected Topics in Power Electronics, IEEE Journal of*, vol. 2, no. 2, pp. 224–235, June 2014.

[28] M. Shamsi-Nejad, B. Nahid-Mobarakeh, S. Pierfederici, and F. Meibody-Tabar, "Fault tolerant and minimum loss control of double-star synchronous machines under open phase conditions," *Industrial Electronics, IEEE Transactions on*, vol. 55, no. 5, pp. 1956–1965, May 2008.

[29] S. Khwan-on, L. De Lillo, L. Empringham, P. Wheeler, C. Gerada, N. Othman, O. Jasim, and J. Clare, "Fault tolerant power converter topologies for pmsm drives in aerospace applications," in *Power Electronics and Applications, 2009. EPE '09. 13th European Conference on*, Sept 2009, pp. 1–9.

[30] L. de Lillo, L. Empringham, P. Wheeler, S. Khwan-on, C. Gerada, M. Othman, and X. Huang, "Multiphase power converter drive for fault-tolerant machine development in aerospace applications," *Industrial Electronics, IEEE Transactions on*, vol. 57, no. 2, pp. 575–583, Feb 2010.

[31] F. Farina, D. Rossi, A. Tenconi, F. Profumo, and S. Bauer, "Thermal design of integrated motor drives for traction applications," in *Power Electronics and Applications, 2005 European Conference on*, 2005, pp. 10 pp.–P.10.

[32] A. Tenconi, F. Profumo, S. Bauer, and M. Hennen, "Temperatures evaluation in an integrated motor drive for traction applications," *Industrial Electronics, IEEE Transactions on*, vol. 55, no. 10, pp. 3619–3626, Oct 2008.

[33] R. Bojoi, A. Cavagnino, A. Tenconi, and S. Vaschetto, "Control of shaft-line-embedded multiphase starter/generator for aero-engine," *IEEE Transactions on Industrial Electronics*, vol. 63, no. 1, pp. 641–652, Jan 2016.

[34] M. Barcaro, N. Bianchi, and F. Magnussen, "Faulty operations of a PM fractional-slot machine with a dual three-phase winding," *IEEE Transactions on Industrial Electronics*, vol. 58, no. 9, pp. 3825–3832, Sept 2011.

[35] G. Scelba, G. Scarcella, M. Pulvirenti, M. Cacciato, A. Testa, S. De Caro, and T. Scimone, "Current-sharing strategies for fault-tolerant ac multidrives," *Industry Applications, IEEE Transactions on*, vol. 51, no. 5, pp. 3943–3953, Sept 2015.

[36] H. Guzman, I. Gonzalez, F. Barrero, and M. Durán, "Open-phase fault operation on multiphase induction motor drives," in *Induction Motors - Applications, Control and Fault Diagnostics*, R. Gregor, Ed. InTech, 2015.

[37] Allen-Bradley, "Load sharing applications for the 1336 impact ac drive," 1336E-WP001A-EN-P, June 2000. [Online]. Available: http://literature.rockwellautomation.com/idc/groups/literature/documents/wp/1336e-wp001_-en-p.pdf

[38] B. Jeftenic, M. Bebic, and S. Statkic, "Controlled multi-motor drives," in *Power Electronics, Electrical Drives, Automation and Motion, 2006. SPEEDAM 2006. International Symposium on*, May 2006, pp. 1392–1398.

[39] M. Aboelhassan, T. Raminosoa, A. Goodman, L. De Lillo, and C. Gerada, "Performance evaluation of a vector-control fault-tolerant flux-switching motor drive," *Industrial Electronics, IEEE Transactions on*, vol. 60, no. 8, pp. 2997–3006, Aug 2013.

[40] T. Raminosoa, C. Gerada, and M. Galea, "Design considerations for a fault-tolerant flux-switching permanent-magnet machine," *Industrial Electronics, IEEE Transactions on*, vol. 58, no. 7, pp. 2818–2825, July 2011.

[41] B. Welchko, T. Lipo, T. Jahns, and S. Schulz, "Fault tolerant three-phase ac motor drive topologies: a comparison of features, cost, and

limitations," *IEEE Transactions on Power Electronics*, vol. 19, no. 4, pp. 1108–1116, July 2004.

[42] N. Mitrovic, M. Petronijevic, V. Kostic, and J. B., *Electrical Drives for Crane Application, Mechanical Engineering*, IntechOpen, Ed. M. Gokcek, 2012. [Online]. Available: http://www.intechopen.com/books/mechanical-engineering/electrical-drives-for-crane-application

[43] Y. Zhao and T. Lipo, "Space vector pwm control of dual three-phase induction machine using vector space decomposition," *Industry Applications, IEEE Transactions on*, vol. 31, no. 5, pp. 1100–1109, Sep 1995.

[44] Y. Hu, Z. Q. Zhu, and M. Odavic, "Comparison of two-individual current control and vector space decomposition control for dual three-phase PMSM," *IEEE Transactions on Industry Applications*, vol. 53, no. 5, pp. 4483–4492, Sept 2017.

[45] Y. Hu, Z. Q. Zhu, and K. Liu, "Current control for dual three-phase permanent magnet synchronous motors accounting for current unbalance and harmonics," *IEEE Journal of Emerging and Selected Topics in Power Electronics*, vol. 2, no. 2, pp. 272–284, June 2014.

[46] A. Galassini, A. Costabeber, C. Gerada, G. Buticchi, and D. Barater, "A modular speed-drooped system for high reliability integrated modular motor drives," *IEEE Transactions on Industry Applications*, vol. 52, no. 4, pp. 3124–3132, July 2016.

[47] R. Bojoi, S. Rubino, A. Tenconi, and S. Vaschetto, "Multiphase electrical machines and drives: A viable solution for energy generation and transportation electrification," in *2016 International Conference and Exposition on Electrical and Power Engineering (EPE)*, Oct 2016, pp. 632–639.

[48] A. Galassini, A. Costabeber, C. Gerada, A. Tessarolo, and R. Menis, "Speed control with load sharing capabilities for multi-three phase syn-

chronous motors," 43rd Annual Conference of the IEEE Industrial Electronics Society (IECON), Nov 2017.

[49] A. Tessarolo, "Modeling and analysis of multiphase machines for high power applications," Ph.D. dissertation, The University of Trieste, 2011.

[50] S. Kobayashi, M. Ooshima, and M. N. Uddin, "A radial position control method of bearingless motor based on *d-q* axis current control," *IEEE Transactions on Industry Applications*, vol. 49, no. 4, pp. 1827–1835, July 2013.

[51] X. L. Wang, Q. C. Zhong, Z. Q. Deng, and S. Z. Yue, "Current-controlled multiphase slice permanent magnetic bearingless motors with open-circuited phases: Fault-tolerant controllability and its verification," *IEEE Transactions on Industrial Electronics*, vol. 59, no. 5, pp. 2059–2072, May 2012.

[52] G. Valente, L. Papini, A. Formentini, C. Gerada, and P. Zanchetta, "Radial force control of multi-sector permanent magnet machines," in *2016 XXII International Conference on Electrical Machines (ICEM)*, Sept 2016, pp. 2595–2601.

[53] E. Klingshirn, "High phase order induction motors - part I-Description and theoretical considerations," *IEEE Transactions on Power Apparatus and Systems,*, vol. PAS-102, no. 1, pp. 47–53, Jan 1983.

[54] A. Tessarolo, L. Branz, and M. Bortolozzi, "Stator inductance matrix diagonalization algorithms for different multi-phase winding schemes of round-rotor electric machines part I. Theory," in *EUROCON 2015 - International Conference on Computer as a Tool (EUROCON), IEEE*, Sept 2015.

[55] ——, "Stator inductance matrix diagonalization algorithms for different multi-phase winding schemes of round-rotor electric machines part II.

Examples and validations," in *EUROCON 2015 - International Conference on Computer as a Tool (EUROCON), IEEE*, Sept 2015.

[56] A. Tessarolo, M. Bortolozzi, and A. Contin, "Modeling of split-phase machines in park's coordinates. Part I: Theoretical foundations," in *EUROCON, 2013 IEEE*, July 2013, pp. 1308–1313.

[57] ——, "Modeling of split-phase machines in park's coordinates. Part II: Equivalent circuit representation," in *EUROCON, 2013 IEEE*, July 2013, pp. 1314–1319.

[58] A. A. Rockhill and T. A. Lipo, "A generalized transformation methodology for polyphase electric machines and networks," in *2015 IEEE International Electric Machines Drives Conference (IEMDC)*, May 2015, pp. 27–34.

[59] D. Hadiouche, H. Razik, and A. Rezzoug, "On the modeling and design of dual-stator windings to minimize circulating harmonic currents for VSI fed AC machines," *IEEE Transactions on Industry Applications*, vol. 40, no. 2, pp. 506–515, March 2004.

[60] S. Gataric, "A polyphase cartesian vector approach to control of polyphase ac machines," in *Conference Record of the 2000 IEEE Industry Applications Conference. Thirty-Fifth IAS Annual Meeting and World Conference on Industrial Applications of Electrical Energy (Cat. No.00CH37129)*, vol. 3, 2000, pp. 1648–1654 vol.3.

[61] J. Figueroa, J. Cros, and P. Viarouge, "Generalized transformations for polyphase phase-modulation motors," *IEEE Transactions on Energy Conversion*, vol. 21, no. 2, pp. 332–341, June 2006.

[62] C. L. Fortescue, "Method of symmetrical co-ordinates applied to the solution of polyphase networks," *Transactions of the American Institute of Electrical Engineers*, vol. XXXVII, no. 2, pp. 1027–1140, July 1918.

[63] D. White and H. Woodson, *Electromechanical Energy Conversion*, ser. [The M.I.T. core curriculum program in electrical engineering]. Wiley, 1959.

[64] E. Levi, "Multiphase ac machines," in *Power Electronics and Motor Drives*, ser. Electrical Engineering Handbook. CRC Press, Feb. 2011, pp. 1–31. [Online]. Available: https://doi.org/10.1201/b10643-6

[65] A. Tessarolo, G. Zocco, and C. Tonello, "Design and testing of a 45-MW 100-Hz quadruple-star synchronous motor for a liquefied natural gas turbo-compressor drive," *IEEE Transactions on Industry Applications*, vol. 47, no. 3, pp. 1210–1219, May 2011.

[66] R. De Doncker, D. Pulle, and A. Veltman, *Advanced Electrical Drives: Analysis, Modeling, Control*, ser. Power Systems. Springer Netherlands, 2010.

[67] V. Nasirian, A. Davoudi, F. L. Lewis, and J. M. Guerrero, "Distributed adaptive droop control for dc distribution systems," *IEEE Transactions on Energy Conversion*, vol. 29, no. 4, pp. 944–956, Dec 2014.

[68] W. Allen J., W. Bruce F., and S. Gerald B., *Power Generation, Operation, and Control*. Wiley, 1984.

[69] Q.-C. Zhong, "Robust droop controller for accurate proportional load sharing among inverters operated in parallel," *Industrial Electronics, IEEE Transactions on*, vol. 60, no. 4, pp. 1281–1290, April 2013.

[70] T. Lazzarin, G. Bauer, and I. Barbi, "A control strategy for parallel operation of single-phase voltage source inverters: Analysis, design and experimental results," *Industrial Electronics, IEEE Transactions on*, vol. 60, no. 6, pp. 2194–2204, June 2013.

[71] B. Johnson, R. Lasseter, F. Alvarado, and R. Adapa, "Expandable multiterminal dc systems based on voltage droop," *Power Delivery, IEEE Transactions on*, vol. 8, no. 4, pp. 1926–1932, Oct 1993.

[72] U. Borup, F. Blaabjerg, and P. Enjeti, "Sharing of nonlinear load in parallel-connected three-phase converters," *Industry Applications, IEEE Transactions on*, vol. 37, no. 6, pp. 1817–1823, Nov 2001.

[73] S. D'Arco, A. Petterteig, R. Pittini, and T. Undeland, "Droop regulated vscs for island operation of future offshore systems," in *PowerTech, 2011 IEEE Trondheim*, June 2011, pp. 1–6.

[74] D. Fingas and P. Lehn, "Operation of parallel three-phase converters as a motor drive," in *Industrial Electronics, 2009. IECON '09. 35th Annual Conference of IEEE*, Nov 2009, pp. 1217–1222.

[75] L. de Lillo, P. Wheeler, L. Empringham, C. Gerada, and Xiaoyan-Huang, "A power converter for fault tolerant machine development in aerospace applications," in *Power Electronics and Motion Control Conference, 2008. EPE-PEMC 2008. 13th*, Sept 2008, pp. 388–392.

[76] A. Galassini, G. L. Calzo, A. Formentini, C. Gerada, P. Zancehtta, and A. Costabeber, "uCube: Control platform for power electronics," 2017 IEEE Workshop on Electrical Machines Design, Control and Diagnosis (WEMDCD), April 2017.

[77] "Microzed," http://microzed.org/product/microzed.

[78] J. M. Rabaey, A. Abnous, Y. Ichikawa, K. Seno, and M. Wan, "Heterogeneous reconfigurable systems," in *1997 IEEE Workshop on Signal Processing Systems. SiPS 97 Design and Implementation formerly VLSI Signal Processing*, Nov 1997, pp. 24–34.

[79] L. H. Crockett, R. A. Elliot, M. A. Enderwitz, and R. W. Stewart, *The Zynq Book: Embedded Processing with the Arm Cortex-A9 on the Xilinx Zynq-7000 All Programmable Soc.* Strathclyde Academic Media, 2014.

[80] "Zynq-7000 all programmable soc," http://www.xilinx.com/products/silicon-devices/soc.html, Nov 2016.

[81] J. McDougall. (2013, February) Simple amp running linux and bare-metal system on both zynq soc processors. Xilinx. [Online]. Available: http://www.xilinx.com/support/documentation/application_notes/xapp1078-amp-linux-bare-metal.pdf

[82] "Modbus specifications," http://www.modbus.org/specs.php, Nov 2016.

[83] S. Raimbault, "libmodbus," http://libmodbus.org/.

Appendices

Appendix A

Matrix diagonalisation - Even n

Aim of this appendix is at aiding the Vector Space Decomposition comprehension. More precisely, it will be shown how the de-coupling matrix $\mathbf{T}_{vsd}$ in (2.32) is built for a $n = 12$ phase multi-three-phase machine starting from data computed by mean of Finite Element (FE) analysis following the flow chart in Fig. 3.2.

According to equation (2.30) and being $\nu = n/2 = 6$, the q-set of harmonic orders to be processed which can be used for building matrix $\mathbf{Q}_{h_1,..h_\nu}$ is the following:

$$q = 1, 3, 5, 7, .., 2\nu - 1 = 1, 3, 5, 7, 9, 11 \tag{A.1}$$

Re-calling the work-flow in Fig. 3.2, $\mathbf{L}_{dq}$ matrix values are expressed in $p.u. = 2\pi f_n\sqrt{3}I_n/V_n$, where f_n is the fundamental electric frequency, I_n and V_n are the nominal RMS current and the nominal RMS line to line voltage, respectively. In this particular case, $V_n = 690V$, $I_n = 2092A$, and $f_n = 60Hz$, stator leakage inductances M, H, and X are the one in Table 3.1 and magnetising inductances are $L_{md} = L_{mq} = 1.62p.u.$. The resulting $\mathbf{L}_{dq}$ matrix in (2.7) is the following:

$$\mathbf{L}_{dq} = \left[\begin{array}{ccc:ccc:ccc:ccc} 1.72 & 0 & 0 & 1.64 & 0 & 0 & 1.63 & 0 & 0 & 1.64 & 0 & 0 \\ 0 & 1.72 & 0 & 0 & 1.64 & 0 & 0 & 1.63 & 0 & 0 & 1.64 & 0 \\ 0 & 0 & 0.1 & 0 & 0 & 0.02 & 0 & 0 & 0 & 0 & 0 & -0.02 \\ \hdashline 1.64 & 0 & 0 & 1.72 & 0 & 0 & 1.64 & 0 & 0 & 1.63 & 0 & 0 \\ 0 & 1.64 & 0 & 0 & 1.72 & 0 & 0 & 1.64 & 0 & 0 & 1.63 & 0 \\ 0 & 0 & 0.02 & 0 & 0 & 0.1 & 0 & 0 & 0.02 & 0 & 0 & 0 \\ \hdashline 1.63 & 0 & 0 & 1.64 & 0 & 0 & 1.72 & 0 & 0 & 1.64 & 0 & 0 \\ 0 & 1.63 & 0 & 0 & 1.64 & 0 & 0 & 1.72 & 0 & 0 & 1.64 & 0 \\ 0 & 0 & 0 & 0 & 0 & 0.02 & 0 & 0 & 0.1 & 0 & 0 & 0.02 \\ \hdashline 1.64 & 0 & 0 & 1.63 & 0 & 0 & 1.64 & 0 & 0 & 1.72 & 0 & 0 \\ 0 & 1.64 & 0 & 0 & 1.63 & 0 & 0 & 1.64 & 0 & 0 & 1.72 & 0 \\ 0 & 0 & -0.02 & 0 & 0 & 0 & 0 & 0 & 0.02 & 0 & 0 & 0.1 \end{array}\right] \tag{A.2}$$

The geometrical transformation mapping the split-phase winding arrangement into the n-phase one described by (2.8) is the following:

$$\mathbf{W} = \left[\begin{array}{ccc:ccc:ccc:ccc} 1 & 0 & 0 & 0 & 0 & 0 & 0 & 0 & 0 & 0 & 0 & 0 \\ 0 & 0 & 0 & 1 & 0 & 0 & 0 & 0 & 0 & 0 & 0 & 0 \\ 0 & 0 & 0 & 0 & 0 & 0 & 1 & 0 & 0 & 0 & 0 & 0 \\ \hdashline 0 & 0 & 0 & 0 & 0 & 0 & 0 & 0 & 0 & 1 & 0 & 0 \\ 0 & 0 & -1 & 0 & 0 & 0 & 0 & 0 & 0 & 0 & 0 & 0 \\ 0 & 0 & 0 & 0 & 0 & -1 & 0 & 0 & 0 & 0 & 0 & 0 \\ \hdashline 0 & 0 & 0 & 0 & 0 & 0 & 0 & 0 & -1 & 0 & 0 & 0 \\ 0 & 0 & 0 & 0 & 0 & 0 & 0 & 0 & 0 & 0 & 0 & -1 \\ 0 & 1 & 0 & 0 & 0 & 0 & 0 & 0 & 0 & 0 & 0 & 0 \\ \hdashline 0 & 0 & 0 & 0 & 1 & 0 & 0 & 0 & 0 & 0 & 0 & 0 \\ 0 & 0 & 0 & 0 & 0 & 0 & 0 & 1 & 0 & 0 & 0 & 0 \\ 0 & 0 & 0 & 0 & 0 & 0 & 0 & 0 & 0 & 0 & 1 & 0 \end{array}\right] \tag{A.3}$$

Defining $\alpha_{12} = \alpha = \pi/12$, the de-coupling matrix for the stationary orthonormal reference frame in (2.15) is the following:

$$\mathbf{Q}_{12} = \sqrt{\frac{2}{12}} \left[\begin{array}{cccccc} 1 & \cos(\alpha_{12}) & \cos(2\alpha_{12}) & \cos(3\alpha_{12}) & \cdots & \cos(10\alpha_{12}) & \cos(11\alpha_{12}) \\ 0 & \sin(\alpha_{12}) & \sin(2\alpha_{12}) & \sin(3\alpha_{12}) & \cdots & \sin(10\alpha_{12}) & \sin(11\alpha_{12}) \\ \hdashline 1 & \cos(3\alpha_{12}) & \cos(6\alpha_{12}) & \cos(9\alpha_{12}) & \cdots & \cos(30\alpha_{12}) & \cos(33\alpha_{12}) \\ 0 & \sin(3\alpha_{12}) & \sin(6\alpha_{12}) & \sin(9\alpha_{12}) & \cdots & \sin(30\alpha_{12}) & \sin(33\alpha_{12}) \\ \hdashline 1 & \cos(5\alpha_{12}) & \cos(10\alpha_{12}) & \cos(15\alpha_{12}) & \cdots & \cos(50\alpha_{12}) & \cos(55\alpha_{12}) \\ 0 & \sin(5\alpha_{12}) & \sin(10\alpha_{12}) & \sin(15\alpha_{12}) & \cdots & \sin(50\alpha_{12}) & \sin(55\alpha_{12}) \\ \hdashline 1 & \cos(7\alpha_{12}) & \cos(14\alpha_{12}) & \cos(21\alpha_{12}) & \cdots & \cos(70\alpha_{12}) & \cos(77\alpha_{12}) \\ 0 & \sin(7\alpha_{12}) & \sin(14\alpha_{12}) & \sin(21\alpha_{12}) & \cdots & \sin(70\alpha_{12}) & \sin(77\alpha_{12}) \\ \hdashline 1 & \cos(9\alpha_{12}) & \cos(18\alpha_{12}) & \cos(27\alpha_{12}) & \cdots & \cos(90\alpha_{12}) & \cos(99\alpha_{12}) \\ 0 & \sin(9\alpha_{12}) & \sin(18\alpha_{12}) & \sin(27\alpha_{12}) & \cdots & \sin(90\alpha_{12}) & \sin(99\alpha_{12}) \\ \hdashline 1 & \cos(11\alpha_{12}) & \cos(22\alpha_{12}) & \cos(33\alpha_{12}) & \cdots & \cos(110\alpha_{12}) & \cos(121\alpha_{12}) \\ 0 & \sin(11\alpha_{12}) & \sin(22\alpha_{12}) & \sin(33\alpha_{12}) & \cdots & \sin(110\alpha_{12}) & \sin(121\alpha_{12}) \end{array}\right] =$$

$$\left[\begin{array}{cccccccccccc} 0.41 & 0.39 & 0.35 & 0.29 & 0.20 & 0.11 & 0 & -0.11 & -0.20 & -0.29 & -0.35 & -0.39 \\ 0 & 0.11 & 0.20 & 0.29 & 0.35 & 0.39 & 0.41 & 0.39 & 0.35 & 0.29 & 0.20 & 0.11 \\ \hdashline 0.41 & 0.29 & 0 & -0.29 & -0.41 & -0.29 & 0 & 0.29 & 0.41 & 0.29 & 0 & -0.29 \\ 0 & 0.29 & 0.41 & 0.29 & 0 & -0.29 & -0.41 & -0.29 & 0 & 0.29 & 0.41 & 0.29 \\ \hdashline 0.41 & 0.11 & -0.35 & -0.29 & 0.20 & 0.39 & 0 & -0.39 & -0.20 & 0.29 & 0.35 & -0.11 \\ 0 & 0.39 & 0.20 & -0.29 & -0.35 & 0.11 & 0.41 & 0.11 & -0.35 & -0.29 & 0.20 & 0.39 \\ \hdashline 0.41 & -0.11 & -0.35 & 0.29 & 0.20 & -0.39 & 0 & 0.39 & -0.20 & -0.29 & 0.35 & 0.11 \\ 0 & 0.39 & -0.20 & -0.29 & 0.35 & 0.11 & -0.41 & 0.11 & 0.35 & -0.29 & -0.20 & 0.39 \\ \hdashline 0.41 & -0.29 & 0 & 0.29 & -0.41 & 0.29 & 0 & -0.29 & 0.41 & -0.29 & 0 & 0.29 \\ 0 & 0.29 & -0.41 & 0.29 & 0 & -0.29 & 0.41 & -0.29 & 0 & 0.29 & -0.41 & 0.29 \\ \hdashline 0.41 & -0.39 & 0.35 & -0.29 & 0.20 & -0.11 & 0 & 0.11 & -0.20 & 0.29 & -0.35 & 0.39 \\ 0 & 0.11 & -0.20 & 0.29 & -0.35 & 0.39 & -0.41 & 0.39 & -0.35 & 0.29 & -0.20 & 0.11 \end{array}\right] \tag{A.4}$$

The de-coupling matrix for the rotating orthonormal reference frame in (2.25) is the following:

$$\mathbf{P}_{12}(\theta) = \left[\begin{array}{cc:cc:cc:c:cc} \cos(\theta) & \sin(\theta) & 0 & 0 & 0 & 0 & \vdots & 0 & 0 \\ -\sin(\theta) & \cos(\theta) & 0 & 0 & 0 & 0 & \vdots & 0 & 0 \\ \hdashline 0 & 0 & \cos(2\theta) & \sin(2\theta) & 0 & 0 & \vdots & 0 & 0 \\ 0 & 0 & -\sin(2\theta) & \cos(2\theta) & 0 & 0 & \vdots & 0 & 0 \\ \hdashline 0 & 0 & 0 & 0 & \cos(3\theta) & \sin(3\theta) & \vdots & 0 & 0 \\ 0 & 0 & 0 & 0 & -\sin(3\theta) & \cos(3\theta) & \vdots & 0 & 0 \\ \hdashline 0 & 0 & 0 & 0 & 0 & 0 & \ddots & 0 & 0 \\ \hdashline 0 & 0 & 0 & 0 & 0 & 0 & \cdots & \cos(6\theta) & \sin(6\theta) \\ 0 & 0 & 0 & 0 & 0 & 0 & \cdots & -\sin(6\theta) & \cos(6\theta) \end{array}\right] \tag{A.5}$$

For illustration purposes, only if assumed that $\theta = 2$, one gets:

$$\mathbf{P}_{12}(2) = \left[\begin{array}{cc:cc:cc:cc:cc:cc} -0.42 & 0.91 & 0 & 0 & 0 & 0 & 0 & 0 & 0 & 0 & 0 & 0 \\ -0.91 & -0.42 & 0 & 0 & 0 & 0 & 0 & 0 & 0 & 0 & 0 & 0 \\ \hdashline 0 & 0 & -0.65 & -0.76 & 0 & 0 & 0 & 0 & 0 & 0 & 0 & 0 \\ 0 & 0 & 0.76 & -0.65 & 0 & 0 & 0 & 0 & 0 & 0 & 0 & 0 \\ \hdashline 0 & 0 & 0 & 0 & 0.96 & -0.28 & 0 & 0 & 0 & 0 & 0 & 0 \\ 0 & 0 & 0 & 0 & 0.28 & 0.96 & 0 & 0 & 0 & 0 & 0 & 0 \\ \hdashline 0 & 0 & 0 & 0 & 0 & 0 & -0.15 & 0.99 & 0 & 0 & 0 & 0 \\ 0 & 0 & 0 & 0 & 0 & 0 & -0.99 & -0.15 & 0 & 0 & 0 & 0 \\ \hdashline 0 & 0 & 0 & 0 & 0 & 0 & 0 & 0 & -0.84 & -0.54 & 0 & 0 \\ 0 & 0 & 0 & 0 & 0 & 0 & 0 & 0 & 0.54 & -0.84 & 0 & 0 \\ \hdashline 0 & 0 & 0 & 0 & 0 & 0 & 0 & 0 & 0 & 0 & 0.84 & -0.54 \\ 0 & 0 & 0 & 0 & 0 & 0 & 0 & 0 & 0 & 0 & 0.54 & 0.84 \end{array}\right] \tag{A.6}$$

Defining $\mathbf{T}_d = \mathbf{P}_{12}\mathbf{Q}_{12}$, the final real-valued orthonormal decoupling transformation matrix $\mathbf{T}_{vsd}$ is the following (the selected instant of time when $\theta = 2$ is used as example):

$$\mathbf{T}_{vsd}(2) = \mathbf{T}_d(2)\mathbf{W} =$$

$$\begin{bmatrix}
-0.17 & 0.41 & -0.24 & -0.07 & 0.38 & -0.31 & 0.04 & 0.33 & -0.37 & 0.14 & 0.26 & -0.40 \\
-0.37 & 0.04 & 0.33 & -0.40 & 0.14 & 0.26 & -0.41 & 0.24 & 0.17 & -0.38 & 0.31 & 0.07 \\
-0.27 & -0.27 & -0.27 & -0.41 & -0.41 & -0.41 & -0.31 & -0.31 & -0.31 & -0.03 & -0.03 & -0.03 \\
0.31 & 0.31 & 0.31 & 0.03 & 0.03 & 0.03 & -0.27 & -0.27 & -0.27 & -0.41 & -0.41 & -0.41 \\
0.39 & -0.10 & -0.29 & -0.01 & 0.36 & -0.35 & -0.40 & 0.28 & 0.11 & -0.20 & -0.21 & 0.41 \\
0.11 & -0.40 & 0.28 & 0.41 & -0.20 & -0.21 & 0.10 & 0.29 & -0.39 & -0.36 & 0.35 & 0.01 \\
-0.06 & 0.38 & -0.32 & 0.41 & -0.24 & -0.16 & -0.15 & -0.25 & 0.40 & -0.33 & 0.37 & -0.05 \\
-0.40 & 0.15 & 0.25 & 0.05 & 0.33 & -0.37 & 0.38 & -0.32 & -0.06 & -0.24 & -0.16 & 0.41 \\
-0.34 & -0.34 & -0.34 & 0.09 & 0.09 & 0.09 & 0.22 & 0.22 & 0.22 & -0.40 & -0.40 & -0.40 \\
0.22 & 0.22 & 0.22 & -0.40 & -0.40 & -0.40 & 0.34 & 0.34 & 0.34 & -0.09 & -0.09 & -0.09 \\
0.34 & 0.02 & -0.36 & -0.39 & 0.09 & 0.30 & 0.41 & -0.19 & -0.22 & -0.40 & 0.28 & 0.12 \\
0.22 & -0.41 & 0.19 & -0.12 & 0.40 & -0.28 & 0.02 & -0.36 & 0.34 & 0.09 & 0.30 & -0.39
\end{bmatrix} \tag{A.7}$$

The transformation matrix $\mathbf{T}_{vsd}$ is meant to diagonalise the phase inductance matrix $\mathbf{L}_{abc} = \mathbf{T}_{park}^T \mathbf{L}_{dq} \mathbf{T}_{Park}$.

$$\mathbf{T}(\theta, h = 3, \alpha = \alpha_{12})$$

$$= \sqrt{\frac{2}{3}} \begin{bmatrix} \cos(\theta - 2\alpha_{12}) & \sin(\theta - 2\alpha_{12}) & 0 \\ -\sin(\theta - 2\alpha_{12}) & \cos(\theta - 2\alpha_{12}) & 0 \\ 0 & 0 & 1 \end{bmatrix} \begin{bmatrix} 1 & -\frac{1}{2} & -\frac{1}{2} \\ 0 & \frac{\sqrt{3}}{2} & -\frac{\sqrt{3}}{2} \\ \frac{1}{\sqrt{2}} & \frac{1}{\sqrt{2}} & \frac{1}{\sqrt{2}} \end{bmatrix} \tag{A.8}$$

which with $\theta = 2$ gives:

$$\mathbf{T}(\theta = 2, h = 3, \alpha = \alpha_{12}) \begin{bmatrix} 0.08 & 0.67 & -0.74 \\ -0.81 & 0.47 & 0.34 \\ 0.58 & 0.58 & 0.58 \end{bmatrix} \tag{A.9}$$

For simplicity, in the above equation only the third set of windings transformation is shown. Combining on the diagonal the Park's transformations for every set of windings, the final Park's transformation matrix mapping $dq0$ into abc is the following:

$$\mathbf{T}_{Park}(\theta = 2)$$

$$= \left[\begin{array}{ccc:ccc:ccc:ccc} -0.34 & 0.81 & -0.47 & 0 & 0 & 0 & 0 & 0 & 0 & 0 & 0 & 0 \\ -0.74 & 0.08 & 0.67 & 0 & 0 & 0 & 0 & 0 & 0 & 0 & 0 & 0 \\ 0.58 & 0.58 & 0.58 & 0 & 0 & 0 & 0 & 0 & 0 & 0 & 0 & 0 \\ \hdashline 0 & 0 & 0 & -0.14 & 0.77 & -0.63 & 0 & 0 & 0 & 0 & 0 & 0 \\ 0 & 0 & 0 & -0.81 & 0.28 & 0.52 & 0 & 0 & 0 & 0 & 0 & 0 \\ 0 & 0 & 0 & 0.58 & 0.58 & 0.58 & 0 & 0 & 0 & 0 & 0 & 0 \\ \hdashline 0 & 0 & 0 & 0 & 0 & 0 & 0.08 & 0.67 & -0.74 & 0 & 0 & 0 \\ 0 & 0 & 0 & 0 & 0 & 0 & -0.81 & 0.47 & 0.34 & 0 & 0 & 0 \\ 0 & 0 & 0 & 0 & 0 & 0 & 0.58 & 0.58 & 0.58 & 0 & 0 & 0 \\ \hdashline 0 & 0 & 0 & 0 & 0 & 0 & 0 & 0 & 0 & 0.28 & 0.52 & -0.81 \\ 0 & 0 & 0 & 0 & 0 & 0 & 0 & 0 & 0 & -0.77 & 0.63 & 0.14 \\ 0 & 0 & 0 & 0 & 0 & 0 & 0 & 0 & 0 & 0.58 & 0.58 & 0.58 \end{array}\right] \tag{A.10}$$

and the following is the phase inductance matrix:

$$\mathbf{L}_{abc} = \mathbf{T}_{park}^{T}\mathbf{L}_{dq}\mathbf{T}_{Park} =$$

$$\left[\begin{array}{ccc:ccc:ccc:ccc} 1.18 & -0.54 & -0.54 & 1.06 & -0.77 & -0.28 & 0.94 & -0.94 & 0 & 0.77 & -1.06 & 0.28 \\ -0.54 & 1.18 & -0.54 & -0.28 & 1.06 & -0.77 & 0 & 0.94 & -0.94 & 0.28 & 0.77 & -1.06 \\ -0.54 & -0.54 & 1.18 & -0.77 & -0.28 & 1.06 & -0.94 & 0 & 0.94 & -1.06 & 0.28 & 0.77 \\ \hdashline 1.06 & -0.28 & -0.77 & 1.18 & -0.54 & -0.54 & 1.06 & -0.77 & -0.28 & 0.94 & -0.94 & 0 \\ -0.77 & 1.06 & -0.28 & -0.54 & 1.18 & -0.54 & -0.28 & 1.06 & -0.77 & 0 & 0.94 & -0.94 \\ -0.28 & -0.77 & 1.06 & -0.54 & -0.54 & 1.18 & -0.77 & -0.28 & 1.06 & -0.94 & 0 & 0.94 \\ \hdashline 0.94 & 0 & -0.94 & 1.06 & -0.28 & -0.77 & 1.18 & -0.54 & -0.54 & 1.06 & -0.77 & -0.28 \\ -0.94 & 0.94 & 0 & -0.77 & 1.06 & -0.28 & -0.54 & 1.18 & -0.54 & -0.28 & 1.06 & -0.77 \\ 0 & -0.94 & 0.94 & -0.28 & -0.77 & 1.06 & -0.54 & -0.54 & 1.18 & -0.77 & -0.28 & 1.06 \\ \hdashline 0.77 & 0.28 & -1.06 & 0.94 & 0 & -0.94 & 1.06 & -0.28 & -0.77 & 1.18 & -0.54 & -0.54 \\ -1.06 & 0.77 & 0.28 & -0.94 & 0.94 & 0 & -0.77 & 1.06 & -0.28 & -0.54 & 1.18 & -0.54 \\ 0.28 & -1.06 & 0.77 & 0 & -0.94 & 0.94 & -0.28 & -0.77 & 1.06 & -0.54 & -0.54 & 1.18 \end{array}\right] \tag{A.11}$$

Finally, applying the real-valued orthonormal decoupling transformation matrix $\mathbf{T}_{vsd}$, it is possible to compute the harmonic inductances with the following equation:

$$\mathbf{L}_{vsd} = \mathbf{T}_{vsd}\mathbf{L}_{abc}\mathbf{T}_{vsd}^{T} =$$

$$\left[\begin{array}{cc:cc:cc:cc:cc:cc}
6.630 & 0 & 0 & 0 & 0 & 0 & 0 & 0 & 0 & 0 & 0 & 0 \\
0 & 6.630 & 0 & 0 & 0 & 0 & 0 & 0 & 0 & 0 & 0 & 0 \\
\hdashline
0 & 0 & 0.128 & 0 & 0 & 0 & 0 & 0 & 0 & 0 & 0 & 0 \\
0 & 0 & 0 & 0.128 & 0 & 0 & 0 & 0 & 0 & 0 & 0 & 0 \\
\hdashline
0 & 0 & 0 & 0 & 0.090 & 0 & 0 & 0 & 0 & 0 & 0 & 0 \\
0 & 0 & 0 & 0 & 0 & 0.090 & 0 & 0 & 0 & 0 & 0 & 0 \\
\hdashline
0 & 0 & 0 & 0 & 0 & 0 & 0.090 & 0 & 0 & 0 & 0 & 0 \\
0 & 0 & 0 & 0 & 0 & 0 & 0 & 0.090 & 0 & 0 & 0 & 0 \\
\hdashline
0 & 0 & 0 & 0 & 0 & 0 & 0 & 0 & 0.072 & 0 & 0 & 0 \\
0 & 0 & 0 & 0 & 0 & 0 & 0 & 0 & 0 & 0.072 & 0 & 0 \\
\hdashline
0 & 0 & 0 & 0 & 0 & 0 & 0 & 0 & 0 & 0 & 0.070 & 0 \\
0 & 0 & 0 & 0 & 0 & 0 & 0 & 0 & 0 & 0 & 0 & 0.070
\end{array}\right] \tag{A.12}$$

In this particular case, $d_1 = q_1 = 6.63$. The final harmonic inductances to be considered for current control loop design are $d_1/pu = q_1/pu = 0.0033H$.

Appendix B

Matrix diagonalisation - Odd n

Aim of this appendix is at aiding the Vector Space Decomposition comprehension. More precisely, it will be shown how the de-coupling matrix $\mathbf{T}_{vsd}$ in (2.32) is built for a $n = 9$ phase multi-three-phase machine starting from data computed by mean of Finite Element (FE) analysis following the flow chart in Fig. 3.2.

According to equation (2.30) and being $\nu = (n-1)/2 = 4$, the q-set of harmonic orders to be processed which can be used for building matrix $\mathbf{Q}_{h_1,..h_\nu}$ is the following:

$$q = 1, 3, 5, 7, .., 2\nu + 1 = 1, 3, 5, 7, 9 \tag{B.1}$$

Re-calling the work-flow in Fig. 3.2, $\mathbf{L}_{dq}$ matrix values are expressed in $p.u. = 2\pi f_n \sqrt{3} I_n / V_n$, where f_n is the fundamental electric frequency, I_n and V_n are the nominal RMS current and the nominal RMS line to line voltage, respectively. In this particular case, $V_n = 760V$, $I_n = 17A$, and $f_n = 50Hz$. Based on FE analysis, the final $\mathbf{L}_{dq}$ matrix in (2.7) is the following:

$$\mathbf{L}_{dq} =$$

$$\left[\begin{array}{ccc:ccc:ccc}
0.69649 & 0 & 0 & 0.69550 & -0.00003 & 0 & 0.69550 & 0.00003 & 0 \\
0 & 0.48841 & 0 & 0.00003 & 0.48742 & 0 & -0.00003 & 0.48742 & 0 \\
0 & 0 & 0.00151 & 0 & 0 & 0.00035 & 0 & 0 & -0.00035 \\
\hdashline
0.69550 & 0.00003 & 0 & 0.69649 & 0 & 0 & 0.69550 & -0.00003 & 0 \\
-0.00003 & 0.48742 & 0 & 0 & 0.48841 & 0 & 0.00003 & 0.48742 & 0 \\
0 & 0 & 0.00035 & 0 & 0 & 0.00151 & 0 & 0 & 0.00035 \\
\hdashline
0.69550 & -0.00003 & 0 & 0.69550 & 0.00003 & 0 & 0.69649 & 0 & 0 \\
0.00003 & 0.48742 & 0 & -0.00003 & 0.48742 & 0 & 0 & 0.48841 & 0 \\
0 & 0 & -0.00035 & 0 & 0 & 0.00035 & 0 & 0 & 0.00151
\end{array}\right] \tag{B.2}$$

The geometrical transformation mapping the split-phase winding arrangement into the n-phase one described by (2.8) is the following:

$$\mathbf{W} = \left[\begin{array}{ccc:ccc:ccc}
1 & 0 & 0 & 0 & 0 & 0 & 0 & 0 & 0 \\
0 & 0 & 0 & 1 & 0 & 0 & 0 & 0 & 0 \\
0 & 0 & 0 & 0 & 0 & 0 & 1 & 0 & 0 \\
\hdashline
0 & 0 & -1 & 0 & 0 & 0 & 0 & 0 & 0 \\
0 & 0 & 0 & 0 & 0 & -1 & 0 & 0 & 0 \\
0 & 0 & 0 & 0 & 0 & 0 & 0 & 0 & -1 \\
\hdashline
0 & 1 & 0 & 0 & 0 & 0 & 0 & 0 & 0 \\
0 & 0 & 0 & 0 & 1 & 0 & 0 & 0 & 0 \\
0 & 0 & 0 & 0 & 0 & 0 & 0 & 1 & 0
\end{array}\right] \tag{B.3}$$

Defining $\alpha_9 = \alpha = \pi/9$, the de-coupling matrix for the stationary orthonormal reference frame in (2.15) is the following:

$$\mathbf{Q}_9 = \sqrt{\frac{2}{9}} \left[\begin{array}{cccccccc} 1 & \cos(\alpha_9) & \cos(2\alpha_9) & \cos(3\alpha_9) & \cdots & \cos(7\alpha_9) & \cos(8\alpha_9) \\ 0 & \sin(\alpha_9) & \sin(2\alpha_9) & \sin(3\alpha_9) & \cdots & \sin(7\alpha_9) & \sin(8\alpha_9) \\ \hdashline 1 & \cos(3\alpha_9) & \cos(6\alpha_9) & \cos(9\alpha_9) & \cdots & \cos(21\alpha_9) & \cos(24\alpha_9) \\ 0 & \sin(3\alpha_9) & \sin(6\alpha_9) & \sin(9\alpha_9) & \cdots & \sin(21\alpha_9) & \sin(24\alpha_9) \\ \hdashline 1 & \cos(5\alpha_9) & \cos(10\alpha_9) & \cos(15\alpha_9) & \cdots & \cos(35\alpha_9) & \cos(40\alpha_9) \\ 0 & \sin(5\alpha_9) & \sin(10\alpha_9) & \sin(15\alpha_9) & \cdots & \sin(35\alpha_9) & \sin(40\alpha_9) \\ \hdashline 1 & \cos(7\alpha_9) & \cos(14\alpha_9) & \cos(21\alpha_9) & \cdots & \cos(49\alpha_9) & \cos(56\alpha_9) \\ 0 & \sin(7\alpha_9) & \sin(14\alpha_9) & \sin(21\alpha_9) & \cdots & \sin(49\alpha_9) & \sin(56\alpha_9) \\ \hdashline \frac{1}{\sqrt{2}} & \frac{1}{\sqrt{2}}\cos(9\alpha_9) & \frac{1}{\sqrt{2}}\cos(18\alpha_9) & \frac{1}{\sqrt{2}}\cos(27\alpha_9) & \cdots & \frac{1}{\sqrt{2}}\cos(63\alpha_9) & \frac{1}{\sqrt{2}}\cos(72\alpha_9) \end{array}\right]$$

$$= \left[\begin{array}{ccccccccc} 0.47140 & 0.44298 & 0.36112 & 0.23570 & 0.08186 & -0.08186 & -0.23570 & -0.36112 & -0.44298 \\ 0 & 0.16123 & 0.30301 & 0.40825 & 0.46424 & 0.46424 & 0.40825 & 0.30301 & 0.16123 \\ \hdashline 0.47140 & 0.23570 & -0.23570 & -0.47140 & -0.23570 & 0.23570 & 0.47140 & 0.23570 & -0.23570 \\ 0 & 0.40825 & 0.40825 & 0 & -0.40825 & -0.40825 & 0 & 0.40825 & 0.40825 \\ \hdashline 0.47140 & -0.08186 & -0.44298 & 0.23570 & 0.36112 & -0.36112 & -0.23570 & 0.44298 & 0.08186 \\ 0 & 0.46424 & -0.16123 & -0.40825 & 0.30301 & 0.30301 & -0.40825 & -0.16123 & 0.46424 \\ \hdashline 0.47140 & -0.36112 & 0.08186 & 0.23570 & -0.44298 & 0.44298 & -0.23570 & -0.08186 & 0.36112 \\ 0 & 0.30301 & -0.46424 & 0.40825 & -0.16123 & -0.16123 & 0.40825 & -0.46424 & 0.30301 \\ \hdashline 0.33333 & -0.33333 & 0.33333 & -0.33333 & 0.33333 & -0.33333 & 0.33333 & -0.33333 & 0.33333 \end{array}\right] \tag{B.4}$$

The de-coupling matrix for the rotating orthonormal reference frame in (2.26) is the following:

$$\mathbf{P}_9(\theta) =$$

$$= \left[\begin{array}{cc:cc:cc:cc:c} \cos(\theta) & \sin(\theta) & 0 & 0 & 0 & 0 & 0 & 0 & 0 \\ -\sin(\theta) & \cos(\theta) & 0 & 0 & 0 & 0 & 0 & 0 & 0 \\ \hdashline 0 & 0 & \cos(2\theta) & \sin(2\theta) & 0 & 0 & 0 & 0 & 0 \\ 0 & 0 & -\sin(2\theta) & \cos(2\theta) & 0 & 0 & 0 & 0 & 0 \\ \hdashline 0 & 0 & 0 & 0 & \cos(3\theta) & \sin(3\theta) & 0 & 0 & 0 \\ 0 & 0 & 0 & 0 & -\sin(3\theta) & \cos(3\theta) & 0 & 0 & 0 \\ \hdashline 0 & 0 & 0 & 0 & 0 & 0 & \cos(4\theta) & \sin(4\theta) & 0 \\ 0 & 0 & 0 & 0 & 0 & 0 & -\sin(4\theta) & \cos(4\theta) & 0 \\ \hdashline 0 & 0 & 0 & 0 & 0 & 0 & 0 & 0 & 1 \end{array}\right] \tag{B.5}$$

which for $\theta = 2$ (used for demonstration) becomes:

$$\mathbf{P}_9(\theta=2) = \left[\begin{array}{cc:cc:cc:cc:c} -0.42 & 0.91 & 0 & 0 & 0 & 0 & 0 & 0 & 0 \\ -0.91 & -0.42 & 0 & 0 & 0 & 0 & 0 & 0 & 0 \\ \hdashline 0 & 0 & -0.65 & -0.76 & 0 & 0 & 0 & 0 & 0 \\ 0 & 0 & 0.76 & -0.65 & 0 & 0 & 0 & 0 & 0 \\ \hdashline 0 & 0 & 0 & 0 & 0.96 & -0.28 & 0 & 0 & 0 \\ 0 & 0 & 0 & 0 & 0.28 & 0.96 & 0 & 0 & 0 \\ \hdashline 0 & 0 & 0 & 0 & 0 & 0 & -0.15 & 0.99 & 0 \\ 0 & 0 & 0 & 0 & 0 & 0 & -0.99 & -0.15 & 0 \\ \hdashline 0 & 0 & 0 & 0 & 0 & 0 & 0 & 0 & 1 \end{array}\right] \tag{B.6}$$

Defining $\mathbf{T}_d = \mathbf{P}_9\mathbf{Q}_9$, the final real-valued orthonormal decoupling transformation matrix $\mathbf{T}_{vsd}$ is the following (the selected instant of time when $\theta = 2$ is used as example):

$$\mathbf{T}_{vsd} = \mathbf{T}_d\mathbf{W}$$

$$= \left[\begin{array}{ccccccccc} -0.19617 & 0.46931 & -0.27313 & -0.03774 & 0.42581 & -0.38807 & 0.12525 & 0.33095 & -0.45620 \\ -0.42865 & 0.04443 & 0.38421 & -0.46989 & 0.20226 & 0.26763 & -0.45446 & 0.33570 & 0.11876 \\ -0.30813 & -0.30813 & -0.30813 & -0.46303 & -0.46303 & -0.46303 & -0.15490 & -0.15490 & -0.15490 \\ 0.35676 & 0.35676 & 0.35676 & -0.08847 & -0.08847 & -0.08847 & -0.44523 & -0.44523 & -0.44523 \\ 0.45263 & -0.11224 & -0.34039 & -0.20831 & 0.47038 & -0.26207 & -0.38028 & -0.05112 & 0.43140 \\ 0.13172 & -0.45785 & 0.32613 & 0.42288 & -0.03103 & -0.39185 & -0.27858 & 0.46862 & -0.19004 \\ -0.06859 & 0.43820 & -0.36961 & 0.35233 & -0.44739 & 0.09506 & -0.47121 & 0.24725 & 0.22397 \\ -0.46639 & 0.17379 & 0.29259 & 0.31319 & 0.14853 & -0.46172 & -0.01344 & -0.40136 & 0.41480 \\ 0.33333 & 0.33333 & 0.33333 & -0.33333 & -0.33333 & -0.33333 & 0.33333 & 0.33333 & 0.33333 \end{array}\right] \tag{B.7}$$

The transformation matrix $\mathbf{T}_{vsd}$ is meant to diagonalise the phase inductance matrix $\mathbf{L}_{abc}\mathbf{T}_{park}^T\mathbf{L}_{dq}\mathbf{T}_{Park}$.

$$\mathbf{T}(\theta, h=3, \alpha=\alpha_9)$$

$$= \sqrt{\frac{2}{3}} \begin{bmatrix} \cos(\theta - 2\alpha_9) & \sin(\theta - 2\alpha_9) & 0 \\ -\sin(\theta - 2\alpha_9) & \cos(\theta - 2\alpha_9) & 0 \\ 0 & 0 & 1 \end{bmatrix} \begin{bmatrix} 1 & -\frac{1}{2} & -\frac{1}{2} \\ 0 & \frac{\sqrt{3}}{2} & -\frac{\sqrt{3}}{2} \\ \frac{1}{\sqrt{2}} & \frac{1}{\sqrt{2}} & \frac{1}{\sqrt{2}} \end{bmatrix} \tag{B.8}$$

which with $\theta = 2$ gives:

$$\mathbf{T}(\theta = 2, h = 3, \alpha = \alpha_9) \begin{bmatrix} 0.22 & 0.57 & -0.79 \\ -0.79 & 0.58 & 0.21 \\ 0.58 & 0.58 & 0.58 \end{bmatrix} \tag{B.9}$$

For simplicity, in the above equation only the third set of windings transformation is shown. Combining on the diagonal the Park's transformations for every set of windings, the final Park's transformation matrix mapping $dq0$ into abc is the following:

$$\mathbf{T}_{Park}(\theta = 2) = \left[\begin{array}{ccc:ccc:ccc} -0.34 & 0.81 & -0.47 & 0 & 0 & 0 & 0 & 0 & 0 \\ -0.74 & 0.08 & 0.67 & 0 & 0 & 0 & 0 & 0 & 0 \\ 0.58 & 0.58 & 0.58 & 0 & 0 & 0 & 0 & 0 & 0 \\ \hdashline 0 & 0 & 0 & -0.07 & 0.74 & -0.67 & 0 & 0 & 0 \\ 0 & 0 & 0 & -0.81 & 0.35 & 0.46 & 0 & 0 & 0 \\ 0 & 0 & 0 & 0.58 & 0.58 & 0.58 & 0 & 0 & 0 \\ \hdashline 0 & 0 & 0 & 0 & 0 & 0 & 0.22 & 0.57 & -0.79 \\ 0 & 0 & 0 & 0 & 0 & 0 & -0.79 & 0.58 & 0.21 \\ 0 & 0 & 0 & 0 & 0 & 0 & 0.58 & 0.58 & 0.58 \end{array}\right] \tag{B.10}$$

and the following is the phase inductance matrix:

$$\mathbf{L}_{abc} = \mathbf{T}_{park}^{T} \mathbf{L}_{dq} \mathbf{T}_{Park} =$$

$$\left[\begin{array}{ccc:ccc:ccc} 0.35013 & -0.21977 & -0.12885 & 0.31008 & -0.30096 & -0.00877 & 0.23348 & -0.34599 & 0.11216 \\ -0.21977 & 0.46360 & -0.24232 & -0.06735 & 0.43020 & -0.36251 & 0.09298 & 0.34577 & -0.43911 \\ -0.12885 & -0.24232 & 0.37268 & -0.24239 & -0.12889 & 0.37163 & -0.32682 & -0.00014 & 0.32660 \\ \hdashline 0.31008 & -0.06735 & -0.24239 & 0.32700 & -0.17233 & -0.15316 & 0.30251 & -0.25662 & -0.04554 \\ -0.30096 & 0.43020 & -0.12889 & -0.17233 & 0.43929 & -0.26545 & -0.02300 & 0.39343 & -0.37008 \\ -0.00877 & -0.36251 & 0.37163 & -0.15316 & -0.26545 & 0.42012 & -0.27916 & -0.13646 & 0.41597 \\ \hdashline 0.23348 & 0.09298 & -0.32682 & 0.30251 & -0.02300 & -0.27916 & 0.33590 & -0.13642 & -0.19797 \\ -0.34599 & 0.34577 & -0.00014 & -0.25662 & 0.39343 & -0.13646 & -0.13642 & 0.39448 & -0.25655 \\ 0.11216 & -0.43911 & 0.32660 & -0.04554 & -0.37008 & 0.41597 & -0.19797 & -0.25655 & 0.45603 \end{array}\right] \tag{B.11}$$

Finally, applying the real-valued orthonormal decoupling transformation matrix $\mathbf{T}_{vsd}$, it is possible to compute the harmonic inductances with the following equation:

$$\mathbf{L}_{vsd} = \mathbf{T}_{vsd}\mathbf{L}_{abc}\mathbf{T}_{vsd}^{T} =$$

$$\left[\begin{array}{cc:cc:cc:cc:c}
2.08749 & 0 & 0 & 0 & 0 & 0 & 0 & 0 & 0 \\
0 & 1.46325 & 0 & 0 & 0 & 0 & 0 & 0 & 0 \\
\hdashline
0 & 0 & 0.00186 & 0 & 0 & 0 & 0 & 0 & 0 \\
0 & 0 & 0 & 0.00186 & 0 & 0 & 0 & 0 & 0 \\
\hdashline
0 & 0 & 0 & 0 & 0.00094 & 0 & 0 & 0 & 0 \\
0 & 0 & 0 & 0 & 0 & 0.00094 & 0 & 0 & 0 \\
\hdashline
0 & 0 & 0 & 0 & 0 & 0 & 0.00104 & 0 & 0 \\
0 & 0 & 0 & 0 & 0 & 0 & 0 & 0.00104 & 0 \\
\hdashline
0 & 0 & 0 & 0 & 0 & 0 & 0 & 0 & 0.00081
\end{array}\right] \tag{B.12}$$

In this particular case, $d_1 = 2.08749$ and $q_1 = 1.46325$. The final harmonic inductances to be considered for current control loop design are $d_1/pu = 0.1715H$ and $q_1/pu = 0.1202H$.

Appendix C

Formulae

1. **Angle subtraction formula**
   $\cos(\alpha - \beta) = \cos\alpha\cos\beta + \sin\alpha\sin\beta$

2. **Werner formulas:**
   $\sin\alpha\cos\beta = \frac{1}{2}[\sin(\alpha+\beta) + \sin(\alpha-\beta)]$
   $\cos\alpha\cos\beta = \frac{1}{2}[\cos(\alpha+\beta) + \cos(\alpha-\beta)]$
   $\sin\alpha\sin\beta = -\frac{1}{2}[\cos(\alpha+\beta) - \cos(\alpha-\beta)]$
   $\cos\alpha\sin\beta = \frac{1}{2}[\sin(\alpha+\beta) - \sin(\alpha-\beta)]$

written in LaTeX